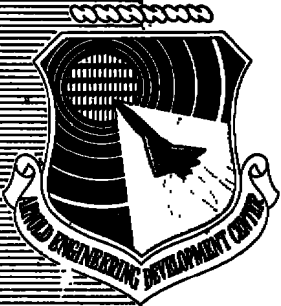


cy.2

AEDC 78-43 1985

JUL 28 1995



JET SIMULATION TECHNIQUES: SIMULATION OF TEMPERATURE EFFECTS BY ALTERING GAS COMPOSITION

W. L. Peters
ARO, Inc., a Sverdrup Corporation Company

**PROPULSION WIND TUNNEL FACILITY
ARNOLD ENGINEERING DEVELOPMENT CENTER
AIR FORCE SYSTEMS COMMAND
ARNOLD AIR FORCE STATION, TENNESSEE 37389**

March 1979

Final Report for Period October 1, 1976 to September 30, 1977

Approved for public release; distribution unlimited.

Prepared for

**ARNOLD ENGINEERING DEVELOPMENT CENTER/DOTR
ARNOLD AIR FORCE STATION, TENNESSEE 37389**

NOTICES

When U. S. Government drawings, specifications, or other data are used for any purpose other than a definitely related Government procurement operation, the Government thereby incurs no responsibility nor any obligation whatsoever, and the fact that the Government may have formulated, furnished, or in any way supplied the said drawings, specifications, or other data, is not to be regarded by implication or otherwise, or in any manner licensing the holder or any other person or corporation, or conveying any rights or permission to manufacture, use, or sell any patented invention that may in any way be related thereto.

Qualified users may obtain copies of this report from the Defense Documentation Center.

References to named commercial products in this report are not to be considered in any sense as an indorsement of the product by the United States Air Force or the Government.

This report has been reviewed by the Information Office (OI) and is releasable to the National Technical Information Service (NTIS). At NTIS, it will be available to the general public, including foreign nations.

APPROVAL STATEMENT

This report has been reviewed and approved.



ELTON R. THOMPSON

Project Manager, Research Division
Directorate of Test Engineering

Approved for publication:

FOR THE COMMANDER



ROBERT W. CROSSLEY, Lt Colonel, USAF

Acting Director of Test Engineering
Deputy for Operations

UNCLASSIFIED

REPORT DOCUMENTATION PAGE		READ INSTRUCTIONS BEFORE COMPLETING FORM
1. REPORT NUMBER AEDC-TR-78-43	2. GOVT ACCESSION NO.	3. RECIPIENT'S CATALOG NUMBER
4. TITLE (and Subtitle) JET SIMULATION TECHNIQUES: SIMULATION OF TEMPERATURE EFFECTS BY ALTERING GAS COMPOSITION	5. TYPE OF REPORT & PERIOD COVERED Final Report - Oct. 1, 1976, to Sept. 30, 1977	
	6. PERFORMING ORG. REPORT NUMBER	
7. AUTHOR(s) W. L. Peters, ARO, Inc., a Sverdrup Corporation Company	8. CONTRACT OR GRANT NUMBER(s)	
9. PERFORMING ORGANIZATION NAME AND ADDRESS Arnold Engineering Development Center/DOTR Air Force Systems Command Arnold Air Force Station, Tennessee 37389	10. PROGRAM ELEMENT, PROJECT, TASK AREA & WORK UNIT NUMBERS Program Element 65807F	
11. CONTROLLING OFFICE NAME AND ADDRESS Arnold Engineering Development Center/OIS Air Force Systems Command Arnold Air Force Station, Tennessee 37389	12. REPORT DATE March 1979	
	13. NUMBER OF PAGES 115	
14. MONITORING AGENCY NAME & ADDRESS (if different from Controlling Office)	15. SECURITY CLASS. (of this report) UNCLASSIFIED	
	15a. DECLASSIFICATION/DOWNGRADING SCHEDULE N/A	
16. DISTRIBUTION STATEMENT (of this Report) Approved for public release; distribution unlimited.		
17. DISTRIBUTION STATEMENT (of the abstract entered in Block 20, if different from Report)		
18. SUPPLEMENTARY NOTES Available in DDC		
19. KEY WORDS (Continue on reverse side if necessary and identify by block number) <div style="display: flex; justify-content: space-between;"> <div> jets plumes jet flow transonic flow wind tunnel test </div> <div> afterbodies flow nozzles drag </div> </div>		
20. ABSTRACT (Continue on reverse side if necessary and identify by block number) <p>The objective of this investigation was to evaluate the effects of individual jet exhaust properties on afterbody drag coefficient and to determine whether these properties affect drag by primarily altering the jet plume shape and/or jet entrainment. Data used in this investigation were obtained from experiments conducted in the AEDC Aerodynamic Wind Tunnel, Transonic (1T), with two different nozzle afterbody models at free-stream Mach numbers</p>		

UNCLASSIFIED

UNCLASSIFIED

20. ABSTRACT (Continued)

from 0.6 to 1.2. Integrated afterbody pressure drag coefficient data were acquired for each of these models with cold exhaust jets of six different compositions, which allowed separate variation of the jet exhaust ratio of specific heats from 1.20 to 1.40 and the gas constant from 55 to 767 ft-lbf/lbm-°R. A large reduction in afterbody drag coefficient was observed with a decrease in the specific heat ratio at most underexpanded nozzle flow conditions. Regardless of free-stream Mach number of afterbody external configuration, an increase in the gas constant produced a consistent reduction in afterbody drag coefficient that was not a function of nozzle pressure ratio. The effects of gas constant increased for separated afterbody configurations and at transonic free-stream Mach numbers. From analysis of the experimental data, it was concluded that the effects of gas constant and specific heat ratio were, to a large extent, separate, that the gas constant affected afterbody drag solely through the entrainment or mixing process, and that the specific heat ratio affected the drag primarily through determination of the inviscid jet plume shape. The effects of specific heat ratio on afterbody drag coefficient were determined to be predictable by duplicating an inviscid jet plume shape parameter, such as the nozzle exit static pressure ratio. Drag coefficient increments resulting from differences in jet entrainment with exhaust gases having different gas constants varied linearly with the square root of the gas constant and joint correlation of these data and comparable data obtained previously with hot gas exhausts showed in each case a linear variation, with parameters which are functions of the square root of the product of gas constant and exhaust temperature.

PREFACE

The work reported herein was conducted by the Arnold Engineering Development Center (AEDC), Air Force Systems Command (AFSC), for the Research Division of the Directorate of Test Engineering (AEDC/DOTR), under Program Element 65807F. The test was conducted by ARO, Inc., AEDC Division (a Sverdrup Corporation Company), operating contractor for the AEDC, AFSC, Arnold Air Force Station, Tennessee, during the period of June 20 to July 18, 1977, under Project Number P41A-N0 in support of research Project Numbers P32-H0B and P32P-40. The Air Force project manager for this work was E. R. Thompson, AEDC/DOTR. The manuscript was submitted for publication on June 19 1978.

CONTENTS

	<u>Page</u>
1.0 INTRODUCTION	7
2.0 APPARATUS	
2.1 Test Facility	8
2.2 Test Article and Support System	8
2.3 Gas Supply System	9
2.4 Instrumentation	10
3.0 PROCEDURE	
3.1 Test Conditions and Technique	11
3.2 Data Reduction	11
3.3 Uncertainty of Measurements	12
4.0 RESULTS AND DISCUSSION	
4.1 Problem Analysis and Approach	13
4.2 Presentation of Results	15
4.3 Correlation of Specific Heat Ratio Effects	19
4.4 Correlation of Gas Constant Effects	21
4.5 Correlation of Combined Total Temperature and Specific Heat Ratio Effects	23
5.0 CONCLUDING REMARKS	25
REFERENCES	26

ILLUSTRATIONS

Figure

1. Dimensional Sketch of Model	29
2. Sketches of Afterbody Configurations Tested	30
3. Model Installation Photographs	32
4. Real Gas Effects on the Specific Heat Ratio for N_2 , H_2 , and C_2H_4 Gases	35
5. Data Repeatability for the 25-deg Boattail	37
6. Gas Constant and Specific Heat Ratio for Jet Exhaust Gases	39
7. The Effects of γ_j and R_j on Afterbody Pressure Drag Coefficient for the 25-deg Boattail, $A_e/A^* = 1.271$, $T_{tj} = 630^\circ R$	40
8. The Effects of γ_j and R_j on Afterbody Pressure Drag Coefficient for the 15-deg Boattail, $A_e/A^* = 1.226$, $T_{tj} = 630^\circ R$	44

<u>Figure</u>	<u>Page</u>
9. Nozzle Total Pressure Ratio Effects on Afterbody Pressure Distributions for the 25-deg Boattail, $A_e/A^* = 1.271$, $T_{tj} = 630^\circ\text{R}$	47
10. Nozzle Total Pressure Ratio Effects on Afterbody Pressure Distributions for the 15-deg Boattail, $A_e/A^* = 1.226$, $T_{tj} = 630^\circ\text{R}$	50
11. Jet Specific Heat Ratio Effects on Afterbody Pressure Distributions at Nozzle Design Conditions for the 25-deg Boattail, $A_e/A^* = 1.271$, $T_{tj} = 630^\circ\text{R}$	53
12. Jet Specific Heat Ratio Effects on Afterbody Pressure Distributions at Nozzle Design Conditions for the 15-deg Boattail, $A_e/A^* = 1.226$, $T_{tj} = 630^\circ\text{R}$	56
13. Jet Gas Constant Effects on Afterbody Pressure Distributions at Nozzle Design Conditions for the 25-deg Boattail, $A_e/A^* = 1.271$, $T_{tj} = 630^\circ\text{R}$	59
14. Jet Gas Constant Effects on Afterbody Pressure Distributions at Nozzle Design Conditions for the 15-deg Boattail, $A_e/A^* = 1.226$, $T_{tj} = 630^\circ\text{R}$	62
15. Comparison of Inviscid Jet Plume Shape Parameters in Correlating Jet Specific Heat Ratio Effects on Afterbody Pressure Drag Coefficient for the 25-deg Boattail, $A_e/A^* = 1.271$, $T_{tj} = 630^\circ\text{R}$	64
16. Comparison of Inviscid Jet Plume Shape Parameters in Correlating Jet Specific Heat Ratio Effects on Afterbody Pressure Drag Coefficient for the 15-deg Boattail, $A_e/A^* = 1.226$, $T_{tj} = 630^\circ\text{R}$	68
17. Inviscid Jet Plume Shape Parameters as a Function of NPR, $A_e/A^* = 1.250$	72
18. Pressure Drag Coefficient Differences between Jet Exhausts of Varying Gas Constant at Design, Overexpanded, and Underexpanded Jet Plume Shape Conditions, $T_{tj} = 630^\circ\text{R}$	73
19. Correlation Parameters for Jet Gas Constant Effects at Design, Overexpanded, and Underexpanded Jet Plume Shape Conditions for the 25-deg Boattail, $A_e/A^* = 1.271$, $T_{tj} = 630^\circ\text{R}$	75
20. Correlation Parameters for Jet Gas Constant Effects at Design, Overexpanded, and Underexpanded Jet Plume Conditions for the 15-deg Boattail, $A_e/A^* = 1.226$, $T_{tj} = 630^\circ\text{R}$	83

<u>Figure</u>	<u>Page</u>
21. Correlation Parameters for Jet Gas Constant Effects and Mach Number Effects at Nozzle Design Conditions, $T_{tj} = 630^{\circ}\text{R}$	91
22. Jet Total Temperature and Specific Heat Ratio Effects on Afterbody Pressure Drag Coefficient as a Function of an Inviscid Jet Plume Shape Matching Parameter, $A_e/A^* = 1.000$, $R_j = 53.35 \text{ ft-lbf/lbm-}^{\circ}\text{R}$ (Data from Refs. 1 and 3)	99
23. Comparison of Pressure Drag Coefficient Increments on the 25-deg Boattail at Fixed Jet Plume Shape Conditions for the Effects of Jet Temperature, Gas Constant, and Ratio of Specific Heats	103
24. Comparison of Pressure Drag Coefficient Increments on the 15-deg Boattail at Fixed Jet Plume Shape Conditions for the Effects of Jet Temperature, Gas Constant, and Ratio of Specific Heats	106

TABLES

1. External Pressure Orifice Locations	109
2. Test Summary	110
3. Free-Stream Test Conditions	111
4. Basic Properties of Jet Exhaust Gases Tested	111

NOMENCLATURE	112
------------------------	-----

1.0 INTRODUCTION

A previous evaluation of jet simulation parameters for nozzle afterbody testing was conducted and reported in Ref. 1. The investigation attempted to improve the wind tunnel test technique of using an unheated air jet exhaust to duplicate the jet effects produced by an aircraft engine exhaust. Various parameters were examined during the investigation in an effort to correlate nozzle afterbody drag coefficient, a measure of jet interference, for jet exhausts of differing temperature. The results demonstrated that adequate correlation could be achieved at certain specific test conditions and for certain afterbody configurations by matching an inviscid jet plume shape parameter. However, analysis indicated that to attain a general jet simulation, another jet mechanism, jet entrainment or mixing, need also be duplicated. For this prior investigation, the jet effects on an afterbody attributable to plume shape and those associated with entrainment were impossible to separate. No means was ascertained to differentiate how variations in jet exhaust total temperature or specific heat ratio, a secondary temperature effect, acted to influence these two jet mechanisms, and thus, change drag.

The present investigation was conducted to evaluate the afterbody drag effects produced by varying individual jet exhaust gas properties and to show whether these properties affect drag by primarily altering the jet plume shape and/or jet entrainment. Two jet exhaust gas properties, the gas constant (R_j) and the specific heat ratio (γ_j), were considered and were independently varied by changing jet exhaust gas composition. Variations in the gas constant (R_j) were chosen to simulate variations in the jet total temperature (T_{t_j}) because many jet flow parameters that should have some relationship to jet simulation are functions of the $R_j T_{t_j}$ product. Examples of such parameters are the jet mass flow, momentum, kinetic energy, and velocity. Adoption of such equivalence of temperature and gas constant also allows the specific heat ratio to be decoupled from "temperature" effects by individually varying R_j and γ_j with selected gas mixtures. Thus, the effects of T_{t_j} , represented by R_j , could be assessed separately from those produced by γ_j . The specific heat ratio (γ_j), which represents a secondary temperature effect, was examined because many jet simulation parameters which have been considered in prior investigations of jet exhaust temperature effects are largely a function of γ_j but are independent of R_j and T_{t_j} . Examples of such parameters which represent jet plume shape matching parameters include the nozzle exit-to-free-stream static pressure ratio, incremental Prandtl-Meyer angle, and the maximum jet plume-to-nozzle exit diameter ratio.

Experiments were conducted in Tunnel 1T, using two strut-mounted pod models representing both separated (25-deg boattail) and unseparated (15-deg boattail) external afterbody contours. Integrated afterbody pressure drag coefficient data were acquired for

each of these models for six jet exhaust gas compositions. Gases composed of either nitrogen (N_2), hydrogen (H_2), ethylene (C_2H_4), or one of three differing mixtures of N_2 and H_2 were exhausted at the rear of each of the models through a convergent-divergent nozzle ($A_e/A^* \approx 1.25$). These gases allowed a variation in R_j from approximately 55 to 767 ft-lbf/lbm-°R and in γ_j from about 1.20 to 1.40. Exhaust gas total temperature was maintained at approximately 630°R. Testing was conducted at nominal free-stream Mach numbers ranging from 0.6 to 1.2, at model nozzle total pressure ratios from approximately 1 to 16, and a model angle of attack of 0 deg.

2.0 APPARATUS

2.1 TEST FACILITY

Tunnel 1T is a continuous-flow, nonreturn wind tunnel capable of being operated at Mach numbers from 0.2 to 1.5, utilizing variable nozzle contours above $M_\infty = 1.10$. The tunnel is operated at a stilling chamber total pressure of about 2,850 psfa with a ± 5 percent variation, dependent on tunnel resistance and ambient atmospheric conditions. The total temperature can be varied from 80 to 120°F above ambient temperatures as necessary to prevent visible condensation in the test section. The test section is 1-ft square and 37.5 in. long with 6 percent porous perforated walls. A detailed description of the tunnel and its operating capabilities is given in Ref. 2.

2.2 TEST ARTICLE AND SUPPORT SYSTEM

The experimental data for this investigation were acquired from tests conducted with two axisymmetric nozzle afterbody models of similar overall design but with differing external afterbody contours. Each model had a length of 14.697 in., a maximum body diameter of 0.986 in., and each incorporated a 14-deg half-angle nose. Both models included an internal plenum chamber connected to a convergent-divergent nozzle that exited at the rear of the model. A support strut was used to mount either model in the wind tunnel test section, producing a maximum cross-sectional area of the model/strut arrangement equivalent to 1.96 percent of the test section cross-sectional area. The strut thickness-to-chord ratio was a fixed value of 0.0853 from the tunnel floor to the model. Six, 1/4-in.-diam passageways were contained within the strut for supplying a high-pressure gas to the model plenum chamber from an external tunnel source. In addition, one other larger passageway was provided to route model thermocouple leads and pressure tubes to instrumentation panels outside the test section. A sketch showing model and strut details in the tunnel is presented in Fig. 1.

The external afterbody contours for the models tested were 25- and 15-deg boattail geometries and represented 1/10-scale replicas of those used in hot and cold jet exhaust tests conducted in Tunnel 16T and reported in Refs. 1 and 3. The internal nozzle details differed slightly between the 25- and 15-deg boattail models, although the nozzle divergence half-angle was 5-deg for both. The contraction and nozzle exit-to-throat area ratios were, respectively, 4.645 and 1.271 for the 25-deg boattail model and were, respectively, 4.676 and 1.226 for the 15-deg boattail model. A sketch showing the external and internal design of each of the afterbodies is presented in Fig. 2. For a portion of testing, the 15-deg boattail model was installed with a solid cylindrical plume simulator which fastened within the model at the front of the plenum chamber. The external portion of the simulator had a diameter equivalent to the nozzle exit diameter and extended approximately 3 in. downstream of the exit. Model photographs are presented in Fig. 3 showing the 25-deg boattail model and the 15-deg boattail model with and without the plume simulator installed.

2.3 GAS SUPPLY SYSTEM

Six jet exhaust compositions were used for the tests conducted with these models. Three exhaust gases were composed of either pure nitrogen (N_2), hydrogen (H_2), or ethylene (C_2H_4) gases and the remaining three were composed of differing mixtures by weight of N_2 and H_2 . A gas piping system, located externally to the wind tunnel, controlled, temperature-conditioned, and supplied these gases to the model. Two different piping schemes were utilized, depending on whether the jet exhaust was composed of a pure gas or a mixture of two gases.

If a pure gas was used as the jet exhaust, the piping system ducted the flow through a double-tube steam heat exchanger and then to any one of three available control valves, a manual-type needle valve and two pneumatic-controlled valves. Located downstream of each pneumatic valve was a choked venturi metering section for measurement of the mass flow of the high-pressure gas. The venturi throat diameter differed for each valve. Thus, by having two pneumatic valves from which to choose, flexibility was gained in measurement of the mass flow for varying required model plenum chamber pressure and for varying available gas supply pressure. The manual needle-type valve was used to a limited extent to regulate small gas flows that the pneumatic valves could not control. After the gas was routed through either one of the pneumatic valves and the associated venturi-metering section or through the needle valve, it was supplied to a manifold which was connected to the base of the model support strut.

For a jet exhaust composed of a mixture of two gases, i.e., N_2 and H_2 , each gas was initially controlled by a pneumatic valve and routed through a venturi metering section

for mass flow measurement. Downstream of the two venturis, the gases merged and the resulting mixture was temperature-conditioned in the double-tube heat exchanger. The mixture was then supplied to the model in the same manner as the pure gas. For the three N_2/H_2 mixture flows that were tested, three pairs of different sized venturis were required. Each pair of venturis represented a fixed nitrogen-hydrogen mass flow ratio, assuming the given pair were operated with a similar venturi upstream supply pressure and temperature.

2.4 INSTRUMENTATION

The two models tested were each instrumented with 26 static pressure orifices distributed axially and circumferentially about the afterbody external surface. In addition, each model had three nozzle base pressure orifices at different circumferential locations. The position of these orifices on both models is presented in Table 1. These pressures were measured by the Tunnel 1T pressure system comprised of a five-module, 48-port Scanivalve. Each valve had a 15-psid differential transducer with tunnel total and plenum pressures as the respective calibrate and reference pressures. The calibrate and reference pressures were measured by a more accurate instrumentation system to allow computation of an on-line Scanivalve® calibration constant for each valve at every data point. Both models incorporated four static pressures within the plenum chamber and two static pressures within the diverging section of the convergent-divergent nozzle. These pressures were measured by strain-gage type transducers with a range from 0 to 500 psia and 0 to 200 psia, respectively. Two copper-constantan thermocouples were located in the plenum chamber of each model to measure gas supply temperature for computation of nozzle mass flow.

Upstream venturi supply and throat static pressures were measured by strain-gage transducers with a range from 0 to 2,000 psia. A copper-constantan thermocouple located upstream of each venturi metering section was used to measure gas supply temperature for mass flow calculations.

Instrumentation readouts in engineering units of all thermocouples, venturi supply pressures, and model plenum chamber static pressures were provided in the tunnel control room for monitoring purposes and for setting desired model nozzle flow conditions. All electrical signals from instrumentation data channels were processed through an analog-to-digital converter, recorded on paper tape, and fed to a facility computer for on-line data reduction.

3.0 PROCEDURE

3.1 TEST CONDITIONS AND TECHNIQUE

Test data were acquired at free-stream Mach numbers of 0.6, 0.8, 0.9, and 1.2 as shown by the test summary in Table 2. Free-stream Reynolds numbers corresponding to these Mach numbers at a tunnel stagnation temperature of 610°R are indicated in Table 3. A test section wall angle of 0 deg was maintained at all test conditions and testing of both models was conducted only at an angle of attack of 0 deg. Nozzle total pressure ratio was the primary run variable, ranging from approximately 1 to 16 depending on gas supply pressure and free-stream Mach number.

The data acquisition procedure, without the plume simulator, consisted of setting the appropriate free-stream conditions, regulating the nozzle plenum chamber static pressure and/or venturi supply pressure(s) to give the required nozzle total pressure ratio, and adjusting the steam heater flow to produce a desired gas supply temperature in the plenum chamber. A plenum chamber temperature of approximately 630°R ($\pm 30^\circ$) was maintained to correspond closely to the free-stream total temperature. For testing with the plume simulator, the gas supply system was disconnected, and the only run variable was free-stream Mach number.

3.2 DATA REDUCTION

The primary parameter presented in this report as a measure of jet interference was the integrated afterbody pressure drag coefficient. For both models, this parameter was based on a maximum model cross-sectional area of approximately 0.76 in.² and was determined by numerically integrating the pressure distribution on the afterbody surface excluding the nozzle base area. This coefficient represented the pressure drag on the nozzle/afterbody projected area aft of M.S. = 14.068 in. for the 25-deg boattail model and aft of M.S. = 13.662 in. for the 15-deg boattail model.

Venturi mass flow calculations were based on the following equation:

$$\dot{m}_v = \frac{(C) (K_1) (K_2) (P_v) (D_v)^2 (\lambda_v)}{\sqrt{T_v}} \quad (1)$$

where C is a constant, K_1 equals the discharge coefficient at the venturi throat assuming laminar flow, K_2 is a factor which is a function of the gas constant and the ratio of specific heats, P_v and T_v are the respective static pressure and temperature measured upstream of the venturi, D_v is the measured venturi throat diameter, and λ_v is the contraction area ratio correction for static pressure to obtain total pressure upstream of

the venturi. The ratio of specific heats used for venturi computations was determined from the upstream venturi static pressure and temperature assuming real gas properties. Real gas data for nitrogen (N_2), hydrogen (H_2), and ethylene (C_2H_4) were obtained, respectively, from the following sources: Refs. 4, 5, and 6. In Fig. 4, the real gas effects on γ are presented as a function of pressure at various temperatures for these gases.

Isentropic relations were used for computation of all nozzle flow and jet parameters presented herein. An average plenum chamber static pressure and the nozzle contraction area ratio were used to calculate the nozzle total pressure. The ratio of specific heats (γ) was assumed to be a constant value of 1.40 (calorically perfect) for jet exhausts composed of N_2 , H_2 , or any mixture of these two gases. For $0 < P_{t_c} < 300$ psia at $T_{t_c} = 630^\circ R$, this produced a maximum deviation from the real gas γ of less than 2 percent for N_2 and less than 0.2 percent for H_2 . For a jet exhaust composed of ethylene (C_2H_4), a real gas specific heat ratio was determined based on an average plenum chamber static pressure and temperature and using the real gas data of Fig. 4.

The gas constant (R_j) for a nozzle flow composed of N_2 and H_2 gases was computed from the following equation:

$$R_{\text{mixture}} = \frac{(\dot{m}_{vN_2}) (R_{N_2}) + (\dot{m}_{vH_2}) (R_{H_2})}{\dot{m}_{vN_2} + \dot{m}_{vH_2}} \quad (2)$$

a consequence of the laws of mixtures of gases. By using these results, venturi metering sections were fabricated prior to testing to give desired values of R_{mixture} .

3.3 UNCERTAINTY OF MEASUREMENTS

Estimates of the uncertainties for certain test parameters at a 95-percent confidence level are as follows:

U	<u>$M_\infty = 0.6$</u>	<u>$M_\infty = 0.9$</u>	<u>$M_\infty = 1.2$</u>
M_∞	± 0.0044	± 0.0037	± 0.0039
q_∞ , psi	± 0.0518	± 0.0357	± 0.0234
NPR	± 0.0317	± 0.0431	± 0.0606
C_{p_x}	± 0.0184	± 0.0108	± 0.0101

Since increments rather than absolute levels in afterbody drag coefficient (C_{D_p}) are of primary interest for this evaluation of individual jet property effects, the repeatability

instead of the computed uncertainty gives a better measure of data reliability. In Fig. 5, typical drag coefficient repeatability is presented for the 25-deg boattail.

4.0 RESULTS AND DISCUSSION

4.1 PROBLEM ANALYSIS AND APPROACH

The important results from a prior investigation (Ref. 1) of jet simulation parameters for nozzle afterbody testing are listed below:

1. Significant afterbody drag differences are present between jet exhausts of varying temperature at a fixed nozzle total pressure ratio (NPR).
2. Duplication of parameters that characterize the inviscid jet plume boundary demonstrate better correlation of afterbody drag than the parameter NPR for underexpanded jets of dissimilar temperature. These inviscid plume shape parameters provide better jet simulation for unseparated afterbody flows as compared with separated flows.
3. At nozzle design conditions (complete expansion), no parameter produces any better jet simulation than the parameter NPR.

As these results indicate, matching of an inviscid jet plume shape parameter does not give universal correlation of afterbody drag for variations in jet exhaust temperature, in particular, at nozzle design conditions and for separated afterbody configurations. This implies that some other jet mechanism, perhaps jet pumping on the afterbody flow or jet entrainment as proposed by Compton (Ref. 7) is responsible for a portion of the drag differences observed. But distinguishing the separate effects of jet shape and jet entrainment on afterbody drag proves to be difficult for the data of this previous study. Two interrelated jet exhaust properties, total temperature (T_{tj}) and the ratio of specific heats (γ_j), were varied simultaneously, and determining how these properties individually influence jet shape and jet entrainment cannot be ascertained.

The present study attempted to overcome this problem by altering jet exhaust gas composition to allow the specific heat ratio and gas constant to be varied independently. The gas constant (R_j) was considered for this investigation to provide a variation similar to that of exhaust total temperature (T_{tj}). One reason for this equivalence is that many inviscid parameters which should have some relationship to jet simulation are functions of the $R_j T_{tj}$ product. The following list of parameters which will be considered herein illustrates this point:

<u>Parameter</u>	<u>Equation</u>	<u>Definition</u>	
V_j	$M_j \gamma_j^{1/2} g^{1/2} R_j^{1/2} T_{tj}^{1/2} \left(1 + \frac{\gamma_j - 1}{2} M_j^2\right)^{1/2}$	Velocity, ft/sec	(3)
$\rho_j V_j$	$P_{tj} M_j \gamma_j^{1/2} g^{1/2} R_j^{-1/2} T_{tj}^{-1/2} \left(1 + \frac{\gamma_j - 1}{2} M_j^2\right)^{-(\gamma_j + 1)/2(\gamma_j - 1)}$	Mass flux, lbm/ft ² -sec	(4)
$\rho_j V_j^2$	$P_{tj} M_j^2 \gamma_j g \left(1 + \frac{\gamma_j - 1}{2} M_j^2\right)^{-\gamma_j/(\gamma_j - 1)}$	Momentum flux, lbm/ft-sec ²	(5)
$\rho_j V_j^3$	$P_{tj} M_j^3 \gamma_j^{3/2} g^{3/2} R_j^{1/2} T_{tj}^{1/2} \left(1 + \frac{\gamma_j - 1}{2} M_j^2\right)^{(-3\gamma_j + 1)/2(\gamma_j - 1)}$	Kinetic energy flux, lbm/sec ³	(6)

Another advantage of the method chosen to simulate high temperature jets by use of low molecular weight mixtures of approximate room temperature gases is that specific heat ratios are constant, thus independent of the R_j which can be used to simulate the effect at high temperature. By evaluation of the preceding parameters, say at the nozzle exit plane or at the inviscid jet plume boundary, it becomes evident that this characteristic is very important. If the Mach number, jet total pressure and temperature, and specific heat ratio of the jet are fixed and the gas constant of the jet allowed to vary, these parameters are reduced to the following:

<u>Parameter</u>	<u>Equation</u>	
$V_j = V_e \text{ or } V_1$	$\text{constant} \times (R_j)^{1/2}$	(7)
$\rho_j V_j = \rho_e V_e \text{ or } \rho_1 V_1$	$\text{constant} \times (R_j)^{-1/2}$	(8)
$\rho_j V_j^2 = \rho_e V_e^2 \text{ or } \rho_1 V_1^2$	constant	(9)
$\rho_j V_j^3 = \rho_e V_e^3 \text{ or } \rho_1 V_1^3$	$\text{constant} \times (R_j)^{1/2}$	(10)

As shown, V_j and $\rho_j V_j^3$ both vary directly with $\sqrt{R_j}$, while $\rho_j V_j$ varies inversely with it. The momentum flux ($\rho_j V_j^2$), being independent of both R_j and T_{tj} , is fixed as R_j changes. With M_j , P_{tj} , T_{tj} , and γ_j constant, the inviscid jet plume boundary is invariant in size and shape at a given NPR. This implies that, ideally, any differences in afterbody drag observed with changing R_j at a fixed NPR are attributable to jet entrainment or mixing effects.

Jet simulation parameters examined herein for changes in γ_j were inviscid jet plume boundary parameters similar to those considered in prior investigations of jet exhaust temperature effects on afterbody drag. These type parameters, although not a function of

R_j , are largely affected by variations in γ_j , since they represent the jet expansion process external to the nozzle and the subsequent jet plume boundary shape that results. A list of these inviscid jet plume shape parameters is as follows:

<u>Parameter</u>	<u>Equation</u>	<u>Definition</u>
$\Delta\nu$	$= \nu_1 - \nu_e$	Incremental Prandtl-Meyer angle, (11) deg $\nu = f(\gamma, M)$ (See Ref. 8)
NSPR	$= \frac{P_e}{P_\infty} = \frac{P_{t_1}}{P_\infty} \left(1 + \frac{\gamma_j - 1}{2} M_e^2 \right)^{-\gamma_j/(\gamma_j - 1)}$	Nozzle exit static to free-stream (12) static pressure ratio
D_1/D_e	$= \sqrt{A_1/A_e} = \sqrt{(A_1/A^*)/(A_e/A^*)}$ $A_1/A^* = f(\gamma_j, M_1)$ (see Ref. 8)	Maximum inviscid jet plume (13) boundary-to-nozzle exit diameter ratio

Initially, ten differing gases encompassing a wide range of values for both γ and R were chosen from a list comprised of approximately 89 gases. In Fig. 6, these ten gases are presented graphically to show their respective γ and R values. As indicated, these gases fall into distinct lines of constant γ and constant R . Because of safety, economic, and problem analysis considerations, only three of these ten gases were chosen to be tested as jet exhausts. Nitrogen (N_2) was chosen as a baseline since it closely resembles air in many of its properties including similar γ and R values. Ethylene (C_2H_4) was considered because its ratio of specific heats at room temperature represents the near minimum of that experienced by a heated jet exhaust in a real turbojet or turbofan engine nozzle. Furthermore, ethylene has a gas constant approximately equal to that of nitrogen, thus comparison of afterbody drag coefficient between nitrogen and ethylene jet exhausts show only the effect of γ_j . Hydrogen (H_2) was chosen because of its high R value (equivalent to matching some high T_1) and because at low temperature its γ is equal to that of nitrogen. Three mixtures of hydrogen and nitrogen were also tested as jet exhaust gases to obtain afterbody drag data at intermediate values of R_j between that provided by N_2 and H_2 . The basic properties for the jet exhaust gases tested are presented in Table 4.

4.2 PRESENTATION OF RESULTS

4.2.1 Effects of Individual Variation of Gas Constant and Specific Heat Ratio on Afterbody Drag Coefficient

In Figs. 7 and 8, afterbody pressure drag coefficient data are presented for jet exhaust gases of separately varying specific heat ratio (γ_j) and gas constant (R_j). These

results are shown for two external afterbody geometries, a 25-deg and a 15-deg boattail, at free-stream Mach numbers from 0.6 to 1.2 and are presented as a function of nozzle total pressure ratio (NPR). This parameter is commonly duplicated in present nozzle afterbody testing in the wind tunnel. In addition to the data presented for differing jet exhaust gases, drag coefficient data are presented for the 15-deg boattail with a solid cylindrical plume simulator. This cylindrical plume represents the inviscid jet plume shape at nozzle design conditions, and these data are shown at an NPR value that corresponds to design for $\gamma_j = 1.40$.

These results show that the overall drag trend with NPR, ignoring absolute drag levels, is similar regardless of the jet exhaust properties, the free-stream Mach number, or the external afterbody geometry. From jet-off to initial jet-on, drag coefficient sharply decreases to some minimum value which corresponds to an NPR of approximately one. This "drag bucket" point is probably attributable to the jet exhaust filling the wake behind the model and thus pressurizing the afterbody base and boattail surfaces and corresponds closely to the NPR for initial nozzle choked flow. An increase in NPR from this drag bucket point produces a drag rise that continues until a maximum jet-on drag point is obtained. Since a drag rise indicates a lowering of afterbody surface static pressures, and thus an increase in flow velocity over the afterbody surface, this implies that jet pumping or jet entrainment may be involved. In general, for a given jet exhaust gas, the drag increments defined between jet-off and the drag bucket point and between the drag bucket and the maximum jet-on drag point are observed to be equal or larger for the 25-deg boattail as compared with the 15-deg boattail and larger for transonic free-stream Mach numbers 0.9 and 1.2 than for the subsonic Mach numbers 0.6 and 0.8. It should be noted that the maximum jet-on drag point occurs at differing NPR values depending on jet exhaust properties, free-stream Mach number, and afterbody geometry. The magnitude of the drag rise from the drag bucket generally increases with increasing value of NPR at the drag peak, except for the 25-deg boattail at $M_\infty = 0.9$ and 1.2. In these cases there is a change in the drag rise and no associated change in NPR at the drag peak. The maximum drag point perhaps represents the point where jet plume effects on afterbody drag become more important than jet entrainment effects, because the drag reduction beyond the peak is characteristic of an increase in size of the inviscid jet plume.

The effect of the jet exhaust specific heat ratio (γ_j) on afterbody drag is generally similar for the 25- and 15-deg boattail models as shown in Figs. 7 and 8. At NPR's below the point of maximum drag, the effect of γ_j is small and irregular. At NPR's greater than that for maximum drag, the effect of a reduction in γ_j is to reduce the drag by an amount which increases with NPR and which is also much greater for the afterbody having attached flow (15-deg boattail). This dependence can be linked to the fact that for

a given nozzle total pressure ratio, the inviscid jet plume becomes larger with decreasing γ_j . It is suggested that the effect is less for the afterbody with the 25-deg boattail because, in this case, the plume grows into a separated wake region and is not in direct contact with the external flow. Inviscid jet plume shape parameters that characterize this growth in plume size include those that will be considered herein for jet simulation capabilities in correlating γ_j effects on afterbody drag.

As observed in Figs. 7 and 8, the effect of jet exhaust gas constant (R_j) on afterbody drag coefficient is significantly larger and quite different than that of γ_j . Except for several anomalies at $M_\infty = 1.2$ for the 15-deg boattail, an increase in R_j produces a reduction in afterbody drag coefficient that generally appears as a constant shift in C_{D_p} for a matched NPR at $\text{NPR} \geq 1$. This behavior is very similar to that observed for an increase in T_{tj} in Ref. 1. In general, the effects of R_j are noted to be equal or slightly greater for the 25-deg boattail as compared with the 15-deg boattail and are larger for transonic Mach numbers ($M_\infty = 0.9$ and 1.2) as compared with subsonic Mach numbers ($M_\infty = 0.6$ and 0.8). From earlier discussion, the jet effects produced by varying R_j can be attributed to jet mixing or jet entrainment since the other jet mechanism, plume shape, can be fixed by matching NPR (since $\gamma_j = \text{constant}$).

The effect of solid cylindrical plume simulator on afterbody drag coefficient is shown in Fig. 8 for the 15-deg boattail. These results, as stated earlier, are presented at the design nozzle total pressure ratio since the cylindrical shape closely corresponds to the inviscid jet plume shape at nozzle design conditions and $\gamma = 1.4$. By comparing the drag coefficient data for this simulator with the jet exhaust data, it is observed that the solid plume at $M_\infty = 0.6$ gives approximately the same drag as that obtained with a jet exhaust with an R_j value of 767 ft-lbf/lbm-°R. Similar comparisons of the drag data for the plume simulator at Mach numbers 0.9 and 1.2 show that solid plume produces a drag coefficient that lies in the midst of those for jet exhausts of differing R_j . At this time, no satisfactory explanation of the drag results for the solid plume in relation to that of the jet exhaust data can be given.

4.2.2 Effect of Nozzle Total Pressure Ratio and Free-Stream Mach Number on Afterbody Pressure Distributions

In Figs. 9 and 10, afterbody surface pressure distributions are presented for the 25- and 15-deg boattail models to show the effect of varying NPR at various free-stream Mach numbers. These results are shown for a jet exhaust composed of nitrogen ($\gamma_j = 1.40$, $R_j = 55.159$) at nozzle total pressure ratios corresponding to jet-off, the drag bucket point ($\text{NPR} \approx 1$), the nozzle design condition, and at a highly underexpanded jet

condition. For each afterbody geometry these pressure distributions represent the effects on the boattail surface beginning at the shoulder and ending at, but prior to, the nozzle base.

The pressure distributions indicate appreciable differences in streamline patterns, shock locations, and separation points between the two afterbodies and between different M_∞ from subsonic to low supersonic conditions. For the 25-deg boattail, at $M_\infty = 0.6$ (Fig. 9a), flow recompression occurs over almost the entire length of the boattail and concludes at a pressure slightly greater than ambient. However, at Mach numbers 0.9 and 1.2 (Figs. 9b and c) only a slight recompression occurs after the shoulder followed by an almost flat pressure distribution ending with a pressure level less than that of the free-stream static pressure. It is suggested that at these conditions separated flow over the aft portion of the afterbody surface exists, while at Mach number 0.6, the afterbody flow remains attached.

A flow expansion immediately downstream of the afterbody shoulder is observed for the 15-deg boattail at all Mach numbers. This expansion continues until some minimum pressure is realized, after which a recompression of the flow occurs. The recompression ends at the aft portion of the boattail and reaches a pressure level greater than free-stream static pressure for Mach numbers 0.6 and 0.9 and is at a pressure level slightly less than free-stream static pressure for Mach number 1.2. The flow expansion region appears to cover a greater portion of the afterbody surface as Mach number increases. As a result, a more adverse pressure gradient is noted in the recompression region for the 15-deg boattail at $M_\infty = 1.2$. Separated flow is suspected at the end of the model because of the adverse pressure gradient which ends at a pressure level less than ambient.

For both afterbody geometries regardless of free-stream Mach number, the effects of nozzle total pressure ratio are felt over the entire recompression region of the pressure distribution. As shown here and as indicated earlier, a larger afterbody drag, at least for jet-on conditions, corresponds to a general decrease in these pressures while a smaller drag coincides with an increase in these pressures. Nozzle total pressure ratio effects on the pressure distributions appear largest in regions where separated afterbody flow has been suspected. The variations of pressure distribution with nozzle total pressure ratio at a given M_∞ are, however, generally much smaller than the variation with M_∞ , suggesting that only minor variations in flow pattern occur as NPR varies from 1.0 to 16.0 at a given M_∞ .

4.2.3 Effects of Specific Heat Ratio and Gas Constant on Afterbody Pressure Distributions

The effects of the jet exhaust specific heat ratio (γ_j) on afterbody pressure distributions are shown for the 25- and 15-deg boattail models in Figs. 11 and 12. These pressure data are presented at the respective nozzle total pressure ratios required to match nozzle design conditions (NSPR = 1) for a nitrogen jet exhaust ($\gamma_j = 1.40$) and for an ethylene jet exhaust ($\gamma_j = 1.20$ to 1.27). As shown, the pressure distributions are practically identical for the two specific heat ratios for a given free-stream condition and afterbody geometry. Since the range of γ_j presented encompasses that experienced in hot and cold jet exhaust testing, the effects of specific heat ratio on afterbody pressure distribution at nozzle design pressure ratio can be considered negligible.

In Figs. 13 and 14, the effects of the jet exhaust gas constant (R_j) on afterbody pressure distributions are presented for the 25- and 15-deg boattail models at their respective nozzle design pressure ratios. For the 15-deg boattail, pressure distributions are presented only at free-stream Mach numbers 0.6 and 1.2, and at these conditions only a limited amount of data are shown. Other results for this afterbody were not considered because of anomalies in the pressure distributions.

The effect of an increasing value of the gas constant (14-fold) is observed to be a general increase in surface pressure for both afterbody shapes and at all Mach numbers, except for the region of expanding flow on the 15-deg boattail, where there is little or no effect. The pressure rise is relatively uniform along the afterbody and is larger in regions of suspected separated flow than in regions of attached flow. These increases of pressure correspond directly to the drag decrease observed at nozzle design conditions in Figs. 7 and 8.

4.3 CORRELATION OF SPECIFIC HEAT RATIO EFFECTS

The effects of jet exhaust specific heat ratio (γ_j) on afterbody pressure drag coefficient are presented in Figs. 15 and 16 for the 25- and 15-deg boattail models as a function of NPR and several inviscid jet plume shape parameters. These data are shown for nozzle total pressure ratios equal to or greater than that required for a normal shock at the nozzle exit. The inviscid jet plume shape parameters presented are the nozzle exit-to-free-stream static pressure ratio (NSPR), the incremental Prandtl-Meyer angle ($\Delta\nu$), and the maximum plume-to-nozzle exit diameter (D_1/D_e). The parameters NSPR and $\Delta\nu$ represent two parameters identified for jet simulation performance for hot and cold jet exhausts reported in Ref. 1. The parameter D_1/D_e has been found to provide correlation of afterbody drag for conventional and annular jet configurations in a study conducted and reported in Ref. 9. These three inviscid plume shape parameters were computed using

isentropic nozzle relations, although it is realized these relations are invalid for overexpanded nozzle flows at which a portion of these drag data are presented. Although it does not by itself determine plume shape, the parameter NPR is shown for these results for comparative purposes since it is, as expressed earlier, a parameter commonly duplicated in present nozzle afterbody testing.

As shown, from overexpanded jet conditions to a nozzle pressure ratio of about 7, the parameter NPR gives drag correlation of specific heat ratio effects within 40 drag counts (based on maximum cross-sectional area) for both boattails at all free-stream Mach numbers presented. For $7 < \text{NPR} < 13$, the correlation becomes increasingly poor with increasing NPR and M_∞ . Discrepancies of 50 to 120 drag counts for the 15-deg boattail model and up to 100 drag counts for the 25-deg boattail model are observed at $M_\infty = 1.2$.

Excellent correlation of afterbody drag (within 30 drag counts) for the effects of γ_j is achieved at free-stream Mach numbers 0.6 and 0.9 at all jet conditions by duplicating either of the parameters $\Delta\nu$ or D_1/D_2 . At $M_\infty = 1.2$, however, these parameters have a tendency to overcorrect the effects of γ_j at underexpanded jet conditions on both boattails, and discrepancies in the drag correlation at highly underexpanded jet conditions are as large as 85 counts for D_1/D_e and up to 140 counts for $\Delta\nu$ on the 15-deg boattail body.

Correlation by use of the parameter NSPR gives almost exact duplication of afterbody drag for the effects of γ_j on the 25-deg boattail at all jet and free-stream conditions shown. For the 15-deg boattail, matching NSPR does not provide as good a drag correlation as that achieved by matching $\Delta\nu$ or D_1/D_e at subsonic free-stream Mach numbers; however, by including the results at $M_\infty = 1.2$, this correlation collapses the drag data for all conditions and both boattails to within 50 drag counts. From this discussion, the effects of γ_j on afterbody drag that exist between real aircraft engine jet exhausts and a simulated jet exhaust composed of unheated air used in the wind tunnel can thus be eliminated if an inviscid jet plume shape parameter, such as NSPR, is matched.

In Fig. 17, the parameters (NSPR, $\Delta\nu$, and D_1/D_e) calculated from Eqs. (11) to (13) are presented as a function of NPR for jet exhaust specific heat ratios of 1.21 and 1.40. A γ_j of 1.21 represents the thermally perfect value for an ethylene jet exhaust gas at $T_{t_j} = 630^\circ\text{R}$. As these parameter plots show, at a given NPR, the value of these inviscid jet plume shape parameters increases as γ_j is decreased. This coincides with earlier comments that the inviscid jet plume becomes larger at a fixed NPR as γ_j is reduced.

4.4 CORRELATION OF GAS CONSTANT EFFECTS

Afterbody pressure drag coefficient increments for the 25- and 15-deg boattail models are presented in Fig. 18 as a function of NPR to demonstrate the drag differences that result for changes in the jet exhaust gas constant (R_j) at constant γ_j . These drag coefficient increments were obtained by means of interpolation at constant values of NPR for pressure ratios equal to or greater than that required for a normal shock at the exit. At a given NPR, the drag increments were determined by subtracting the drag coefficient produced by a nitrogen jet exhaust ($R_j = 55 \text{ ft-lbf/lbm-}^\circ\text{R}$) from the drag coefficient produced by a jet exhaust with R_j of any other value. The drag coefficient for the nitrogen jet exhaust was chosen to be subtracted since, for comparative purposes, it most closely resembles the drag coefficient produced by a simulated jet exhaust composed of unheated air commonly used for nozzle afterbody testing in the wind tunnel. For the 15-deg boattail, data are included at Mach numbers 0.6, 0.9, and 1.2 that have anomalies as a possible result of physical changes in the wind tunnel during testing with this model but which, nevertheless, appear to demonstrate an overall drag trend with R_j similar to that of the 25-deg boattail.

Since a matched value of NPR coincides with a fixed inviscid jet plume shape (as well as constant jet momentum) for these particular data (because $\gamma_j = \text{constant}$), drag coefficient increments represent differences in jet entrainment that are produced by varying R_j . As observed, these differences become larger as R_j is increased and, in general at a given free-stream Mach number, do not vary significantly with NPR for either afterbody. However, as noted earlier, the drag increments for the 25-deg boattail are equal to or larger than for the 15-deg boattail and are larger for transonic Mach numbers 0.9 and 1.2 than for the subsonic Mach number of 0.6.

In Figs. 19 and 20, entrainment-related drag increments produced by varying R_j are presented for both afterbody geometries as a function of several parameters which correspond to the jet exhaust velocity, mass flux, and kinetic energy flux. Each of these parameters is a function of R_j and T_{tj} . Thus, if the jet effects produced by changes in R_j can be correlated by any of these parameters, then the jet effects produced by variations in T_{tj} can possibly be correlated by the same parameters. Parameters shown include $\sqrt{R_j}$, which is proportional to the jet exhaust velocity and kinetic energy flux, and $1/\sqrt{R_j}$ which is, likewise, proportional to the jet exhaust mass flux. Others presented represent differences in actual magnitudes of the jet exhaust and free-stream quantities of velocity, mass flux, and kinetic energy flux computed at both the nozzle exit plane and the inviscid jet plume boundary. These parameters were determined assuming isentropic relationships were valid, even at overexpanded jet conditions. Parameters correspondent to the jet momentum flux were not considered for these results since momentum remains constant for variations in R_j at a given P_{tj} .

The correlations of drag increments produced by jet entrainment differences resulting from R_j variation are shown as curves of constant NPR (representing fixed inviscid jet plume shape and jet momentum). Three curves of constant NPR are presented for each afterbody geometry at free-stream Mach numbers 0.6, 0.9, and 1.2. The three differing NPR's correspond to overexpanded and underexpanded jet conditions as well as nozzle design conditions.

The results indicate that at a fixed NPR, the drag increments produced by changes in R_j vary in a nearly linear manner with $\sqrt{R_j}$ and thus nonlinearly with $1/\sqrt{R_j}$. It is further observed at a given free-stream Mach number that the different NPR curves, representing overexpanded and underexpanded nozzle total pressure ratios, collapse essentially on a single line when presented as a function of these parameters. This occurs because jet entrainment differences appear for the most part to be nearly independent of nozzle total pressure ratio (see Fig. 18). The maximum spread in ΔC_{D_p} between lines of constant NPR at any free-stream Mach number with either afterbody geometry is no greater than 80 drag counts for an NPR range from 2 to 6.

As a function of the velocity parameters ($V_e - V_\infty$ and $V_1 - V_\infty$) and the kinetic energy flux parameters ($\rho_e V_e^3 - \rho_\infty V_\infty^3$ and $\rho_1 V_1^3 - \rho_\infty V_\infty^3$) entrainment-related drag increments at a given NPR vary in a straight-line manner, as might be anticipated from the results with $\sqrt{R_j}$. Likewise, the entrainment differences as a function of the mass flux parameters ($\rho_e V_e - \rho_\infty V_\infty$ and $\rho_1 V_1 - \rho_\infty V_\infty$) exhibit a similar trend as when presented versus $1/\sqrt{R_j}$. Of these six parameters, only $(V_e - V_\infty)$ appears to correlate the jet entrainment differences for various pressure ratios at a fixed Mach number and does so similarly as $\sqrt{R_j}$. The other parameters prove to be unsatisfactory correlation parameters for jet entrainment differences as a result of being functions of NPR. Normalization of these parameters with NPR should, however, produce correlation equal to that of $\sqrt{R_j}$ or $1/\sqrt{R_j}$.

In conclusion, jet entrainment and mixing effects on afterbody drag appear to be relatively insensitive to NPR over a wide range of overexpanded and underexpanded jet conditions and thus are relatively independent of inviscid jet plume shape. Since jet momentum varies with NPR, these jet entrainment differences seem to be also relatively independent of jet momentum. This assumes that jet plume shape and jet momentum do not act in a compensating manner such as to produce jet entrainment differences essentially constant over the NPR range. (It may also be that matching jet plume shape and matching jet momentum are synonymous for these results.) Finally, parameters proportional to $\sqrt{R_j}$ but independent of NPR seem to linearly correlate the jet entrainment differences observed for various NPR's.

Comparison of drag increments at design nozzle pressure ratio which were produced by varying R_j at various Mach numbers is presented for the 25- and 15-deg boattail models in Fig. 21. At design conditions, the inviscid jet plume boundary is, by definition, cylindrical in shape with a diameter equivalent to the nozzle exit diameter. In an attempt to correlate these drag coefficient increments, they are shown as functions of quantities representing both differences between and ratios of the jet exhaust and free-stream velocities, mass fluxes, and kinetic energy fluxes. Since nozzle exit and inviscid jet plume boundary conditions are identical at nozzle design pressure ratio, there is no distinction between these parameters in the plume and at the nozzle exit. Momentum-related parameters were not considered, because, as before, jet momentum remains fixed when R_j varies at a given P_{tj} .

As observed, the jet entrainment differences in afterbody drag coefficient produced by altering R_j at nozzle design conditions vary linearly with the $\sqrt{R_j}$. The data in Fig. 21 demonstrate that this line of variable R_j but fixed NPR becomes steeper in slope as free-stream Mach number increases and/or the boattail angle increases. Thus, there are significant differences in the drag coefficient increments observed between two Mach numbers at a matched value of $\sqrt{R_j}$. Maximum differences in these coefficient increments between Mach numbers 0.6 and 1.2 are approximately 260 drag counts and 100 drag counts for the 25- and 15-deg boattails, respectively. The correlation of jet entrainment differences for various Mach numbers in terms of $1/\sqrt{R_j}$ is no better, as might be anticipated. Matching parameters representing both differences and ratios of the jet exhaust and free-stream velocities and kinetic energy fluxes serve to further degrade this correlation, although the linearity of the jet entrainment differences at a given Mach number is comparable to $\sqrt{R_j}$. By matching the mass flux related parameters (shown in Figs. 21e and f), the jet entrainment differences (produced by varying R_j) for various Mach numbers are best correlated. As shown, these entrainment differences collapse together within 100 drag counts for the 25-deg and 85 counts for the 15-deg boattail at free-stream Mach numbers from 0.6 through 1.2.

4.5 CORRELATION OF COMBINED TOTAL TEMPERATURE AND SPECIFIC HEAT RATIO EFFECTS

In Fig. 22, afterbody pressure drag coefficient data from Refs. 1 and 3 are presented to show the effects produced by varying the jet exhaust total temperature (T_{tj}) and the jet exhaust specific heat ratio (γ_j) simultaneously. These results, obtained in Tunnel 16T, are shown for both the 25- and 15-deg boattails on an isolated nozzle afterbody model very similar to the 1T model for this present investigation, but approximately ten times larger in scale. The drag coefficient data are presented as a function of NSPR, which represents one of the parameters previously shown to correlate the jet effects produced

by changes in γ_j . If matching NSPR is assumed to duplicate inviscid jet plume shape for exhausts of differing γ_j , then the variation of C_{D_p} on Fig. 22 must be the result of differences in mixing or jet entrainment produced by variation of T_{tj} . An increase in T_{tj} produces almost constant downward shift in drag over the entire NSPR range and does so for both external afterbody geometries at all free-stream Mach numbers shown. As a result of the similar drag variation noted for changes in T_{tj} and R_j at matched plume shape conditions, it is concluded that the basic physical mechanisms characterizing mixing at the plume boundary are determined primarily by the $R_j T_{tj}$ product, although there may also be secondary influences which are important in any given case.

Drag coefficient increments produced by variations of R_j and T_{tj} at matched plume shape conditions (fixed NSPR) are presumed to be associated with jet entrainment and are compared in Figs. 23 and 24 for the 25- and 15-deg boattail bodies, respectively. (The variable R_j data are given for the nozzle design pressure ratio, but limitations on test data required that the variable T_{tj} data be given for NSPR = 2.0. Figure 22 shows that there is only a small change in ΔC_{D_p} between NSPR = 1.0 and 2.0.) The entrainment differences for the effects of temperature (T_{tj}) were obtained at a fixed NSPR by subtracting the afterbody drag coefficient for a jet exhaust composed of unheated air from that for a jet exhaust of higher temperature, composed of exhaust products of ethylene/air combustion. The products of ethylene/air combustion closely resemble those of an actual aircraft engine exhaust since the hydrogen-carbon ratio is similar for ethylene and JP fuels. The jet entrainment differences representing the effects of exhaust gas constant (R_j) were determined by the method discussed earlier, using the drag coefficient for the nitrogen jet as the baseline to be subtracted. Since air and nitrogen have similar properties at ambient conditions, the entrainment differences presented for variations in temperature and gas constant were obtained using a similar baseline jet exhaust gas. Although the trends in C_{D_p} are quite similar for the T_{tj} and R_j variation in Figs. 23 and 24, it should be recognized that the comparison may be affected by such secondary influences as differences in model and support system between 1T and 16T, dissimilar model blockage, 1T strut interference, and small differences in the supersonic Mach numbers in the data comparison.

In Figs. 23 and 24, these drag coefficient differences are presented as a function of jet-to-free-stream ratios of velocity, mass flux, and kinetic energy flux. The ratio representing momentum flux is not presented because, at a matched jet plume shape condition (fixed value of NSPR), and a given free-stream condition, the effects of varying jet temperature and specific heat ratio change the momentum ratio by a negligible amount. (It has been previously indicated that varying R_j has no effect on jet momentum.) In general, varying γ_j over the range of specific heat ratios experienced by an aircraft engine does not significantly alter the magnitude of entrainment-related

parameters such as the jet-to-free-stream ratios of velocity, mass flow flux, and kinetic energy flux. This substantiates an earlier conclusion that the effects of γ_j on afterbody drag are primarily related to inviscid jet plume shape. Jet entrainment differences for variations in jet temperature and gas constant prove to be similar and exhibit a like trend as a function of the various parameters presented. As a result, it appears possible that for nozzle afterbody wind tunnel tests that the entrainment effects produced by jet temperature might possibly be simulated by judicious selection of the jet exhaust gas constant. Since the nozzle exit-to-free-stream velocity parameter has proved to correlate jet entrainment differences for the effects of R_j at various inviscid jet plume shape conditions, it appears that the parameter $\sqrt{R_j T_{t_j}}$ may relate temperature and gas constant effects on jet entrainment over a wide range of nozzle total pressure ratios. Further research is recommended with a given afterbody configuration to verify this.

5.0 CONCLUDING REMARKS

The objective of this investigation was to evaluate the effects of individual jet exhaust properties on integrated afterbody pressure drag coefficient. Data for this investigation were obtained from experiments conducted with two isolated nozzle afterbody configurations where essentially unheated gases with six different jet compositions were utilized to separately vary the exhaust ratio of specific heats from 1.20 to 1.40 and to vary the exhaust gas constant from 55 to 767 ft-lbf/lbm-°R.

Experimental observations and results are as follows:

1. The variation of afterbody drag coefficient with nozzle pressure ratio was found to be similar to that observed with heated combustion gases for which total temperature and specific heat ratio vary simultaneously. A drag rise that commences at a nozzle total pressure ratio (NPR) corresponding to initial choked nozzle flow increases in magnitude and continues to a progressively higher NPR as the internal flow passes through the subsonic to the supersonic regime. Beyond the drag peak representing the conclusion of the drag rise, a reduction in drag occurs which is characteristic of an increase in the inviscid jet plume size.
2. Variation of the specific heat ratio at a fixed NPR and a given value of the gas constant was found to have little or no effect on the afterbody drag coefficient at nozzle pressure ratios below the drag peak. Above the drag peak, decreasing the specific heat ratio produced a drag reduction which increased monotonically with further increases in the pressure ratio. Afterbody drag coefficient for the normally unseparated 15-deg boattail model was more sensitive to the effects of specific heat ratio than the separated 25-deg boattail model.

3. An increase in the gas constant at a fixed NPR and a given value of the specific heat ratio was found to produce a constant decrease in drag coefficient over the entire range of nozzle pressure ratio covered. The effects of gas constant on afterbody drag coefficient were greater for a separated afterbody as compared with an unseparated afterbody and were greater for transonic Mach numbers as compared with subsonic Mach numbers.

From these observations the following conclusions were made:

1. In terms of the physical mechanisms involved, it is clear that the gas constant and temperature affect the drag coefficient only through the mixing or entrainment process between the jet and the free-stream flow. The specific heat ratio has little or no effect on the mixing/entrainment process at nozzle pressure ratios up to the drag peak and it is inferred that this is true for all pressure ratios. As a consequence, it is concluded that variations in specific heat ratio affect the drag primarily, if not exclusively, through resultant changes in the inviscid plume shape.
2. Drag coefficients obtained for different values of specific heat ratio at a given value of the gas constant were found to correlate very well with the nozzle static pressure ratio, corresponding to matched inviscid plume shape and are, therefore, predictable by duplicating this parameter.
3. Drag coefficient increments produced by variation of the gas constant at a fixed NPR and at a given value of specific heat ratio displayed a linear variation with square root of the gas constant. At matched plume shape conditions, joint correlations of these data and comparable data obtained previously with hot combustion gas exhaust jets showed in each case a linear variation with parameters directly dependent on the square root of the product of jet gas constant and exhaust temperature. An ideal correlation parameter for these effects was not identified; however, several parameters were found which could provide the basis for judicious adjustment of cold jet parameters to give proper simulation of hot jet tests.

REFERENCES

1. Peters, W. L. "An Evaluation of Jet Simulation Parameters for Nozzle Afterbody Testing at Transonic Mach Numbers." AEDC-TR-76-109 (ADA031525), October 1976.

2. Test Facilities Handbook (Tenth Edition). "Propulsion Wind Tunnel Facility, Vol. 4." Arnold Engineering Development Center, May 1974.
3. Galigher, Lawrence L., Yaros, S. F., and Bauer, R. C. "Evaluation of Boattail Geometry and Exhaust Plume Temperature Effects on Nozzle Afterbody Drag at Transonic Mach Numbers." AEDC-TR-76-102 (ADA030852), October 1976.
4. Hilsenrath, Joseph, et al. "Tables of Thermal Properties of Gases." National Bureau of Standards, Circular 564, November 1, 1955.
5. Johnson, Robert C. "Real Gas Effects in Critical-Flow-Through Nozzles and Tabulated Thermodynamic Properties." NASA TN D-2565. January 1965.
6. Ellenwood, Frank O., Kulik, Nicholas, and Gay, Norman R. "The Specific Heats of Certain Gases over Wide Ranges of Pressures and Temperatures." Cornell University Engineering Experiment Station. Bulletin No. 30, October 1942.
7. Compton, W. B. "Effects of Jet Exhaust Gas Properties on Exhaust Simulation and Afterbody Drag." NASA TR R-444, October 1975.
8. Ames Research Staff. "Equations, Tables, and Charts for Compressible Flow." Report 1135, 1953.
9. Price, Earl A. "A Parametric Investigation of the Annular Jet Concept for Obtaining Afterbody Drag at Transonic Mach Numbers." AEDC-TR-77-104 (ADA050891), February 1978.

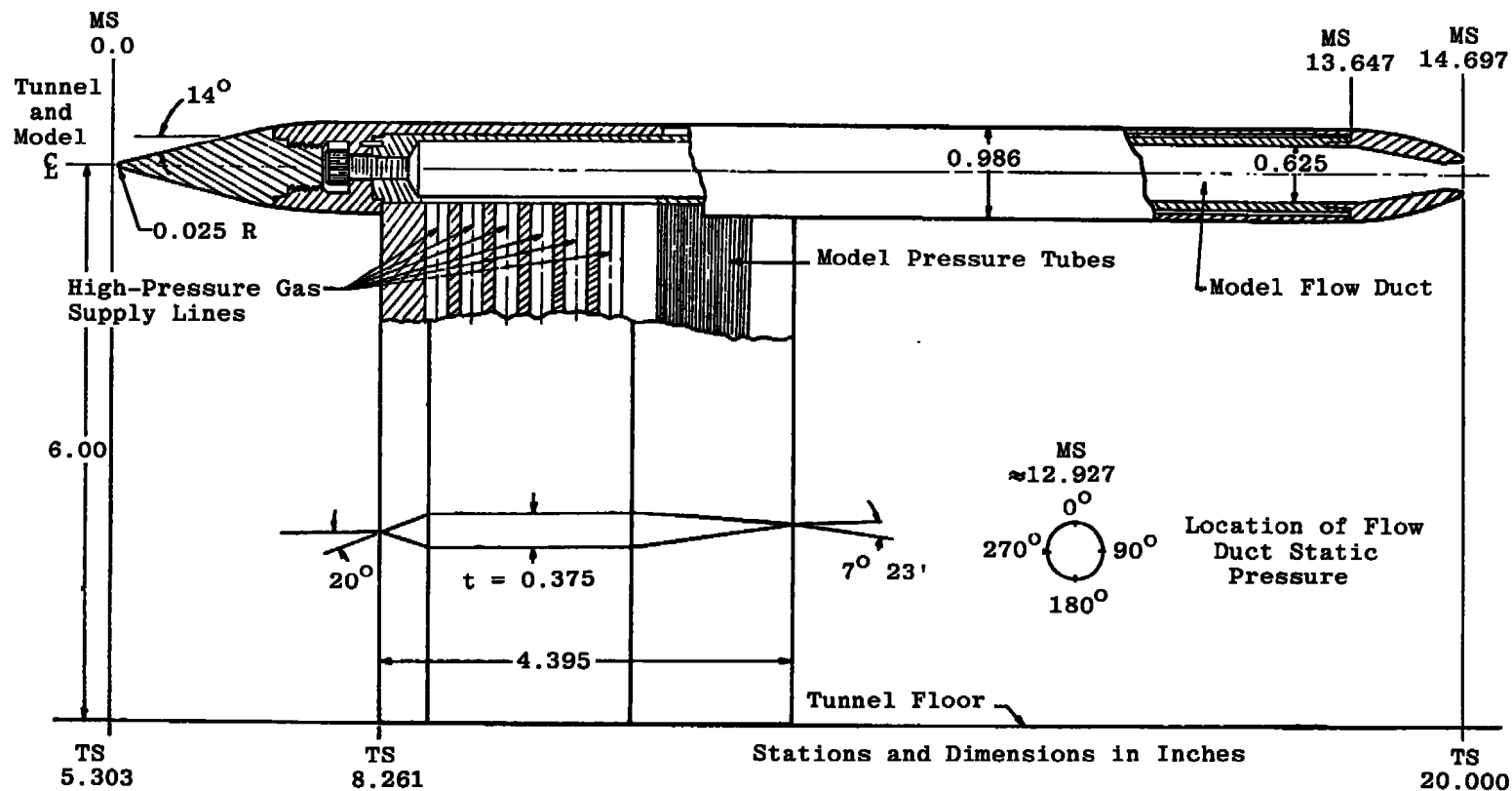
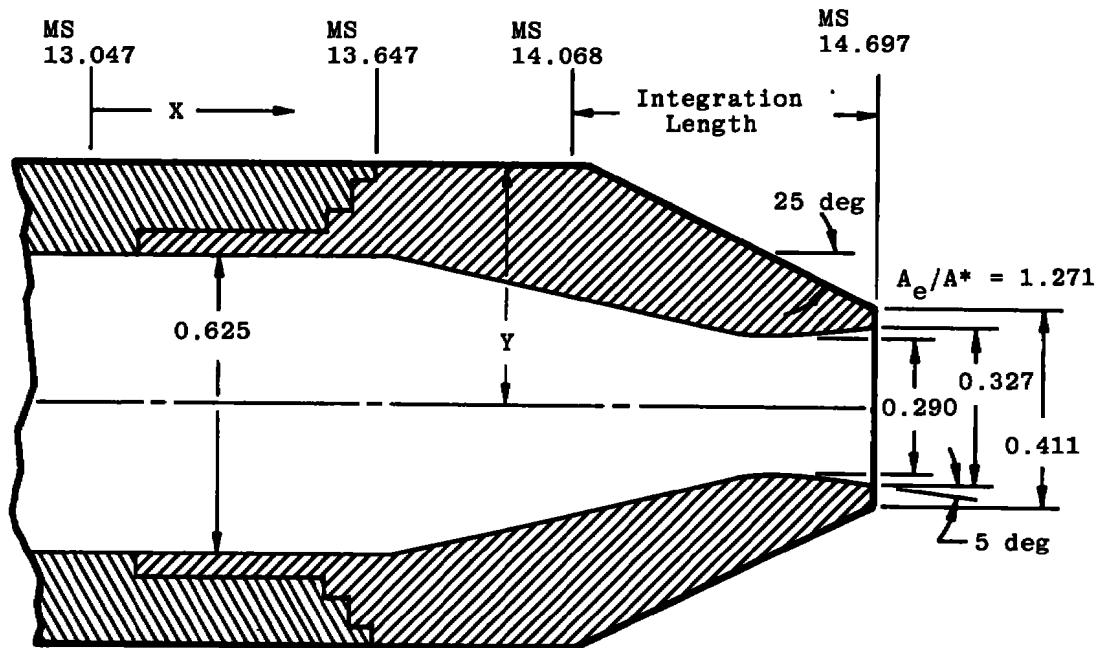


Figure 1. Dimensional sketch of model.

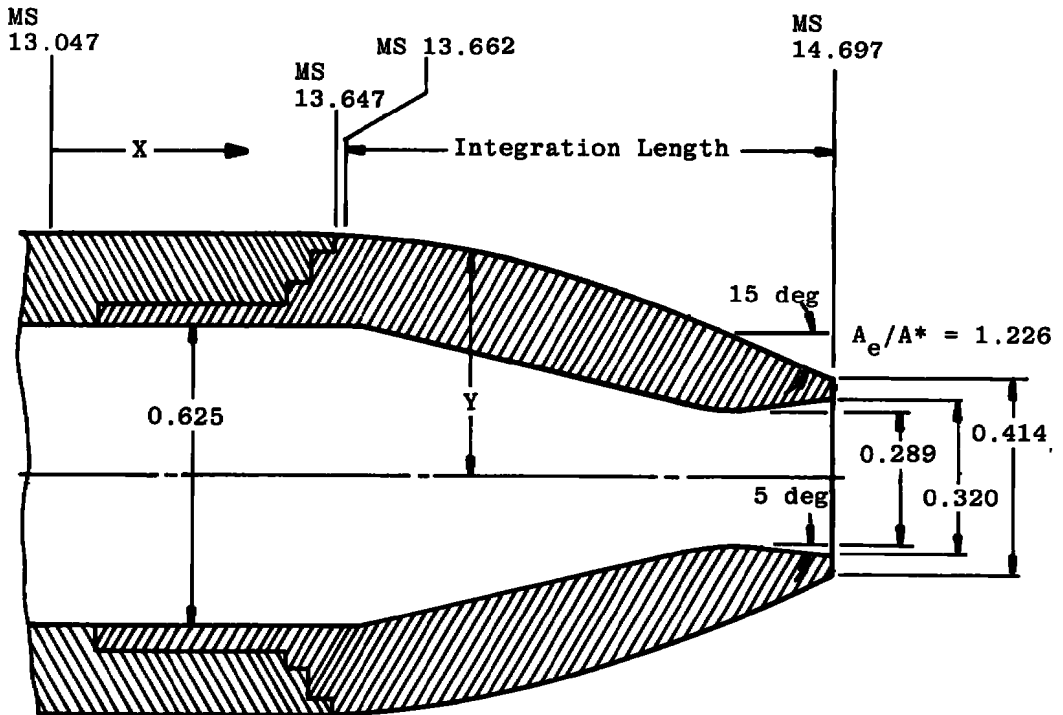


Stations and Dimensions in Inches

X	Y	X	Y
1.021	0.492	1.305	0.368
1.034	0.491	1.354	0.344
1.058	0.487	1.403	0.322
1.083	0.479	1.453	0.299
1.108	0.468	1.502	0.276
1.157	0.444	1.552	0.252
1.206	0.419	1.601	0.230
1.256	0.393	1.650	0.205

a. 25-deg boattail

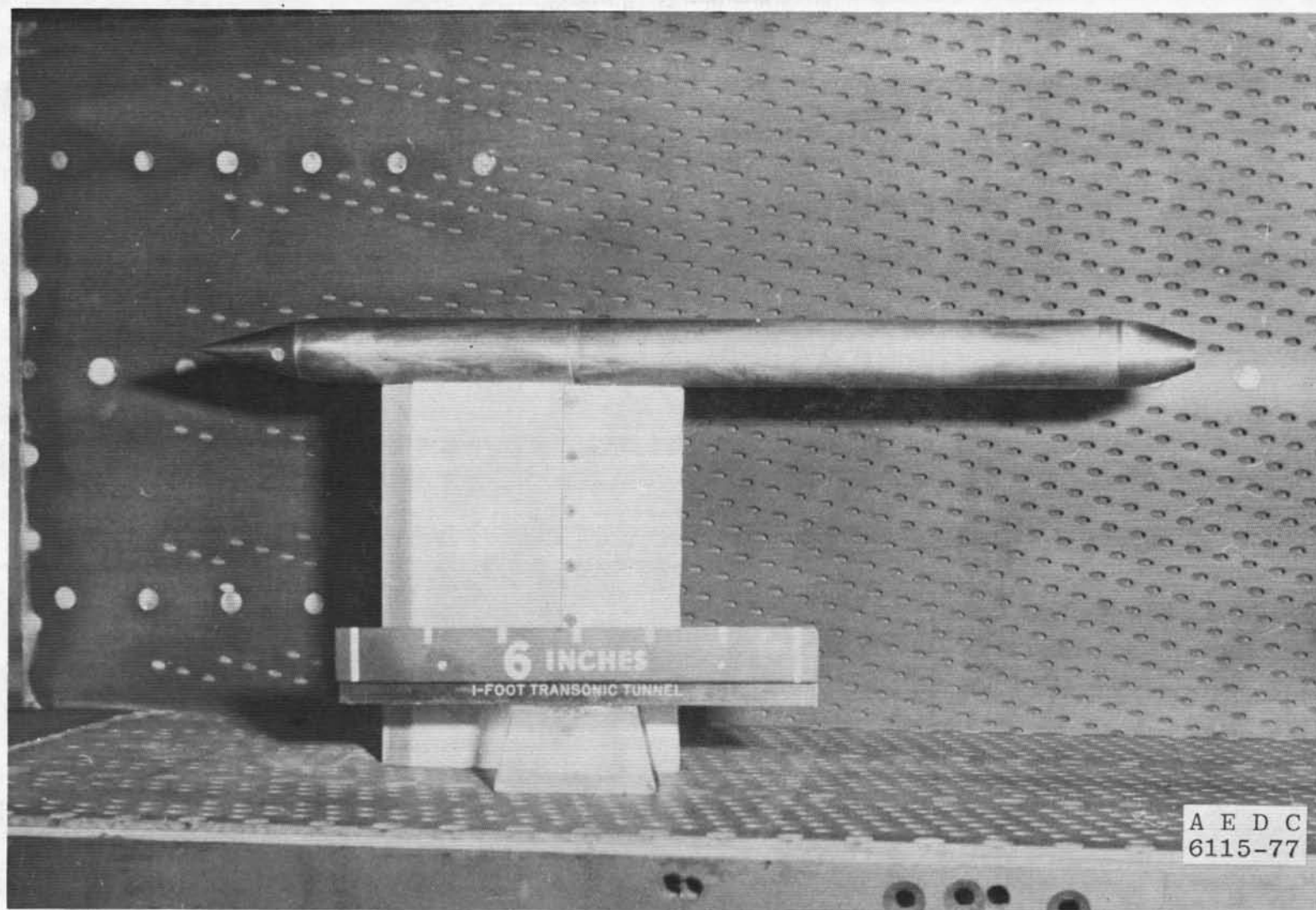
Figure 2. Sketches of afterbody configurations tested.



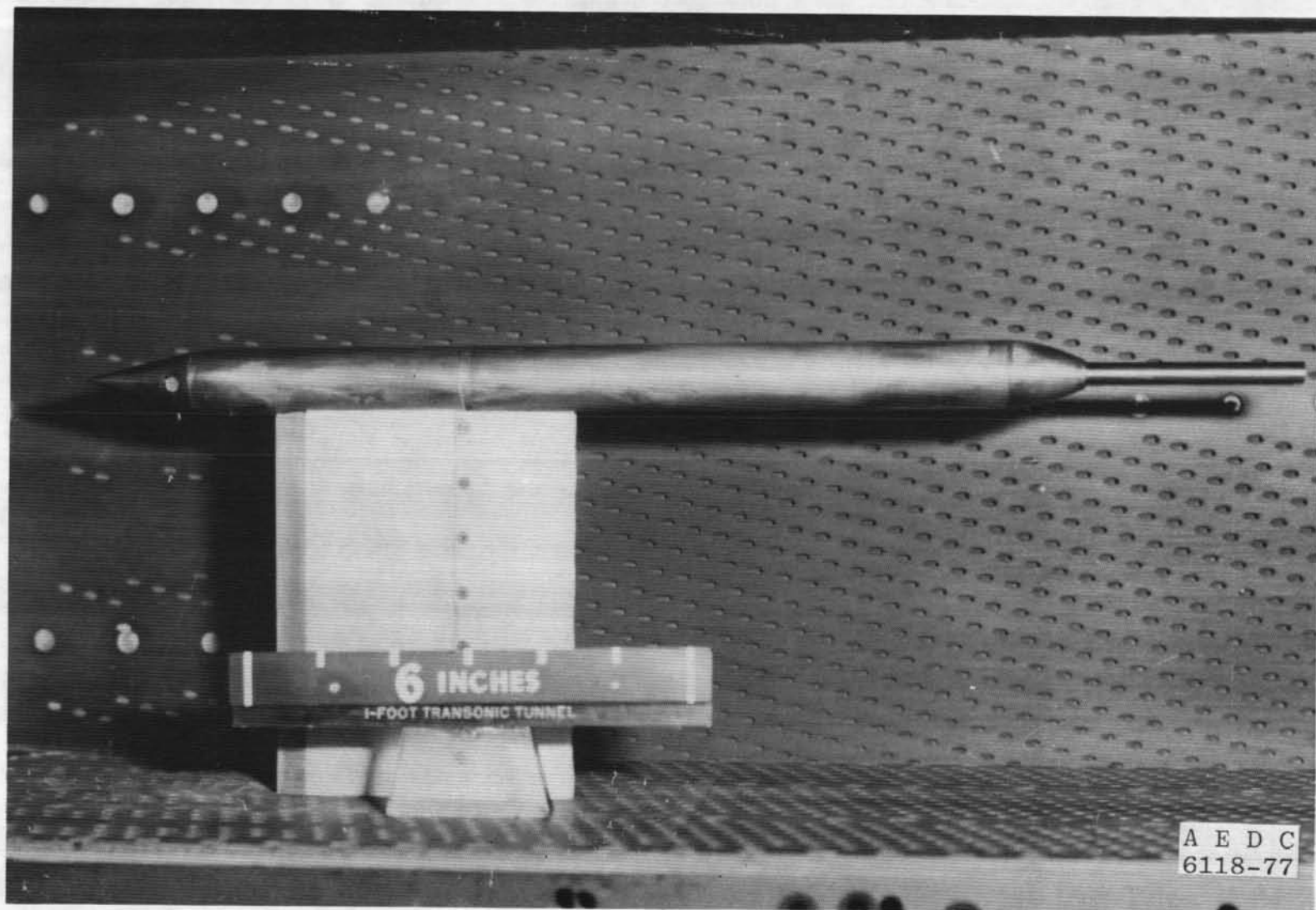
Stations and Dimensions in Inches

X	Y	X	Y
0.615	0.492	1.157	0.393
0.664	0.490	1.206	0.378
0.713	0.486	1.256	0.361
0.763	0.480	1.305	0.344
0.812	0.473	1.354	0.327
0.861	0.464	1.403	0.308
0.910	0.454	1.453	0.288
0.960	0.444	1.502	0.268
1.008	0.433	1.552	0.247
1.058	0.420	1.601	0.226
1.108	0.407	1.650	0.207

b. 15-deg boattail
Figure 2. Concluded.



b. 15-deg boattail
Figure 3. Continued.



c. 15-deg boattail with plume simulator
Figure 3. Concluded.

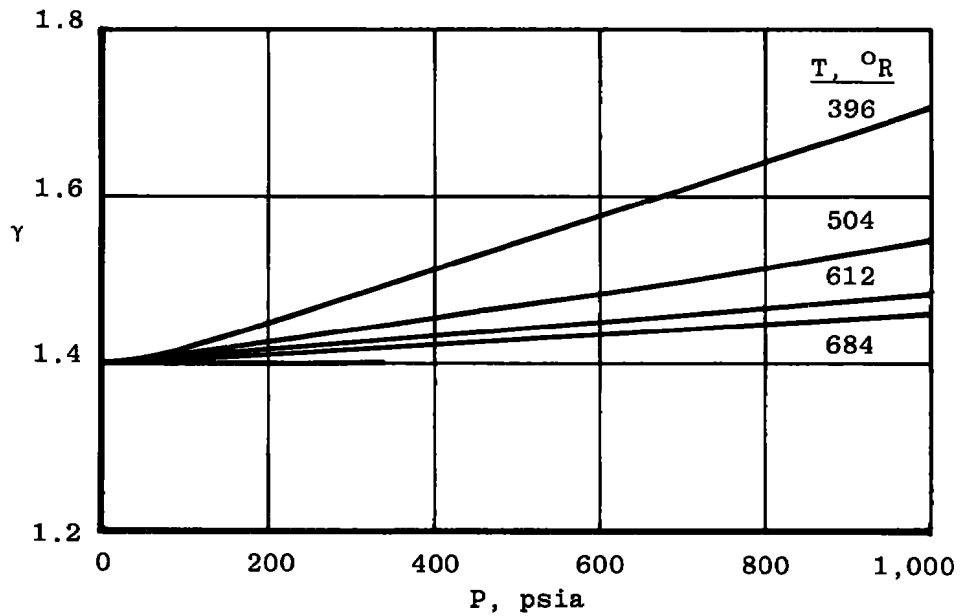
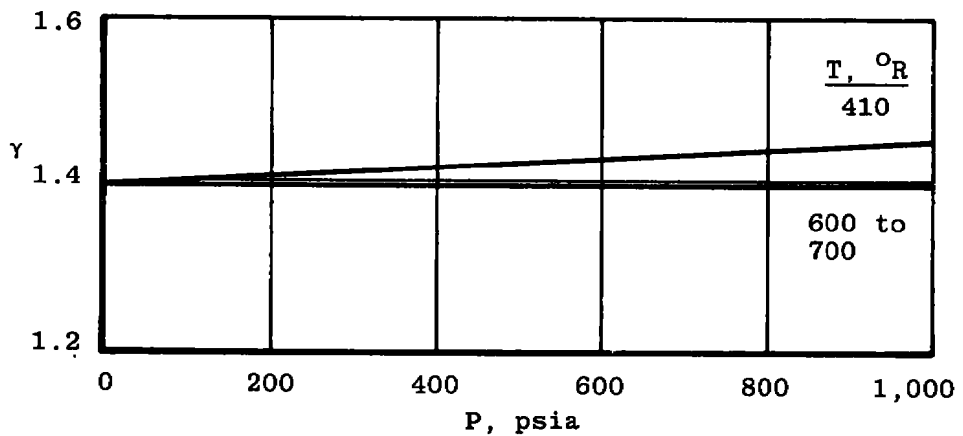
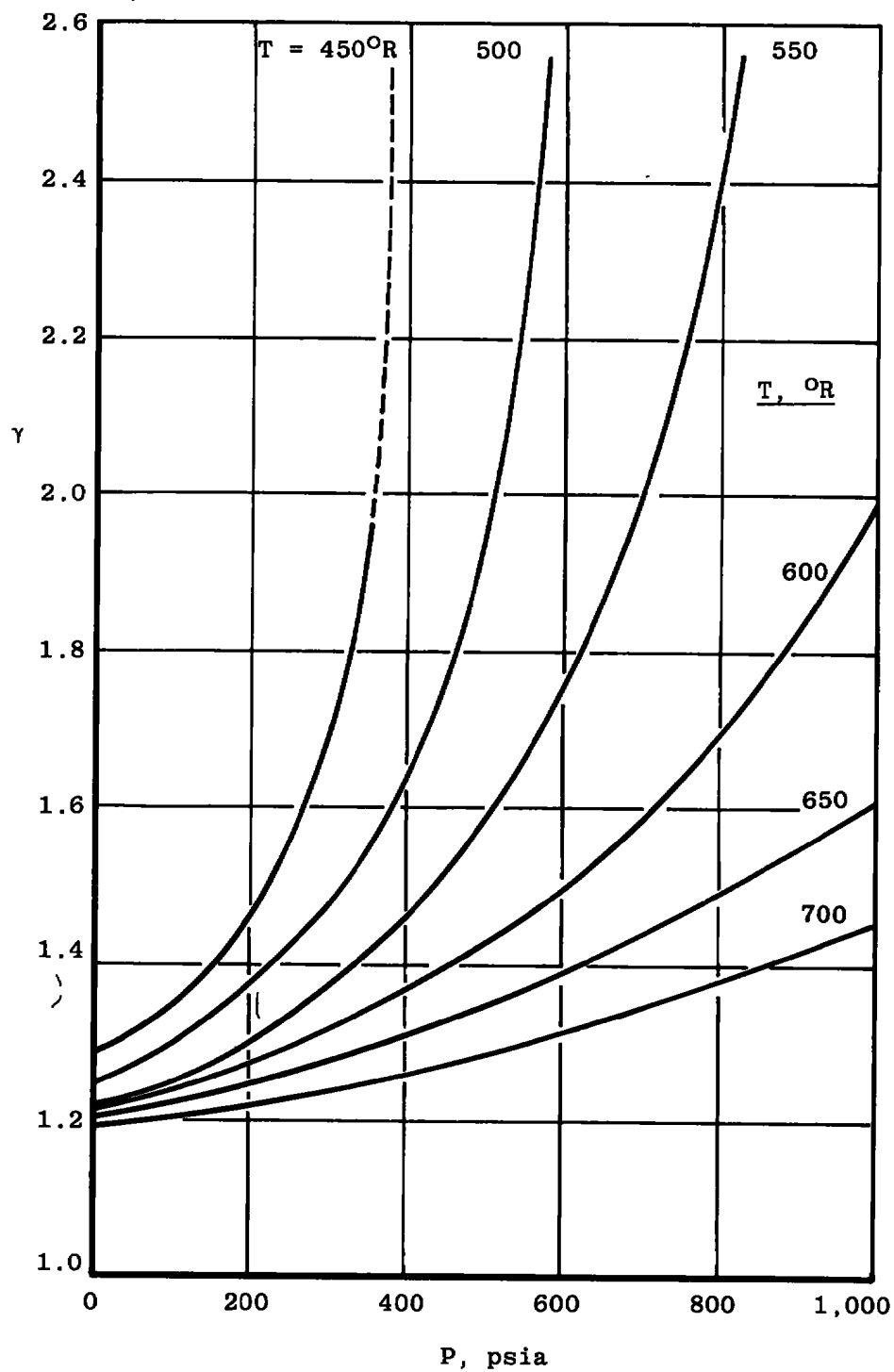
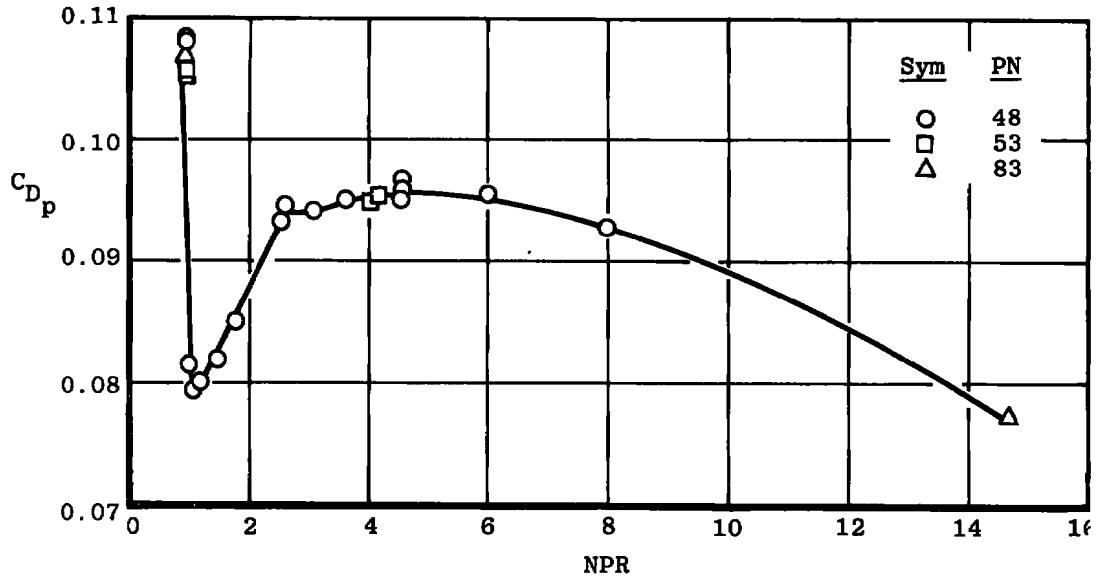
a. Nitrogen (N_2)b. Hydrogen (H_2)

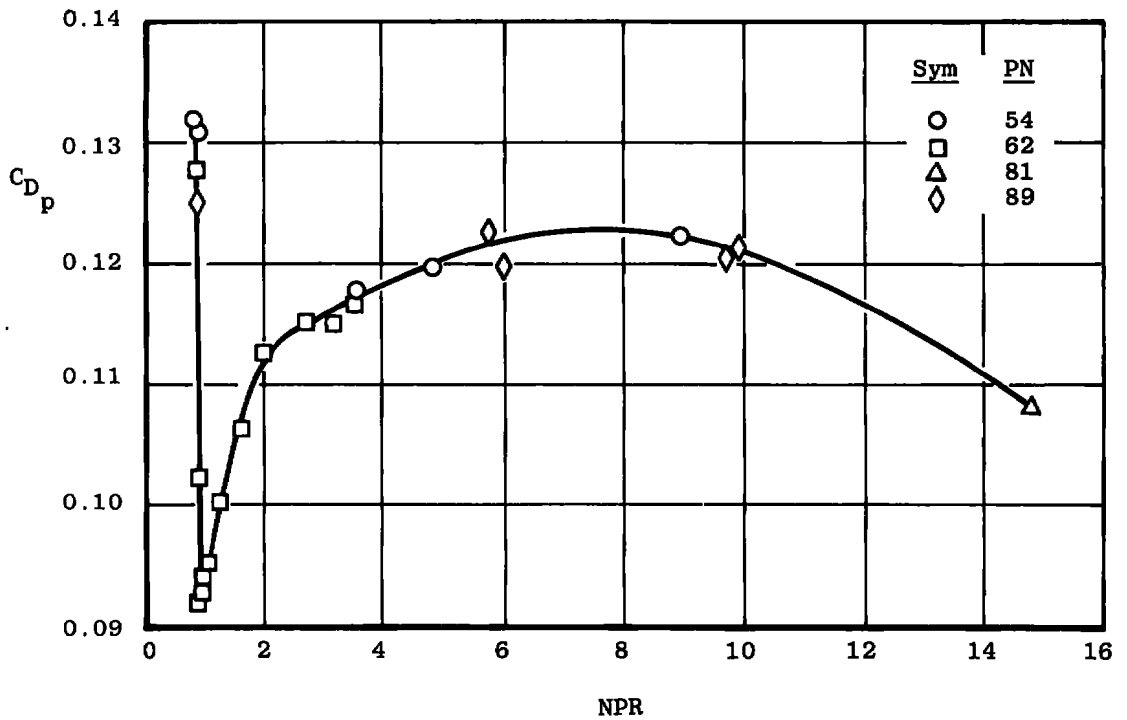
Figure 4. Real gas effects on the specific heat ratio for N_2 , H_2 , and C_2H_4 gases.



c. Ethylene (C_2H_4)
Figure 4. Concluded.

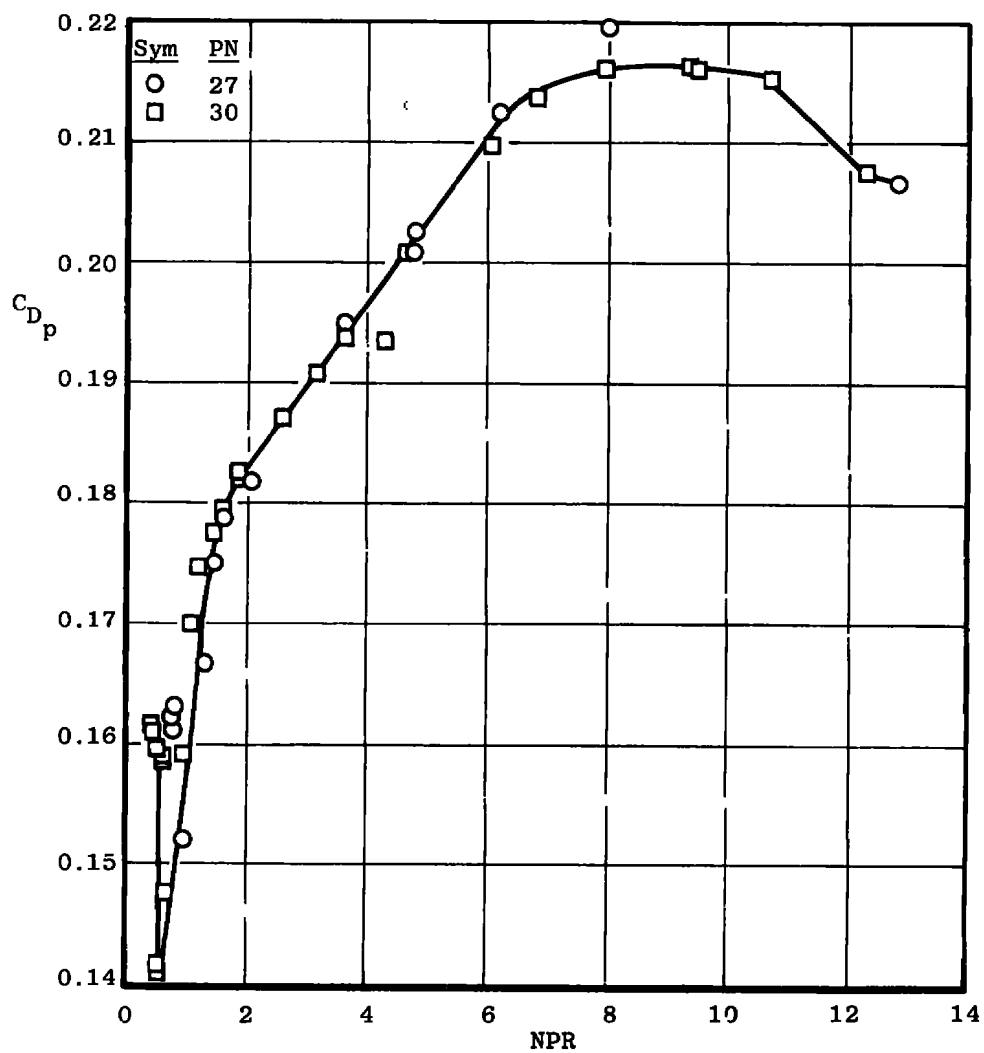


a. $M_\infty = 0.6$



b. $M_\infty = 0.9$

Figure 5. Data repeatability for the 25-deg boattail.



c. $M_\infty = 1.2$
Figure 5. Concluded.

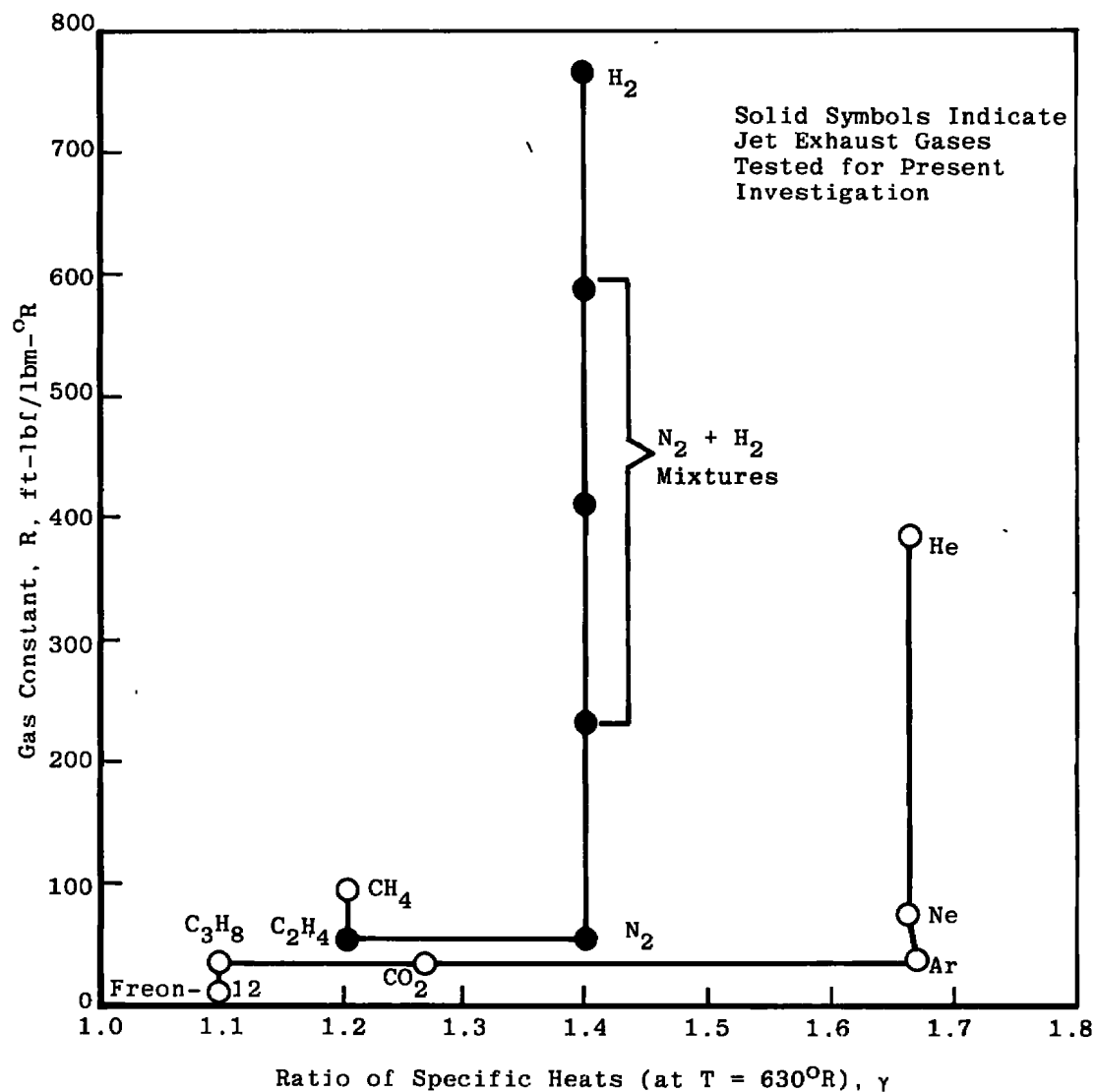
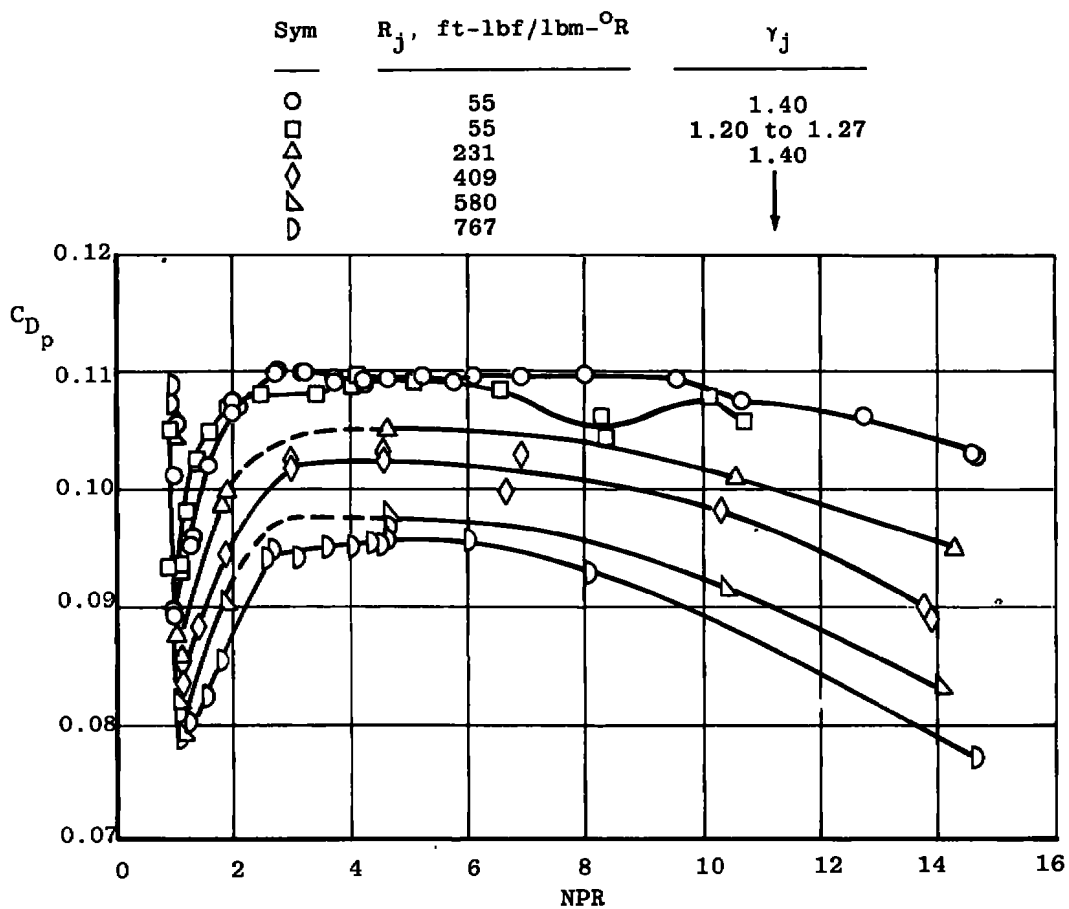
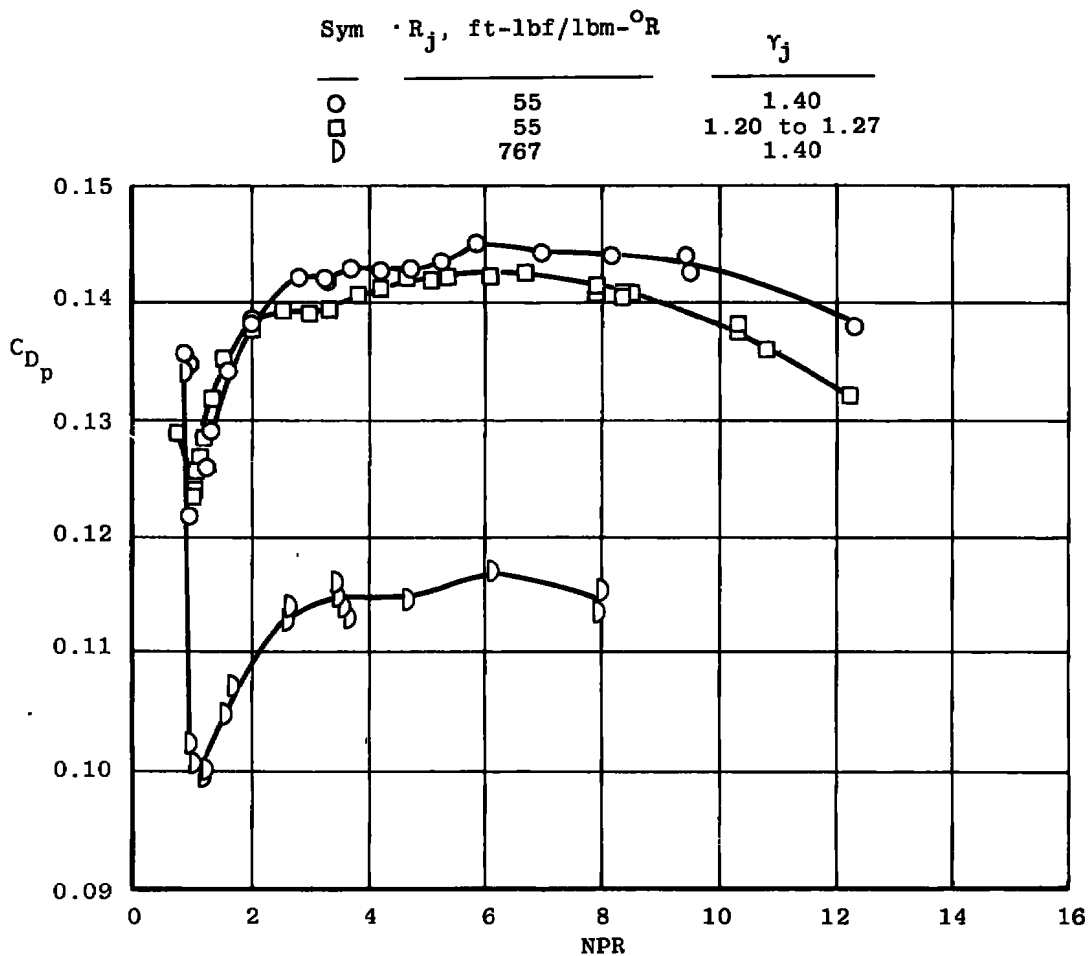


Figure 6. Gas constant and specific heat ratio for jet exhaust gases.

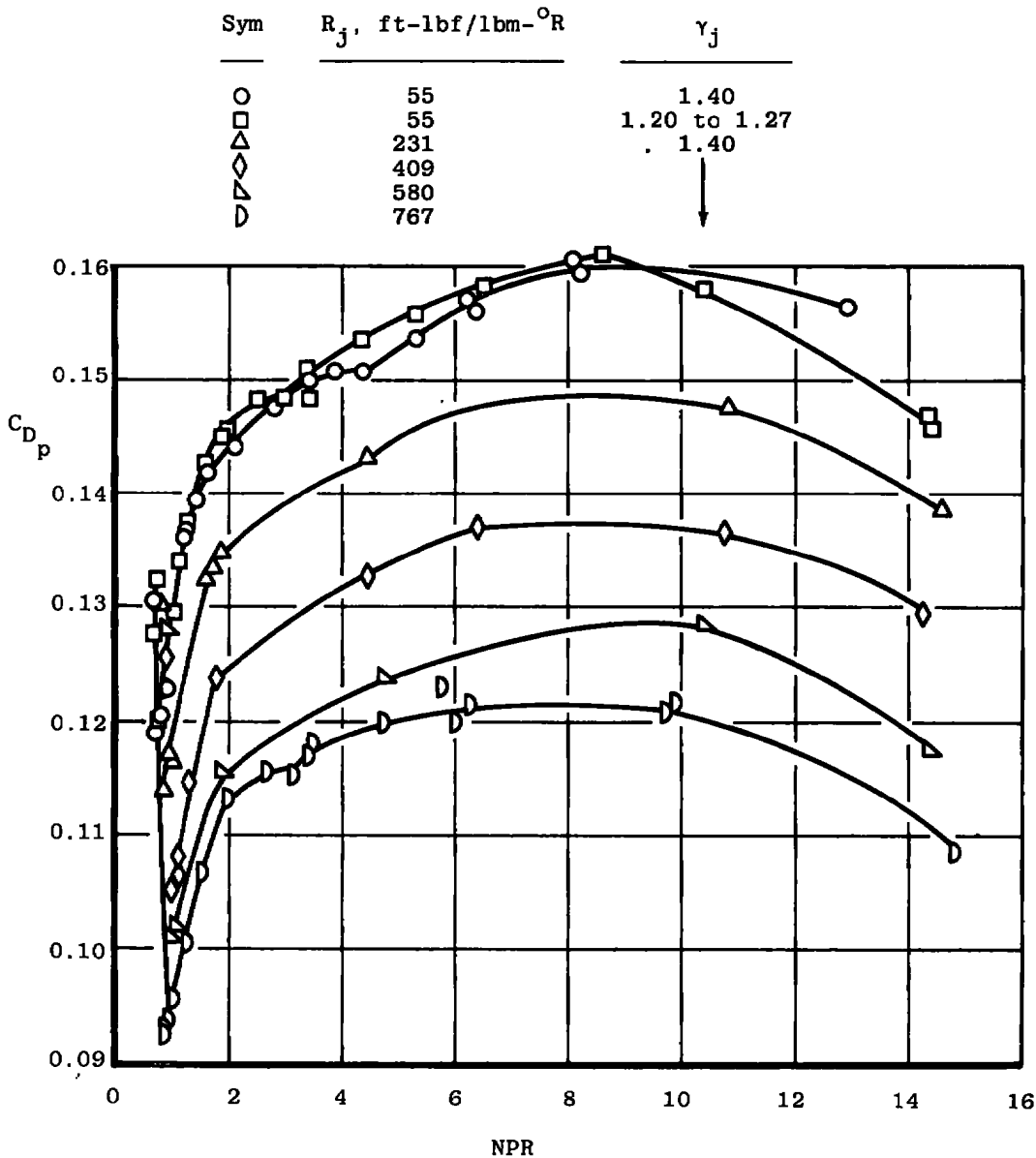


a. $M_\infty = 0.6$

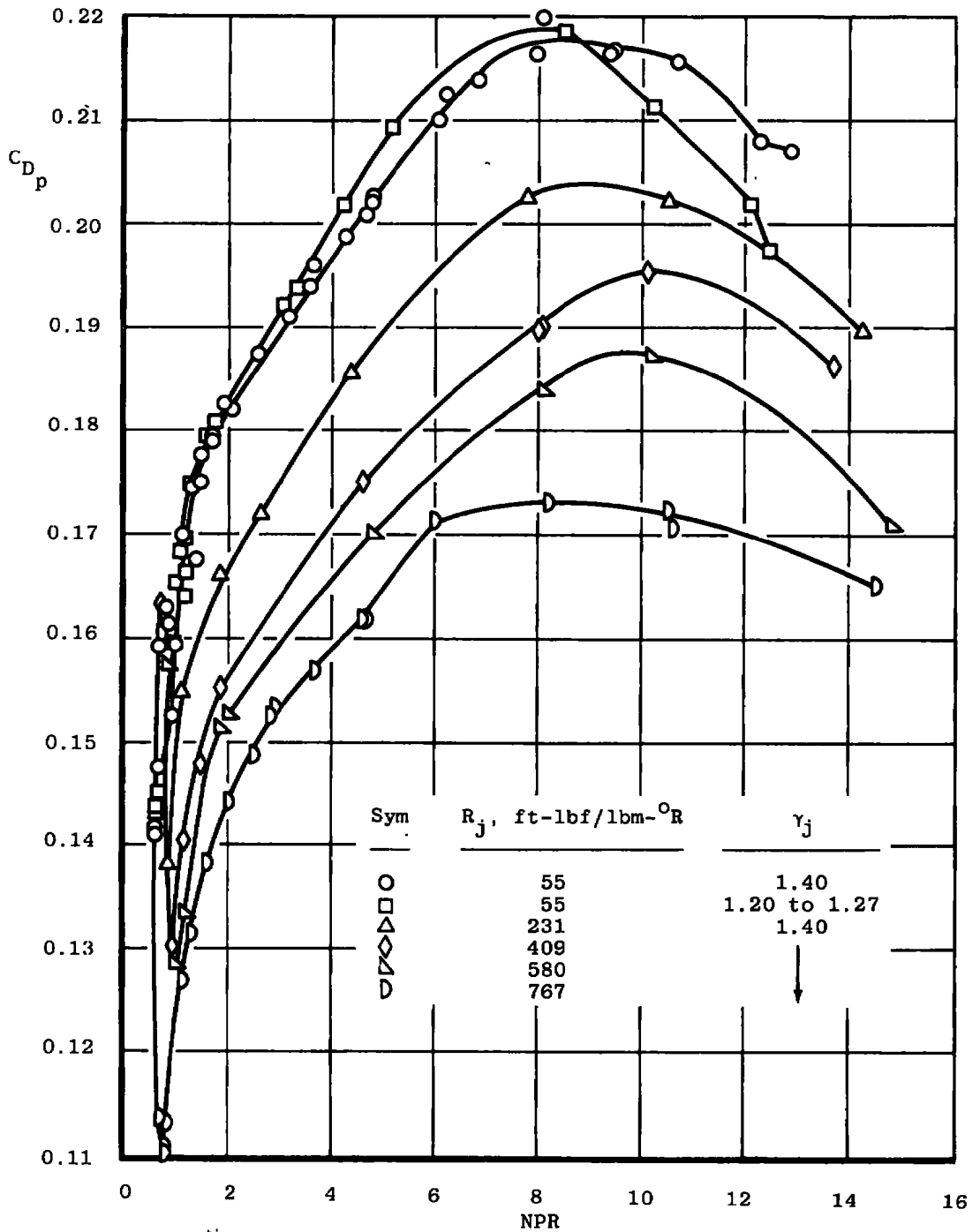
Figure 7. The effects of γ_j and R_j on afterbody pressure drag coefficient for the 25-deg boattail, $A_e/A^* = 1.271$, $T_{tj} = 630^\circ\text{R}$.



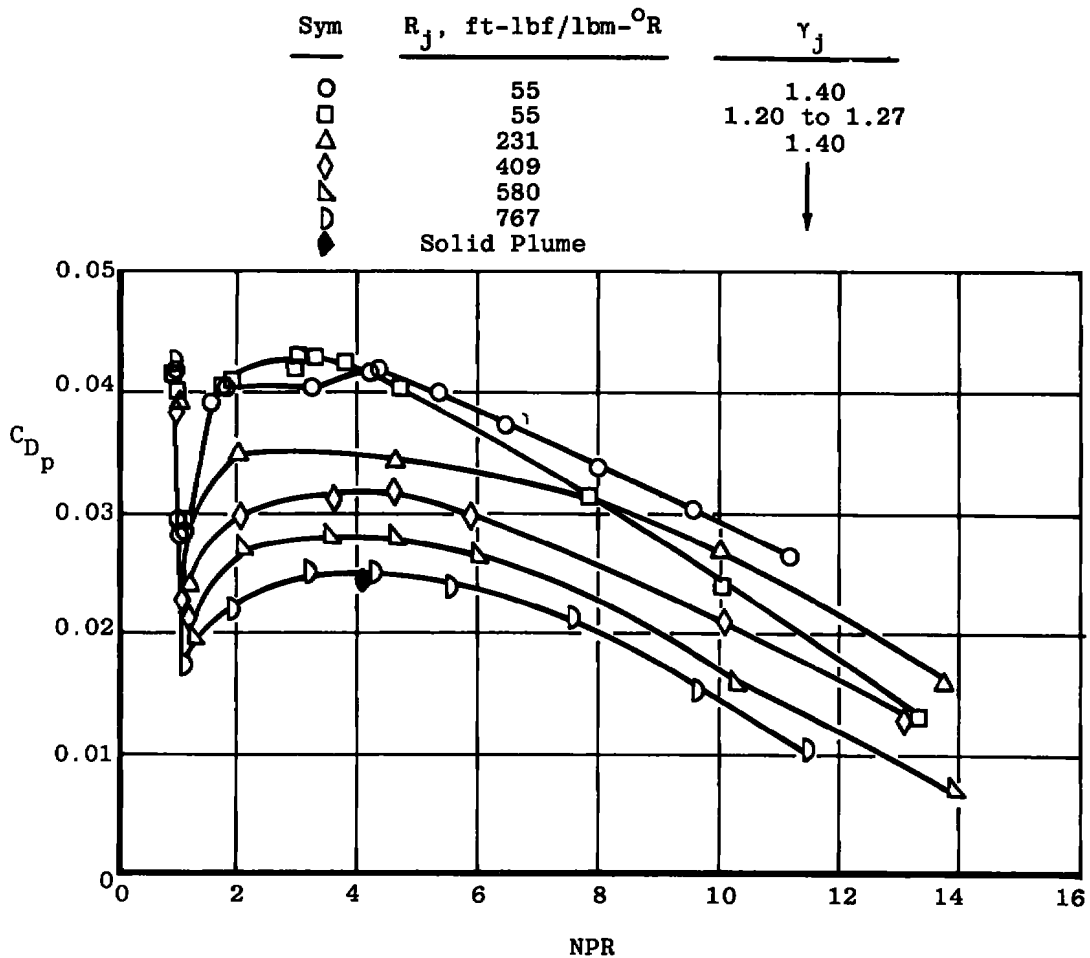
b. $M_{\infty} = 0.8$
Figure 7. Continued.



c. $M_\infty = 0.9$
Figure 7. Continued.

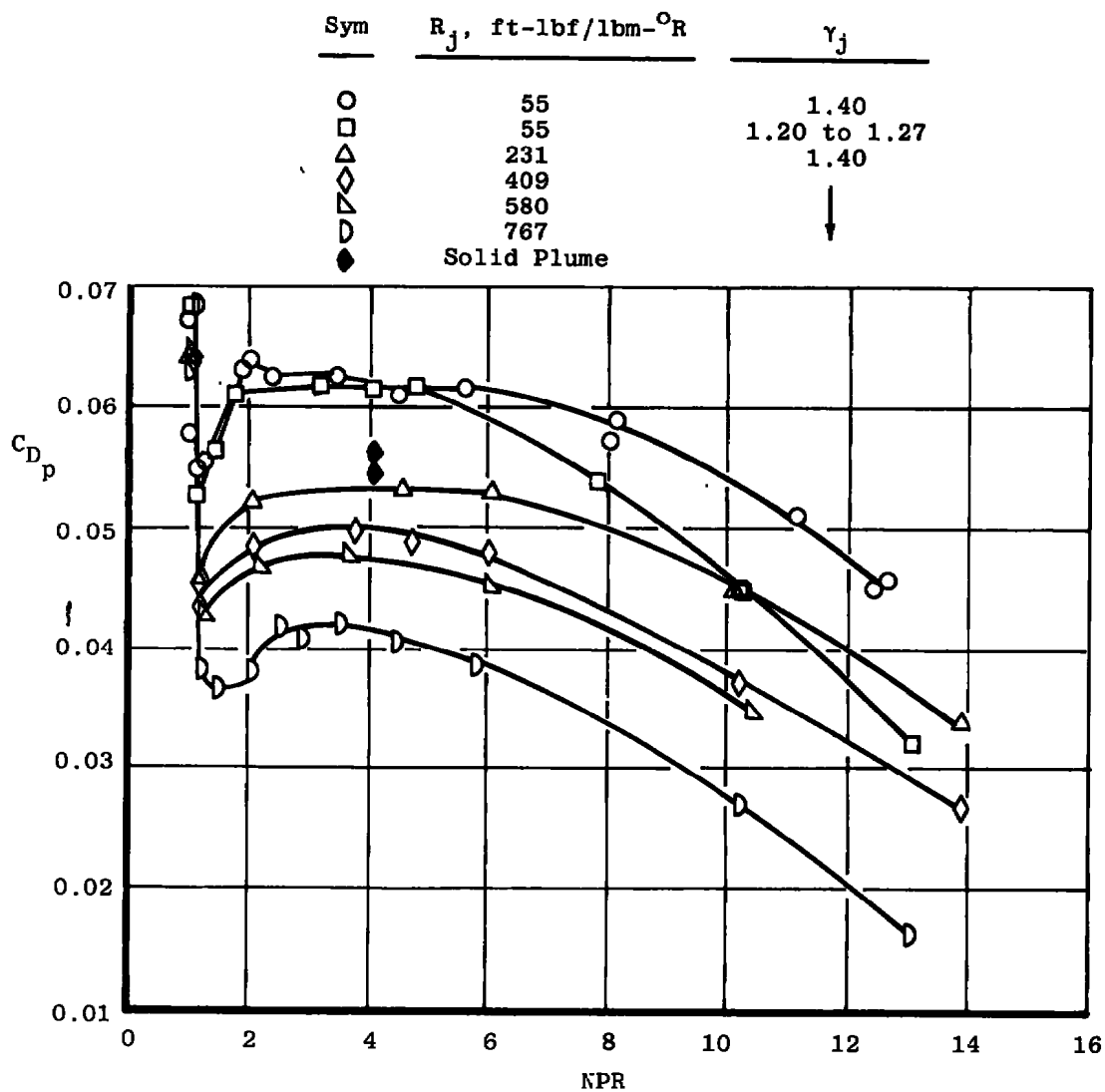


d. $M_\infty = 1.2$
Figure 7. Concluded.

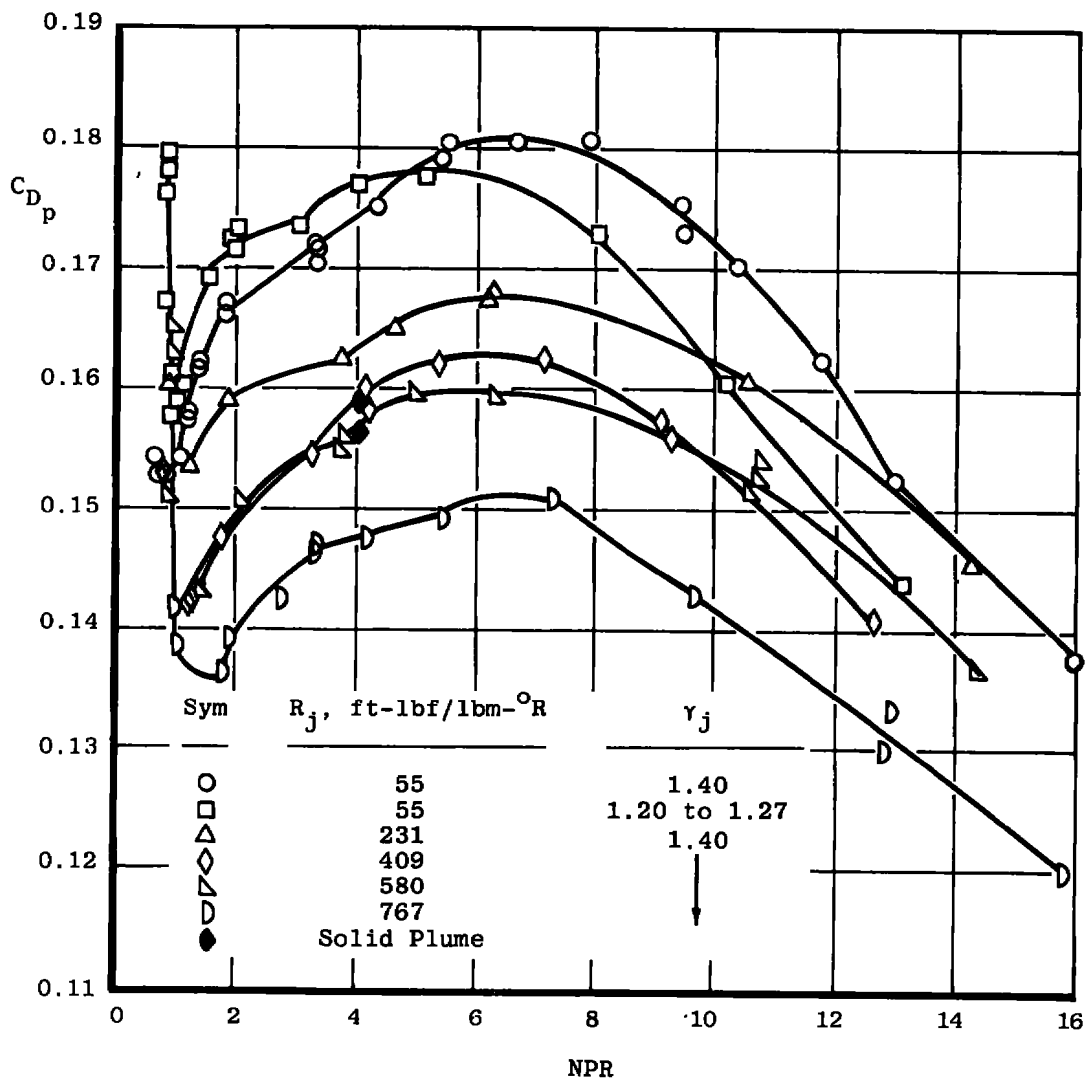


a. $M_{\infty} = 0.6$

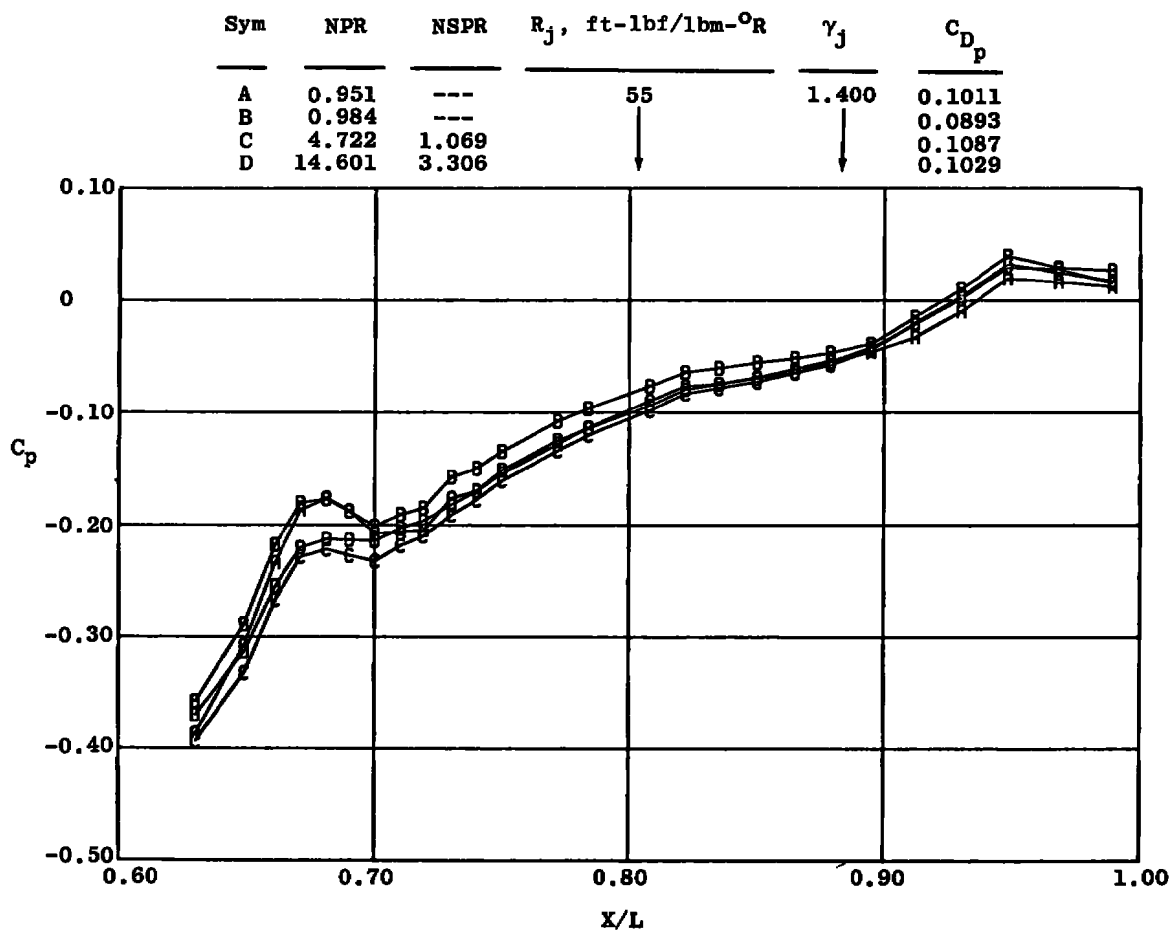
Figure 8. The effects of γ_j and R_j on afterbody pressure drag coefficient for the 15-deg boattail, $A_e/A^* = 1.226$, $T_{tj} = 630^{\circ}$ R.



b. $M_{\infty} = 0.9$
Figure 8. Continued.



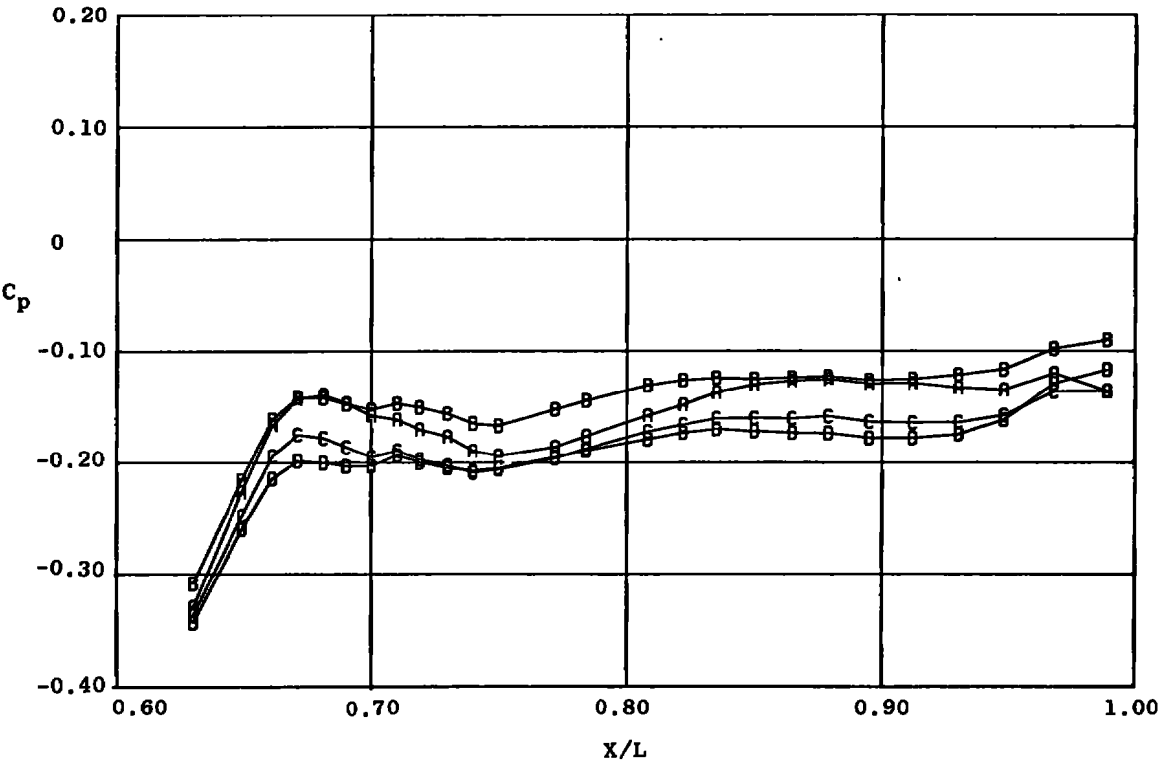
c. $M_{\infty} = 1.2$
Figure 8. Concluded.



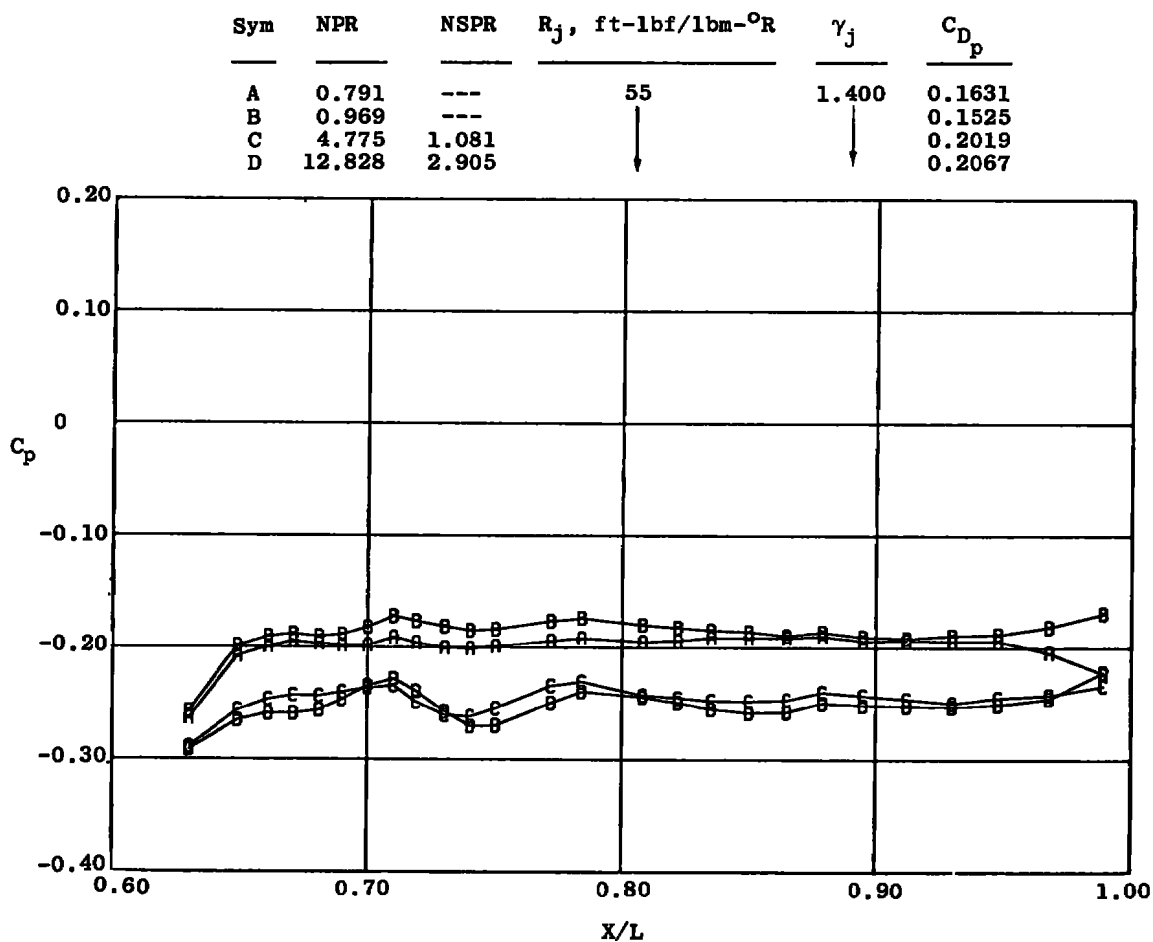
a. $M_\infty = 0.6$

Figure 9. Nozzle total pressure ratio effects on afterbody pressure distributions for the 25-deg boattail, $A_0/A^* = 1.271$, $T_{tj} = 630^{\circ}$ R.

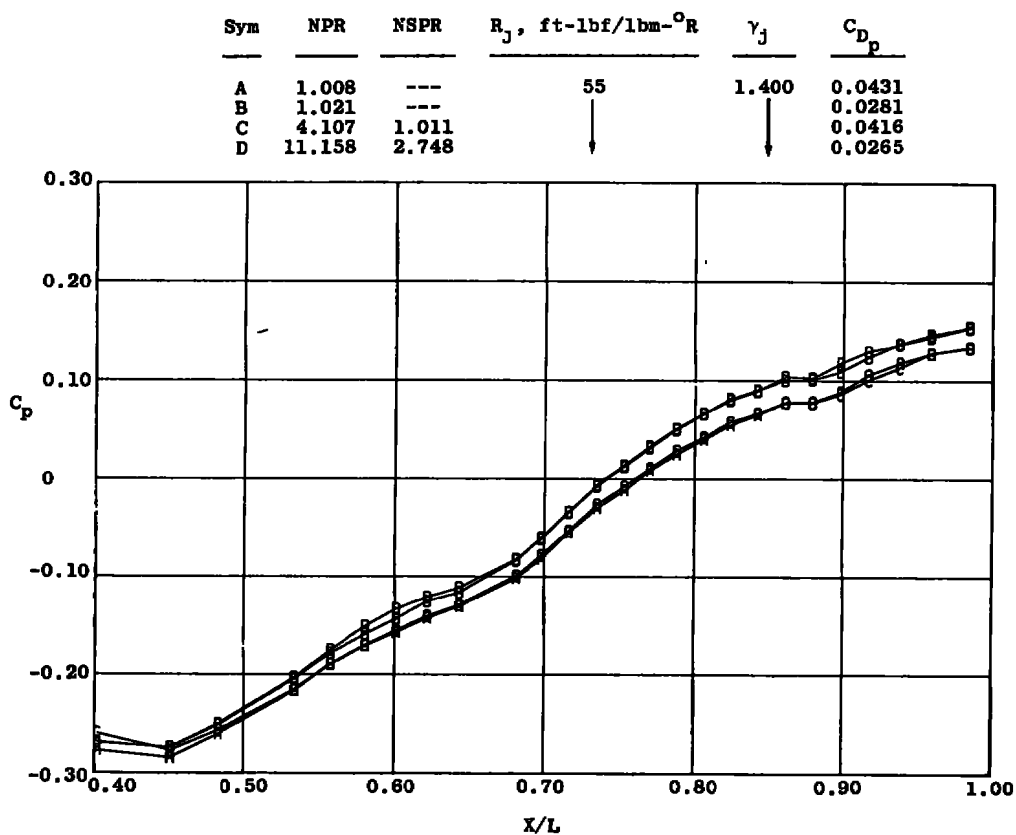
Sym	NPR	NSPR	R_j , ft-lbf/lbm ^o R	γ_j	C_{Dp}
A	0.724	---	55	1.400	0.1314
B	0.769	---	↓	↓	0.1181
C	4.392	0.995			0.1506
D	12.944	2.931			0.1563



b. $M_\infty = 0.9$
Figure 9. Continued.

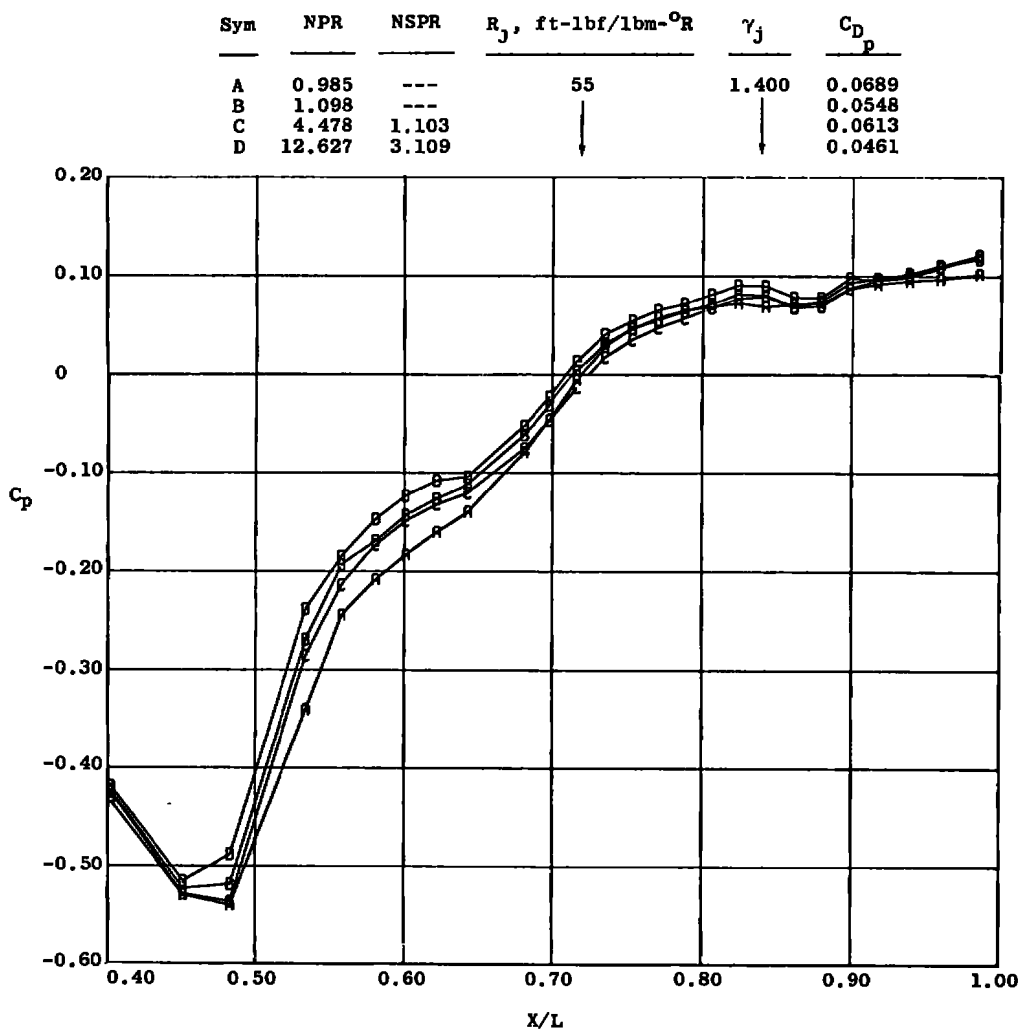


c. $M_\infty = 1.2$
Figure 9. Concluded.



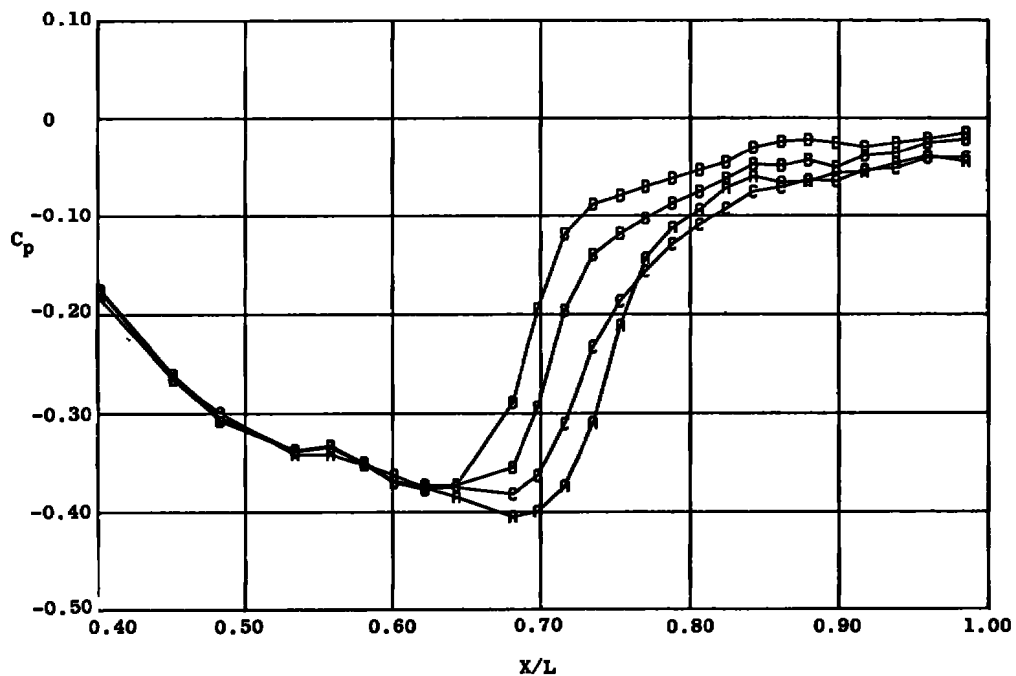
a. $M_\infty = 0.6$

Figure 10. Nozzle total pressure ratio effects on afterbody pressure distributions for the 15-deg boattail, $A_0/A^* = 1.226$, $T_{tj} = 630^\circ\text{R}$.



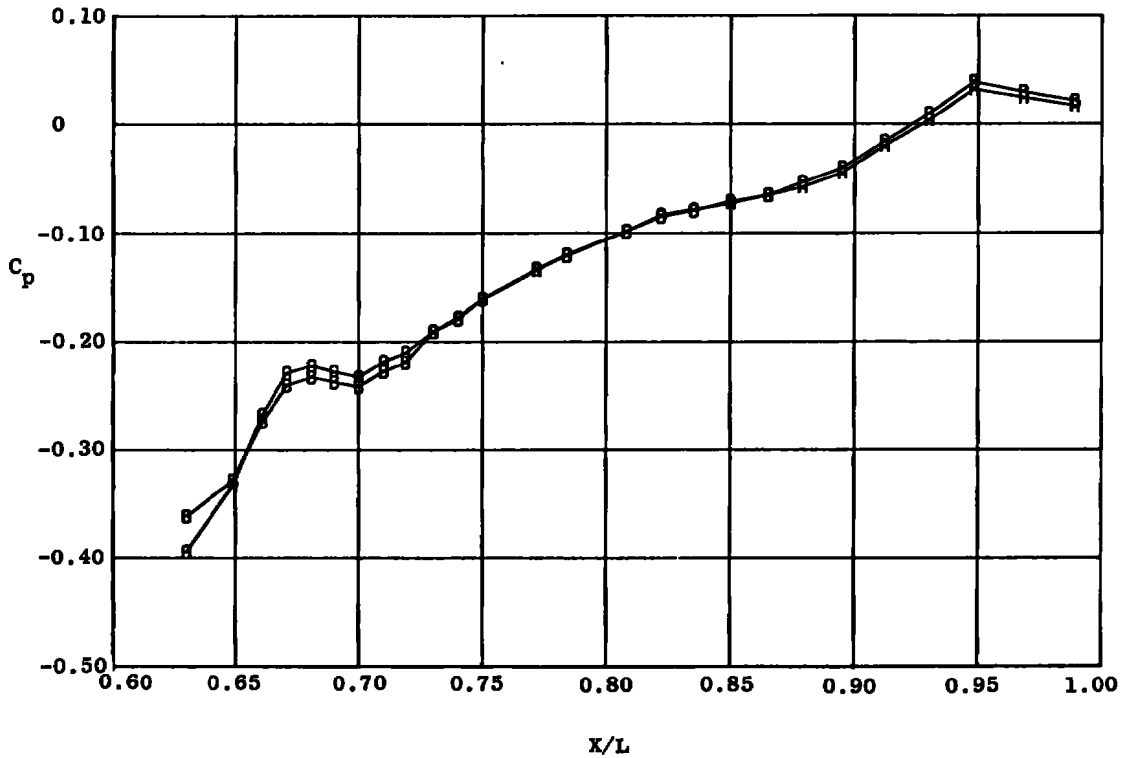
b. $M_\infty = 0.9$
Figure 10. Continued.

Sym	NPR	NSPR	R_j , ft-lbf/lbm ⁰ R	γ_j	C_{Dp}
A	0.856	---	55	1.400	0.1796
B	1.096	---	↓	↓	0.1541
C	4.366	1.075	↓	↓	0.1750
D	15.990	3.937	↓	↓	0.1379



c. $M_\infty = 1.2$
Figure 10. Concluded.

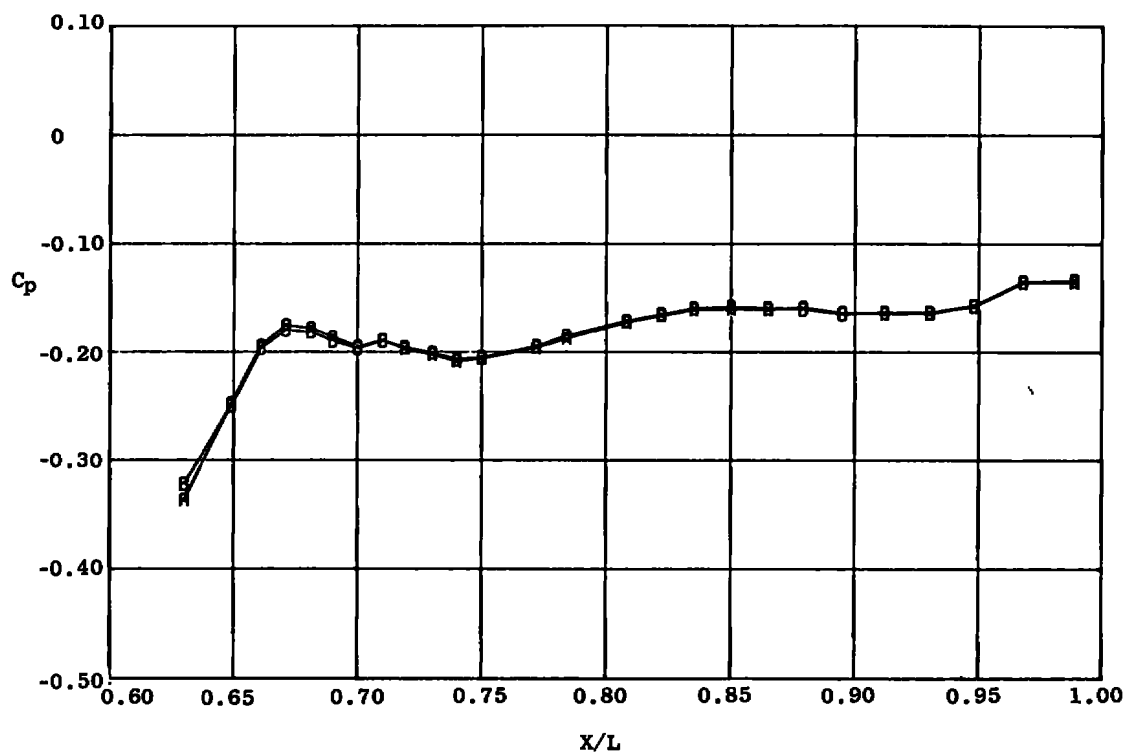
Sym	NPR	NSPR	R_j , ft-lbf/lbm-°R	γ_j	C_{D_p}
A	4.722	1.069	55	1.400	0.1087
B	5.081	1.319	55	1.224	0.1089



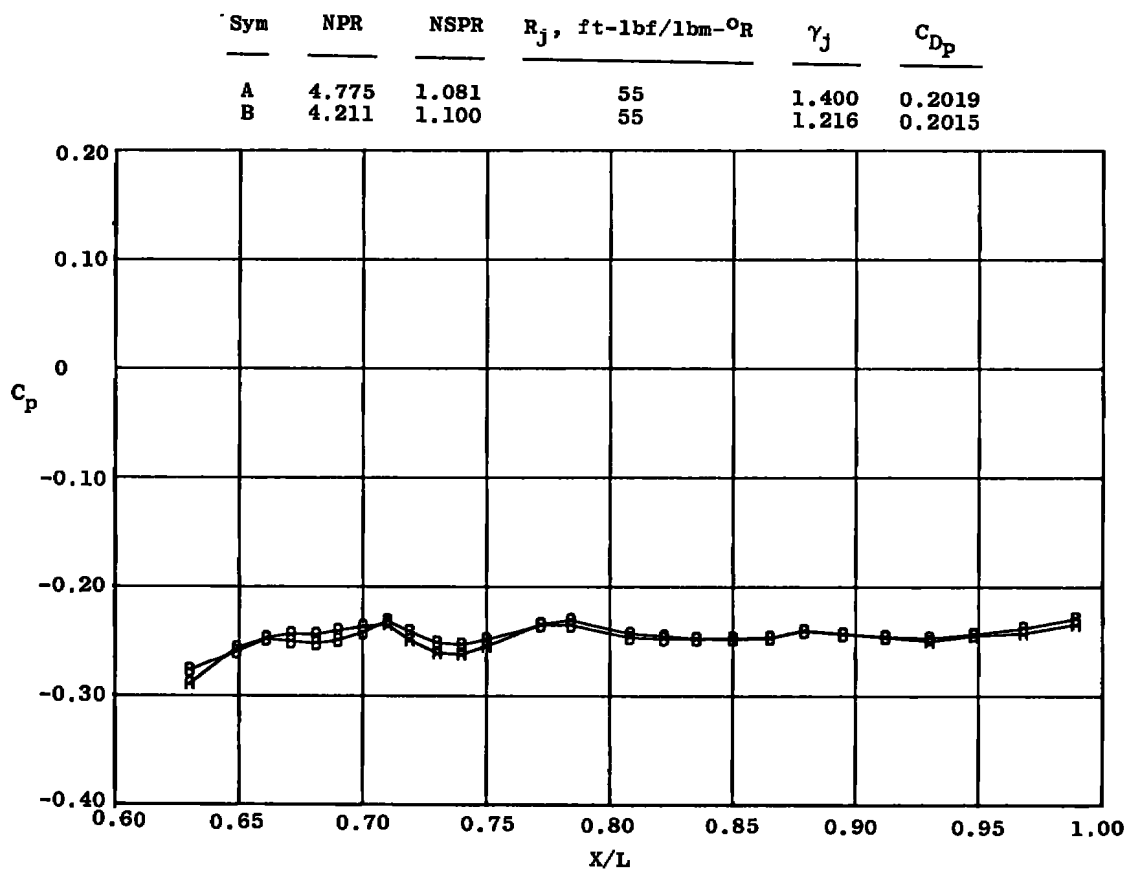
a. $M_\infty = 0.6$

Figure 11. Jet specific heat ratio effects on afterbody pressure distributions at nozzle design conditions for the 25-deg boattail, $A_e/A^* = 1.271$, $T_{tj} = 630^\circ\text{R}$.

Sym	NPR	NSPR	R_j , ft-lbf/lbm- $^{\circ}$ R	γ_j	C_{D_p}
A	4.392	0.995	55	1.400	0.1506
B	3.837	1.013	55	1.204	0.1502

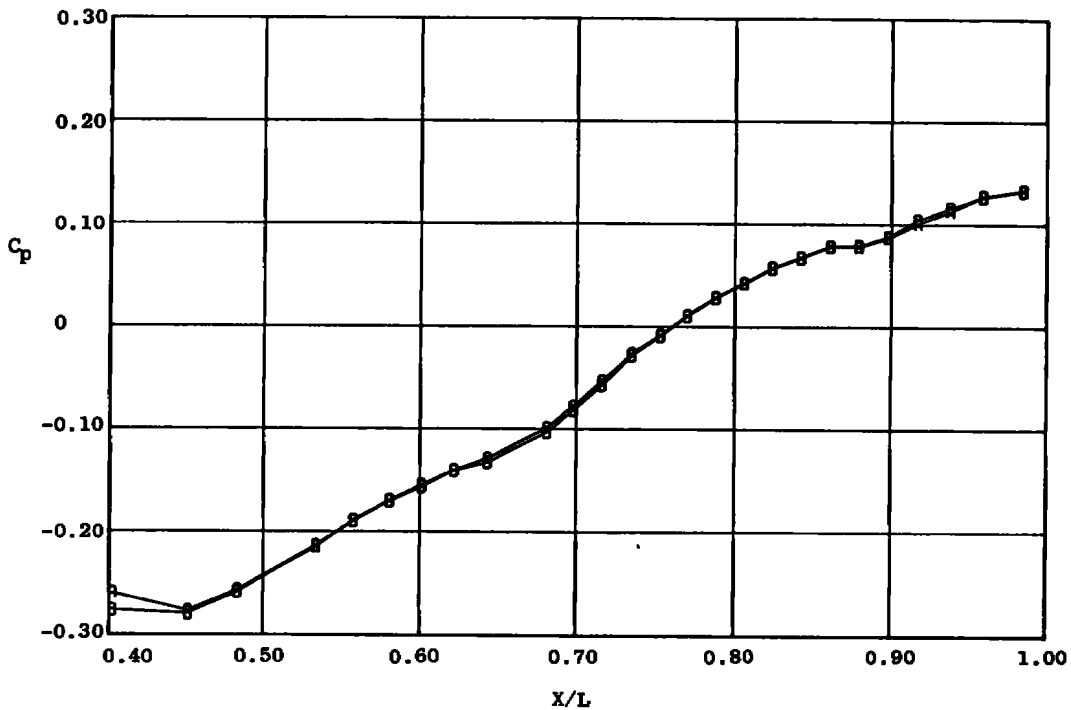


b. $M_{\infty} = 0.9$
Figure 11. Continued.



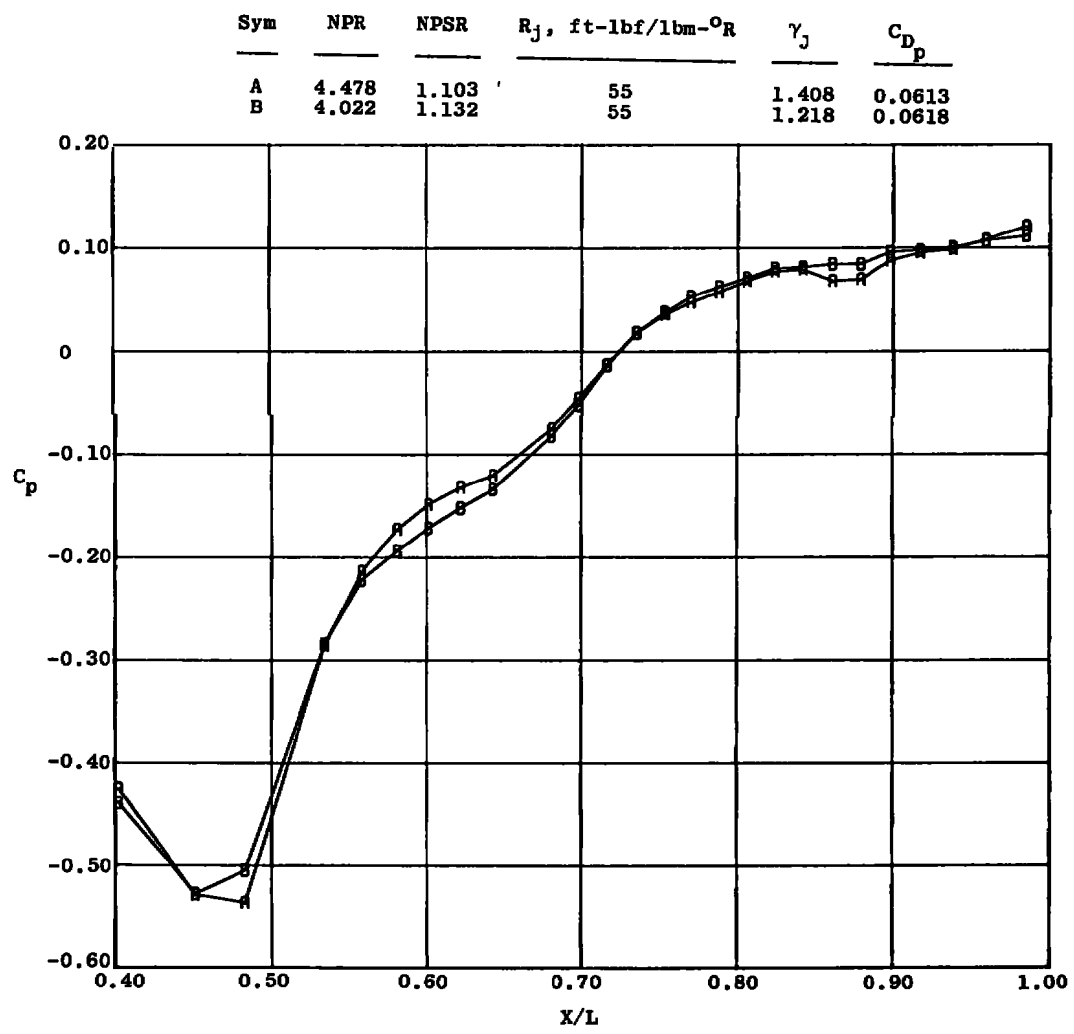
c. $M_{\infty} = 1.2$
 Figure 11. Concluded.

Sym	NPR	NSPR	R_j , ft-lbf/lbm-°R	γ_j	C_{D_p}
A	4.107	1.011	55	1.400	0.0416
B	3.839	1.082	55	1.215	0.0426



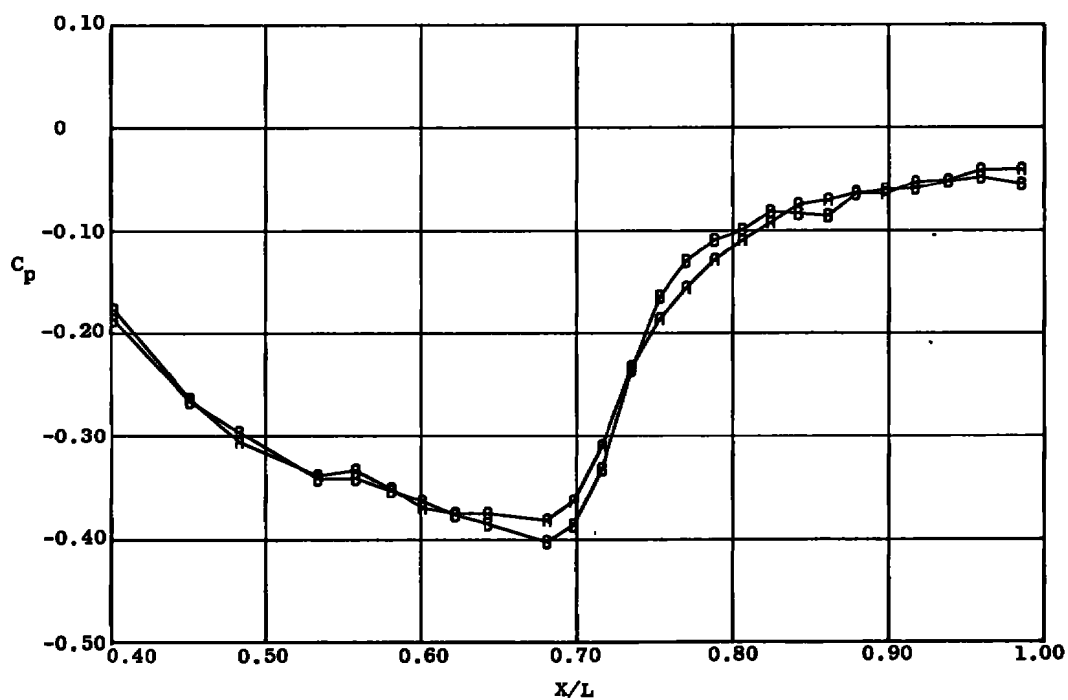
a. $M_\infty = 0.6$

Figure 12. Jet specific heat ratio effects on afterbody pressure distributions at nozzle design conditions for the 15-deg boattail, $A_0/A^* = 1.226$, $T_{tj} = 630^\circ\text{R}$.

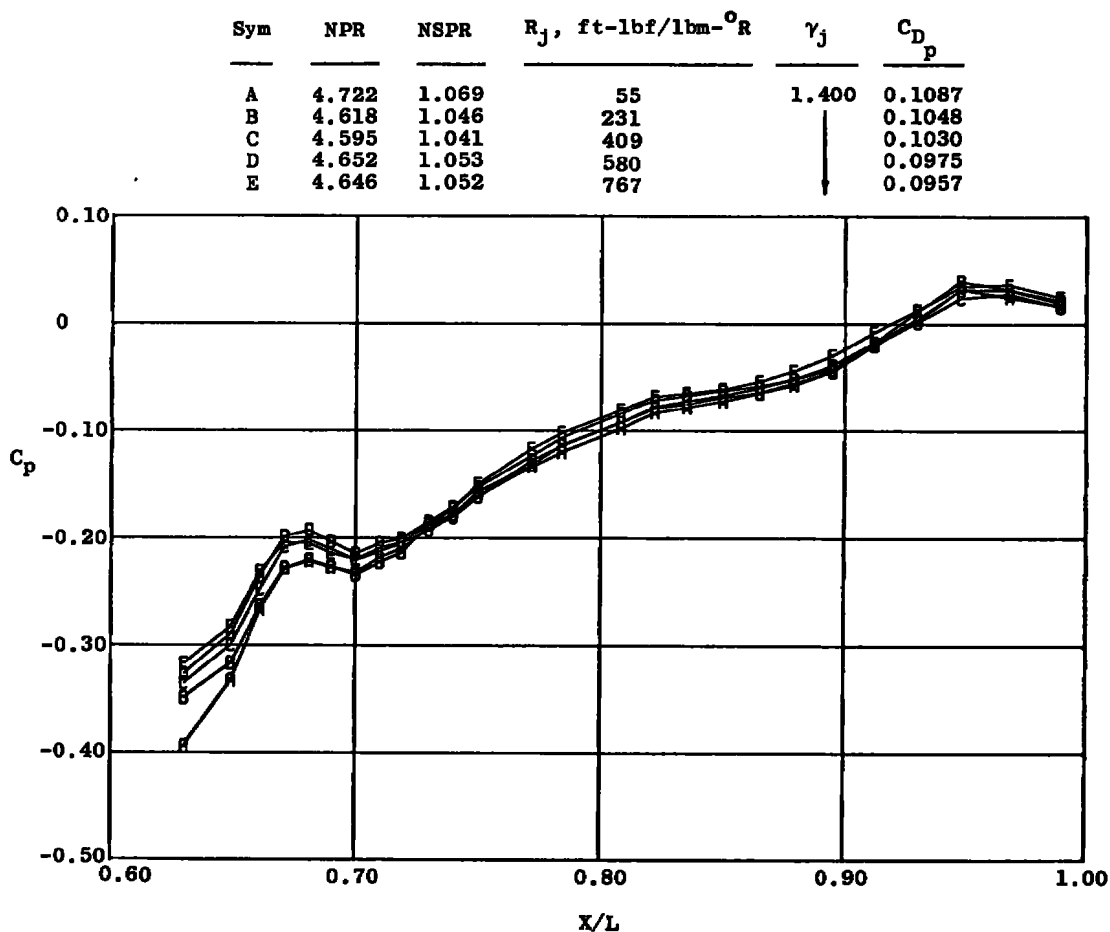


b. $M_{\infty} = 0.9$
Figure 12. Continued.

Sym	NPR	NSPR	R_j , ft-lbf/lbm- $^{\circ}$ R	γ_j	C_{D_p}
A	4.366	1.075	55	1.400	0.1750
B	4.009	1.132	55	1.213	0.1768

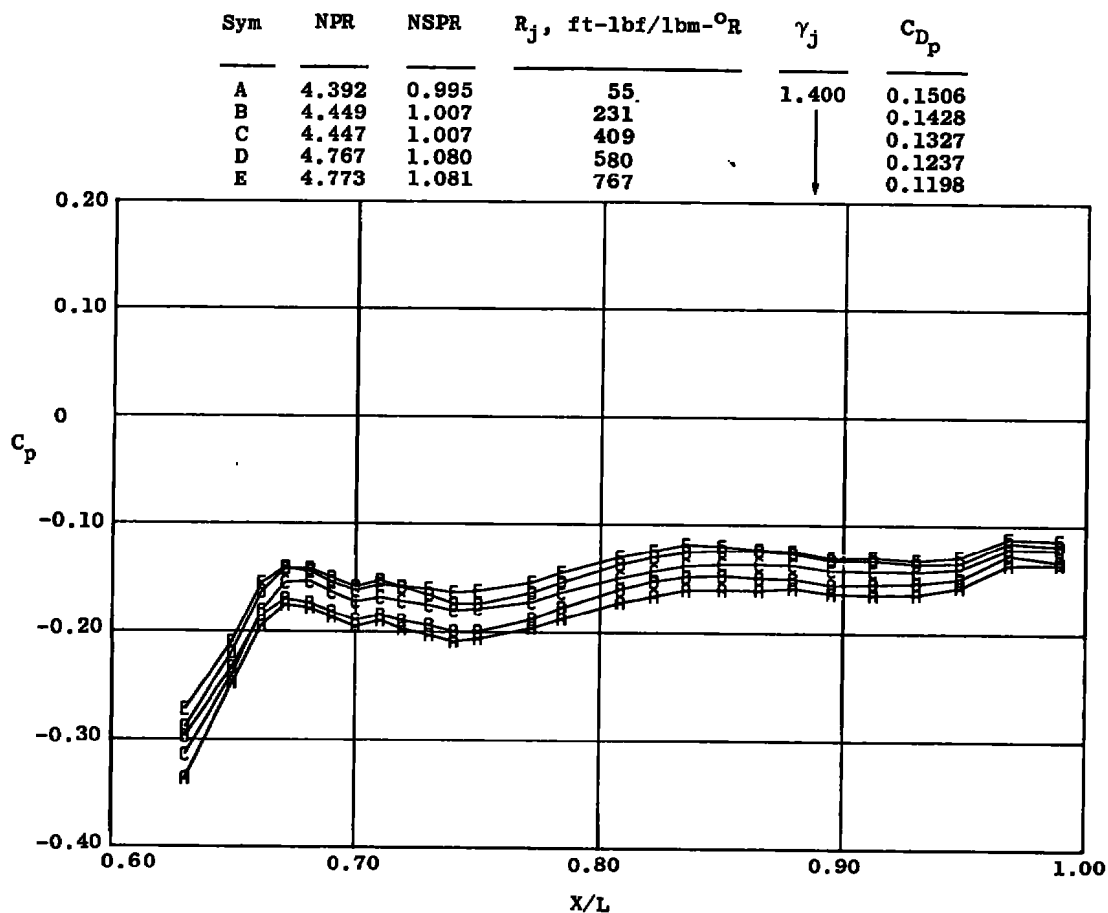


c. $M_{\infty} = 1.2$
Figure 12. Concluded.

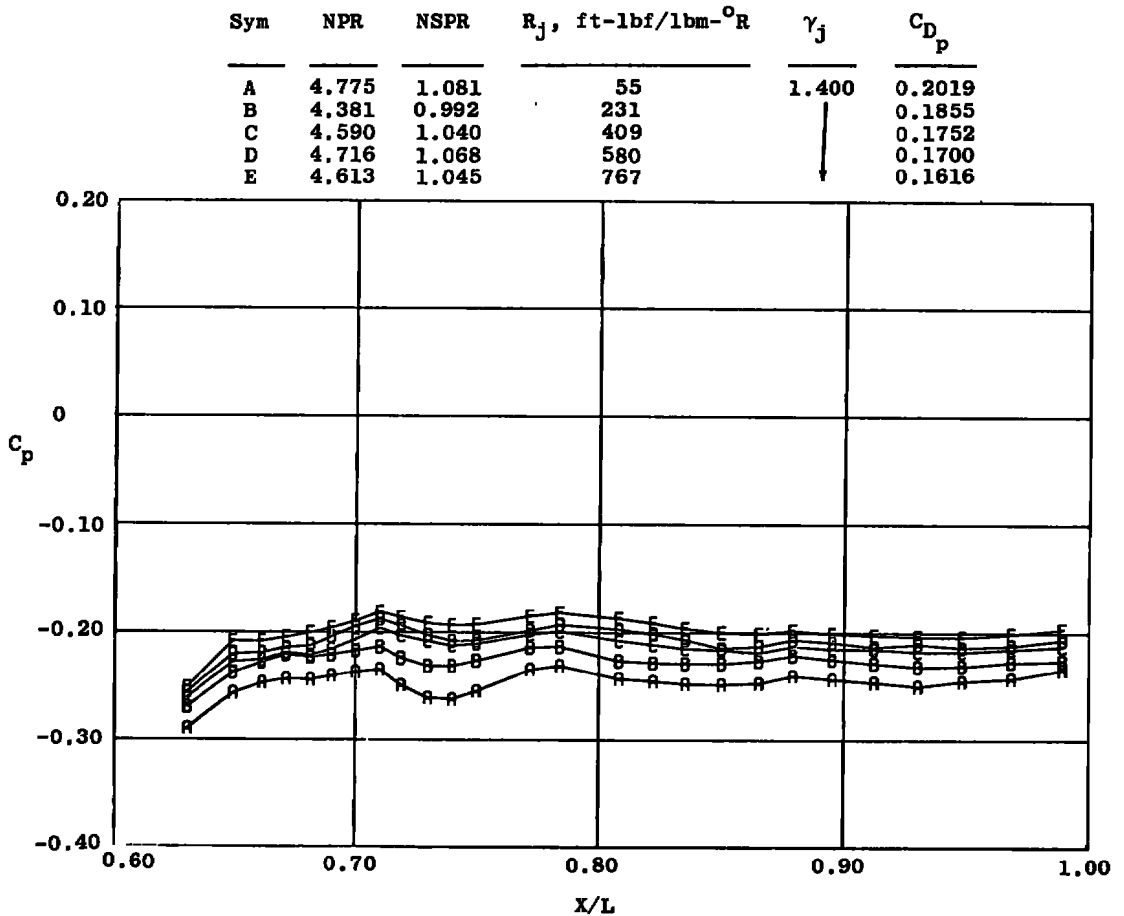


a. $M_\infty = 0.6$

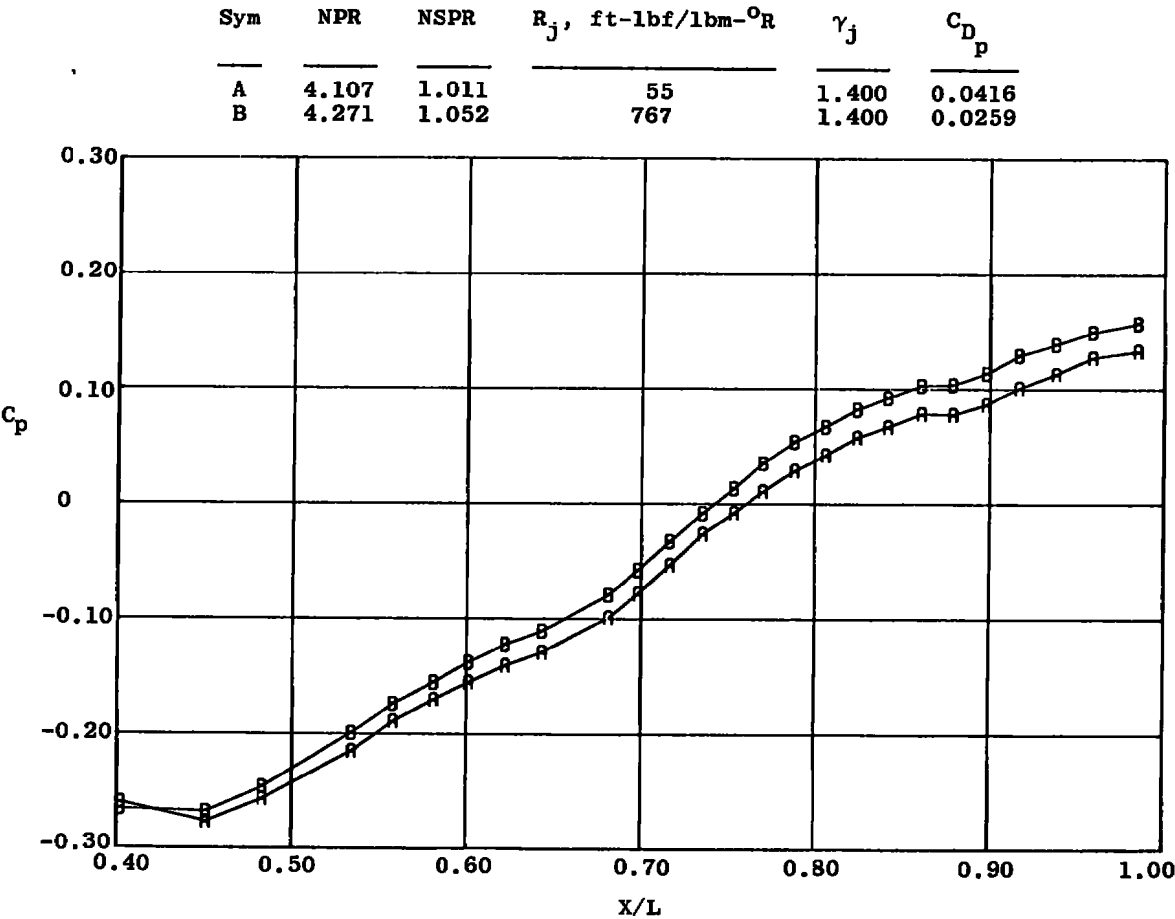
Figure 13. Jet gas constant effects on afterbody pressure distributions at nozzle design conditions for the 25-deg boattail, $A_b/A^* = 1.271$, $T_{tj} = 630^\circ R$.



b. $M_\infty = 0.9$
Figure 13. Continued.



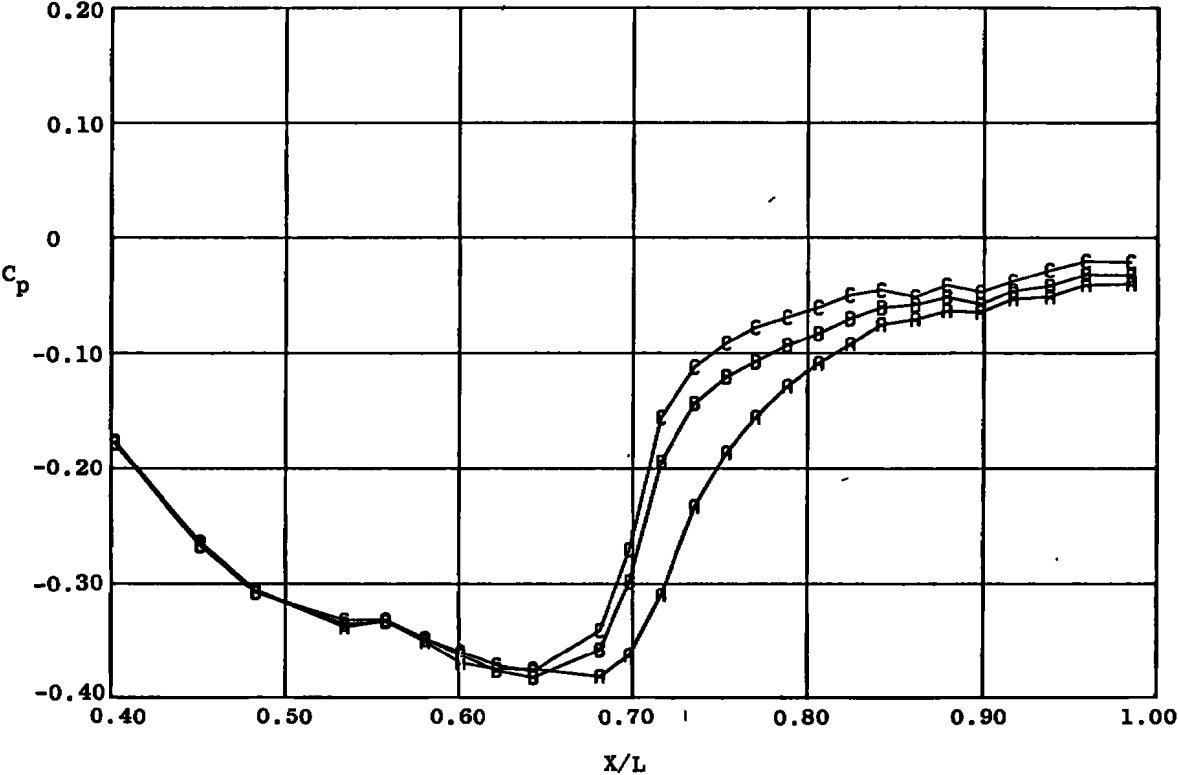
c. $M_{\infty} = 1.2$
 Figure 13. Concluded.



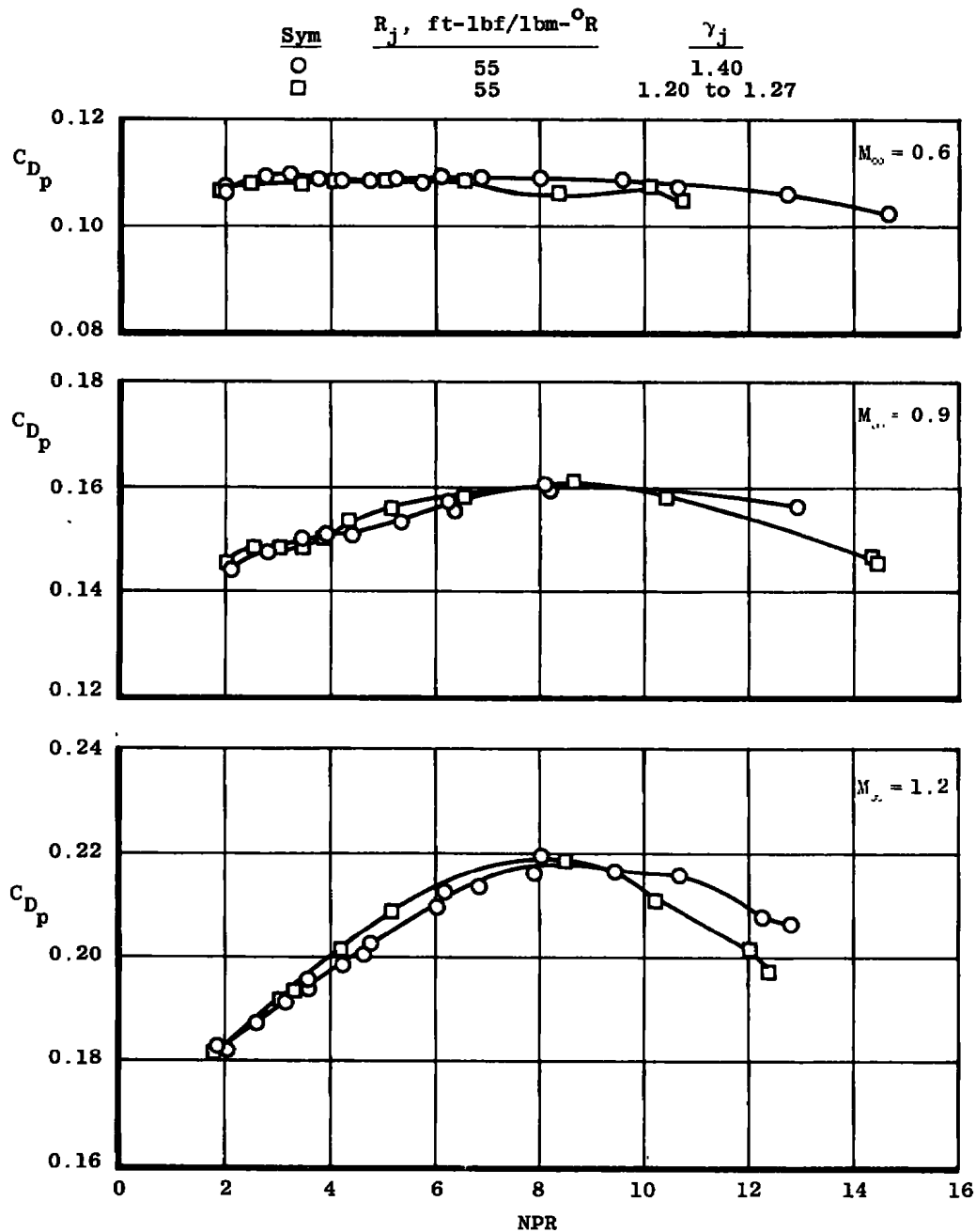
a. $M_\infty = 0.6$

Figure 14. Jet gas constant effects on afterbody pressure distributions at nozzle design conditions for the 15-deg boattail, $A_b/A^* = 1.226$, $T_{tj} = 630^\circ\text{R}$.

Sym	NPR	NSPR	R_j , ft-lbf/lbm- $^{\circ}$ R	γ_j	C_{D_p}
A	4.366	1.075	55	1.400	0.1750
B	4.215	1.038	409		0.1581
C	4.163	1.025	767		0.1476

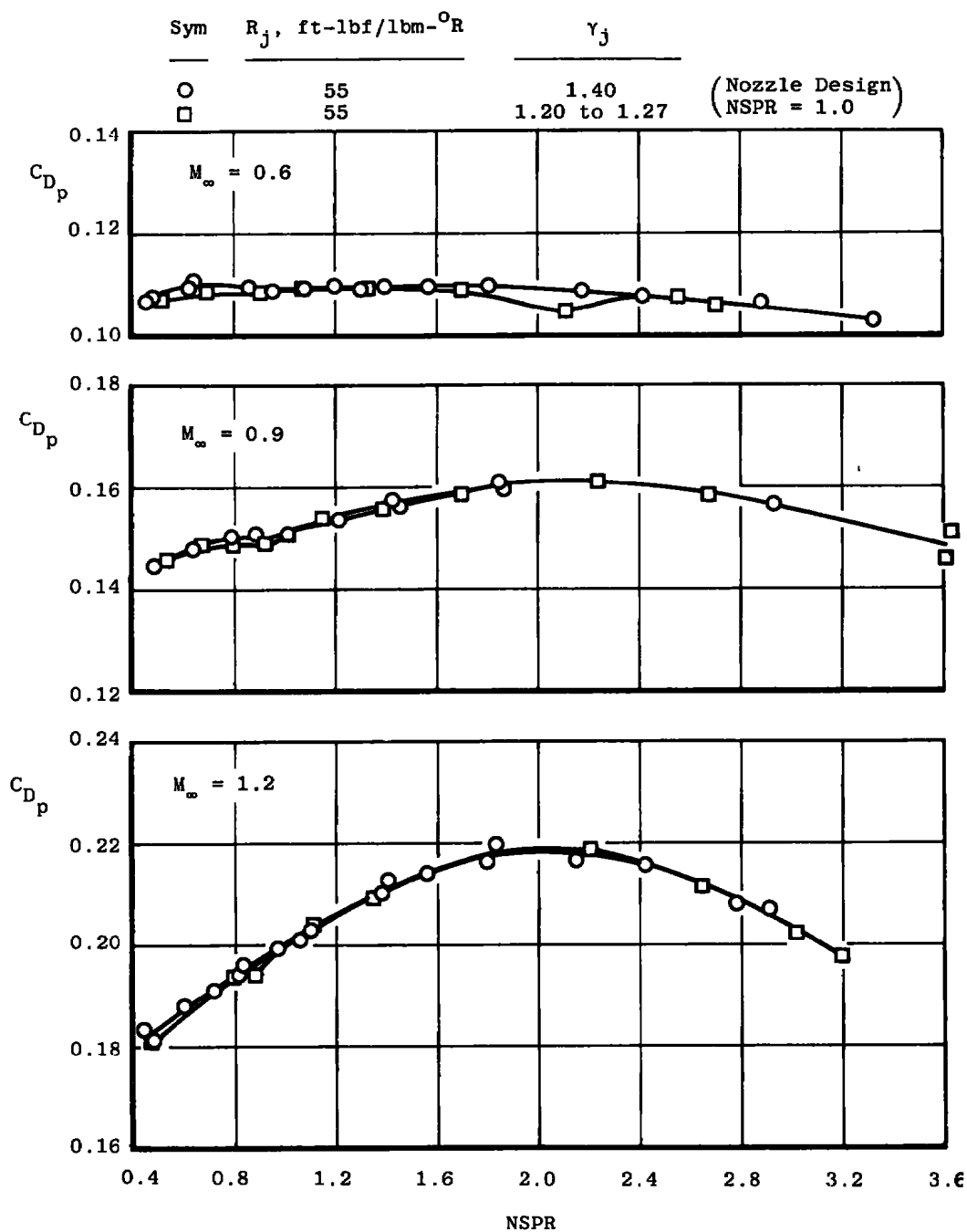


b. $M_{\infty} = 1.2$
Figure 14. Concluded.

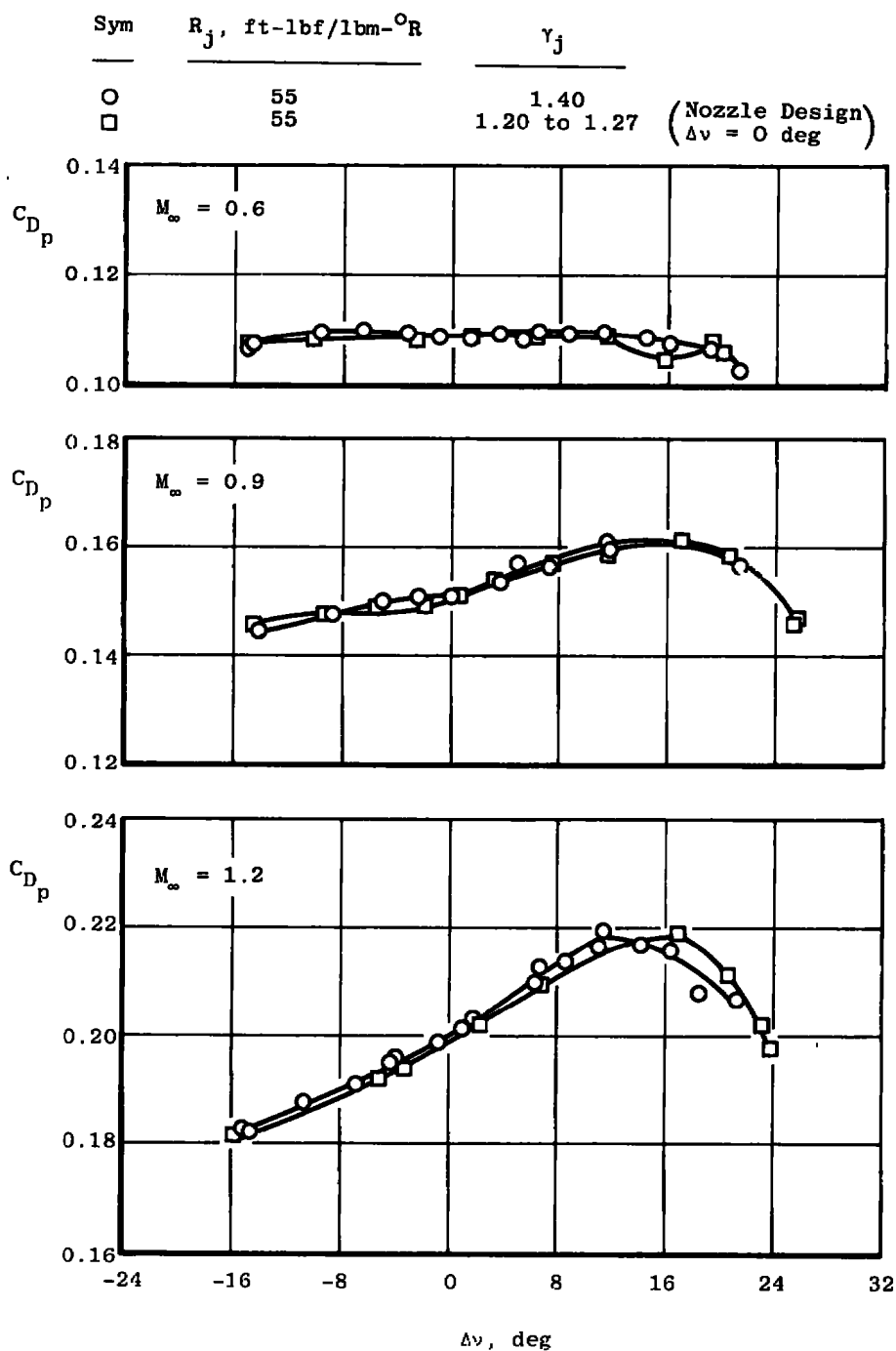


a. Nozzle total pressure ratio

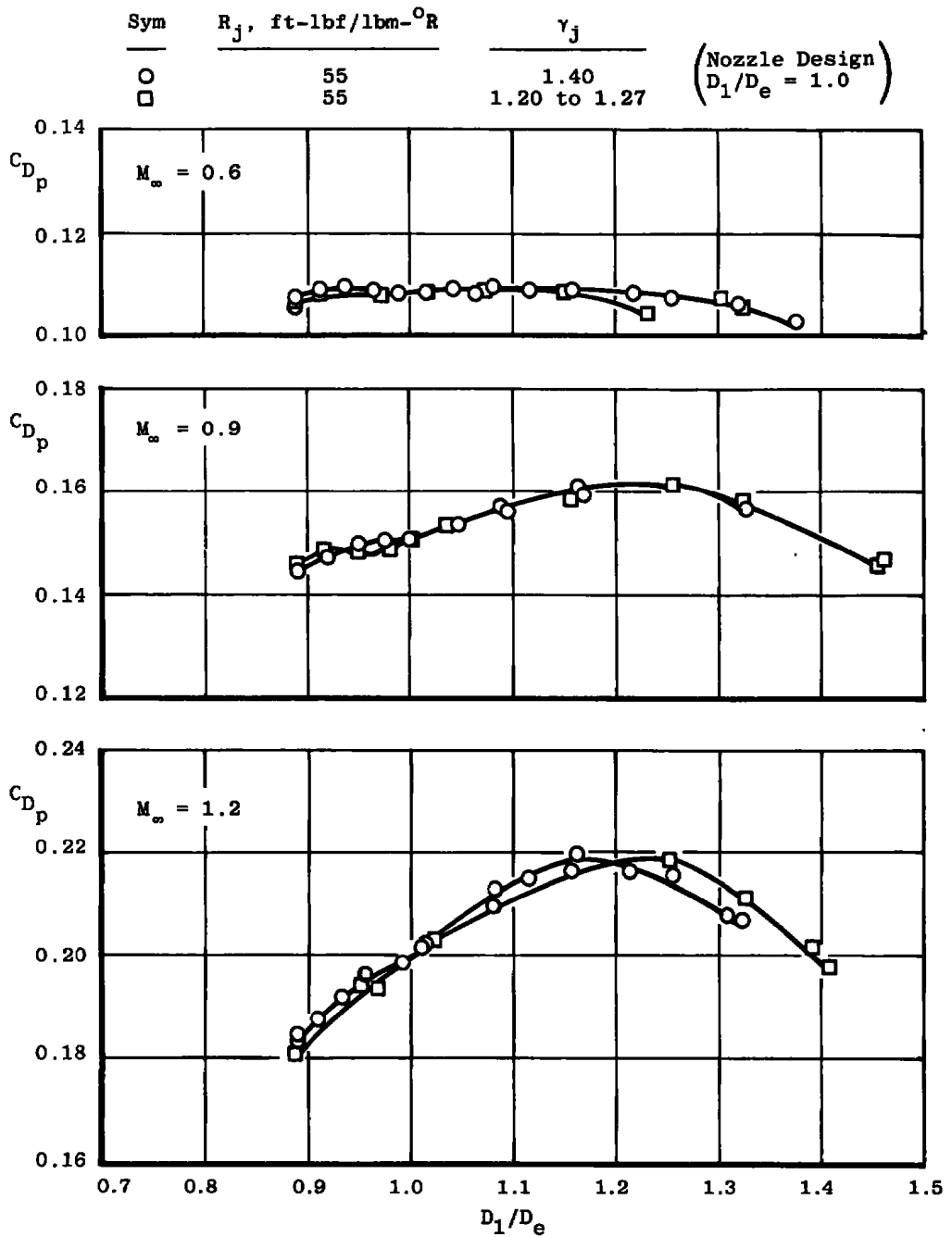
Figure 15. Comparison of inviscid jet plume shape parameters in correlating jet specific heat ratio effects on afterbody pressure drag coefficient for the 25-deg boattail, $A_e/A^* = 1.271$, $T_{tj} = 630^\circ\text{R}$.



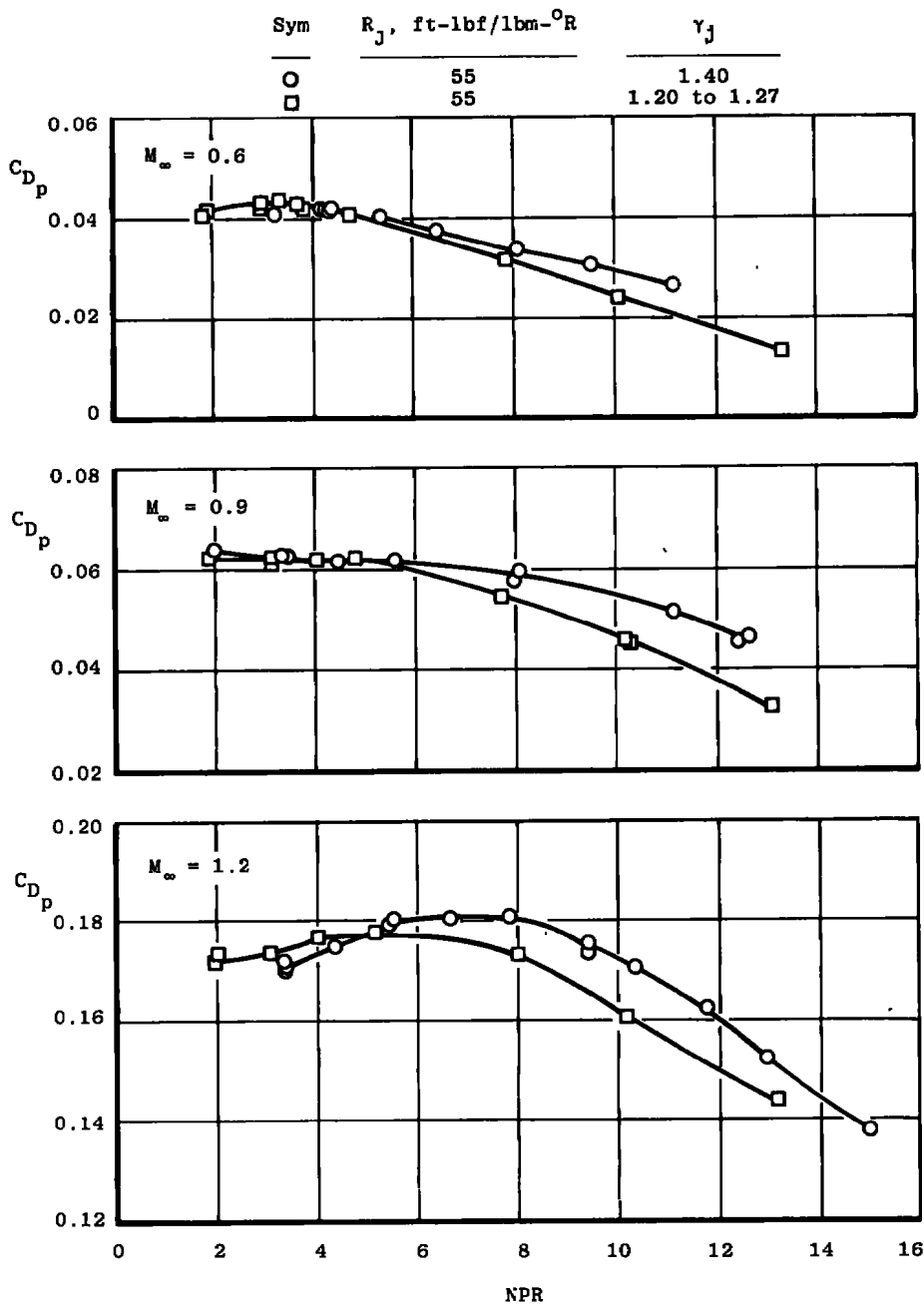
b. Nozzle static pressure ratio
Figure 15. Continued.



c. Incremental Prandtl-Meyer angle
Figure 15. Continued.

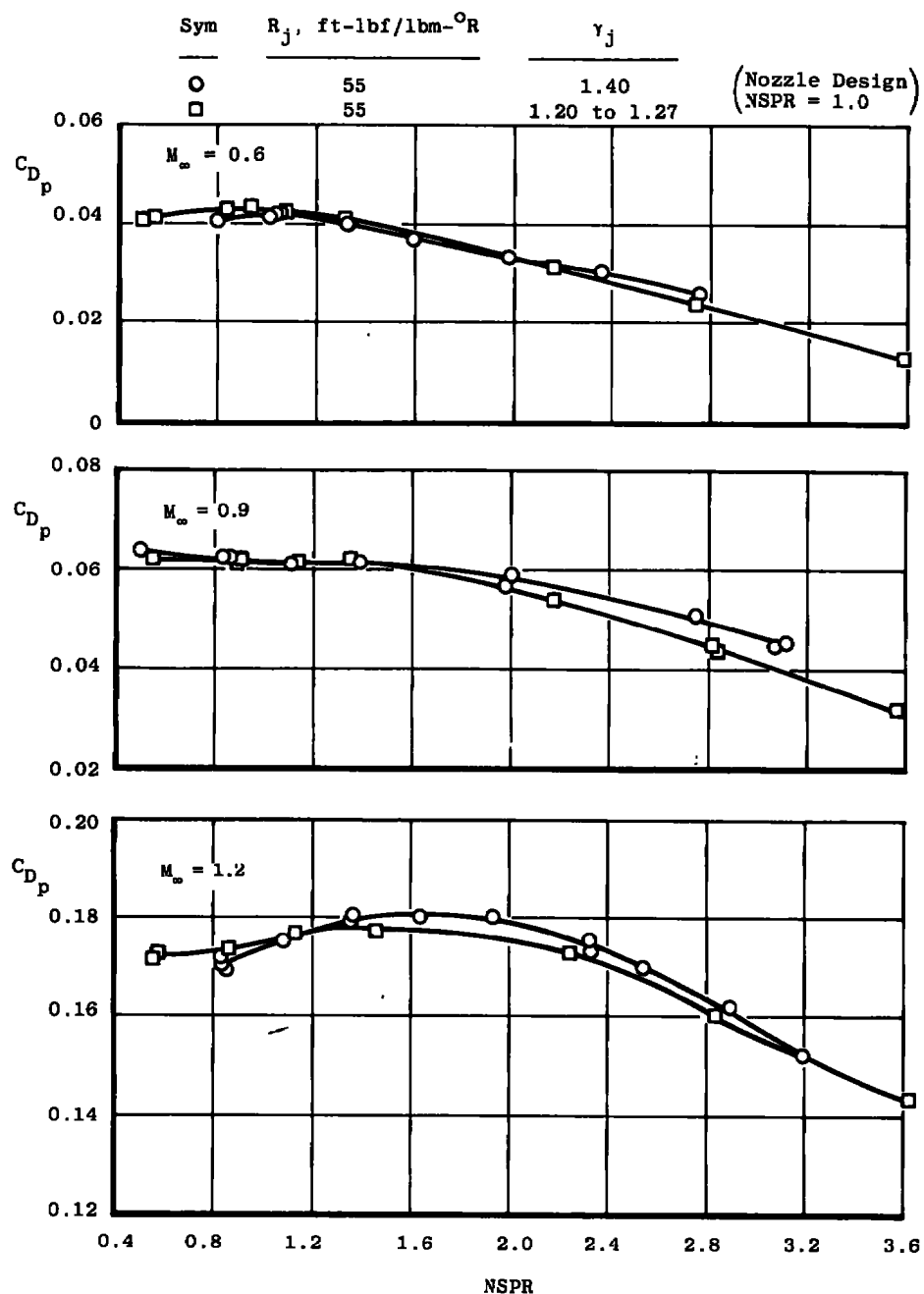


d. Plume-to-nozzle exit diameter ratio
Figure 15. Concluded.

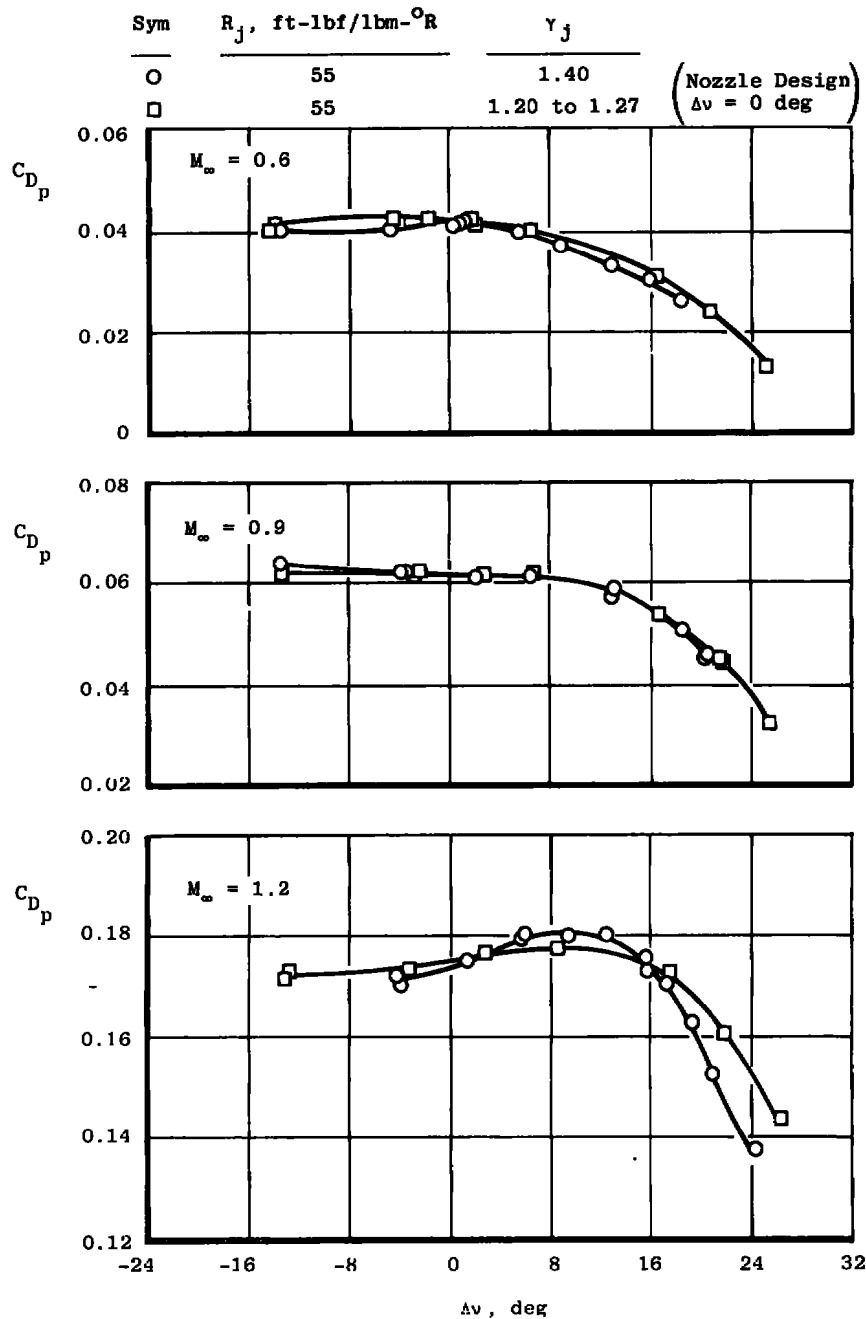


a. Nozzle total pressure ratio

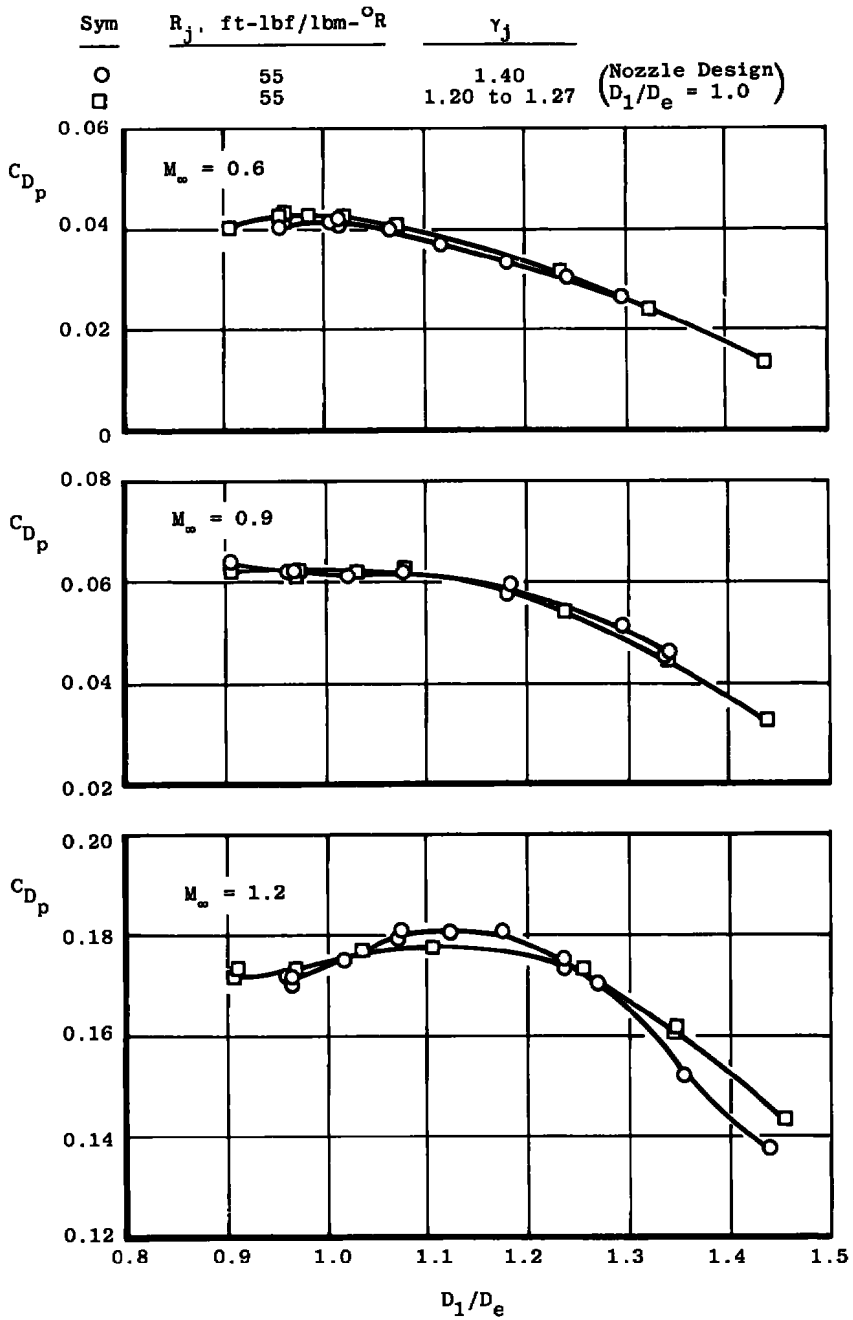
Figure 16. Comparison of inviscid jet plume shape parameters in correlating jet specific heat ratio effects on afterbody pressure drag coefficient for the 15-deg boattail, $A_0/A^* = 1.226$, $T_{tj} = 630^{\circ}$ R.



b. Nozzle static pressure ratio
Figure 16. Continued.



c. Incremental Prandtl-Meyer angle
Figure 16. Continued.



d. Plume-to-nozzle exit diameter ratio
Figure 16. Concluded.

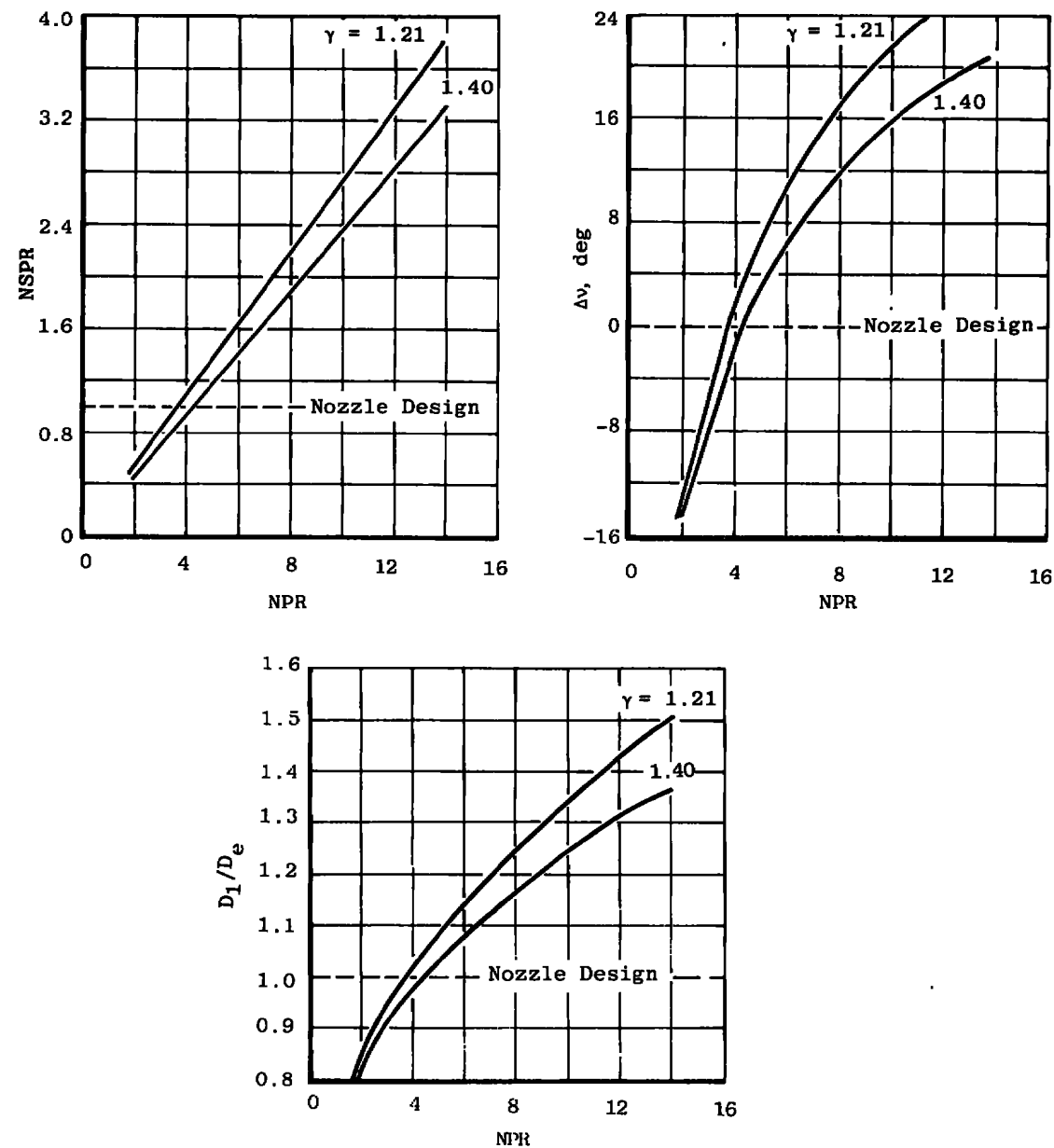
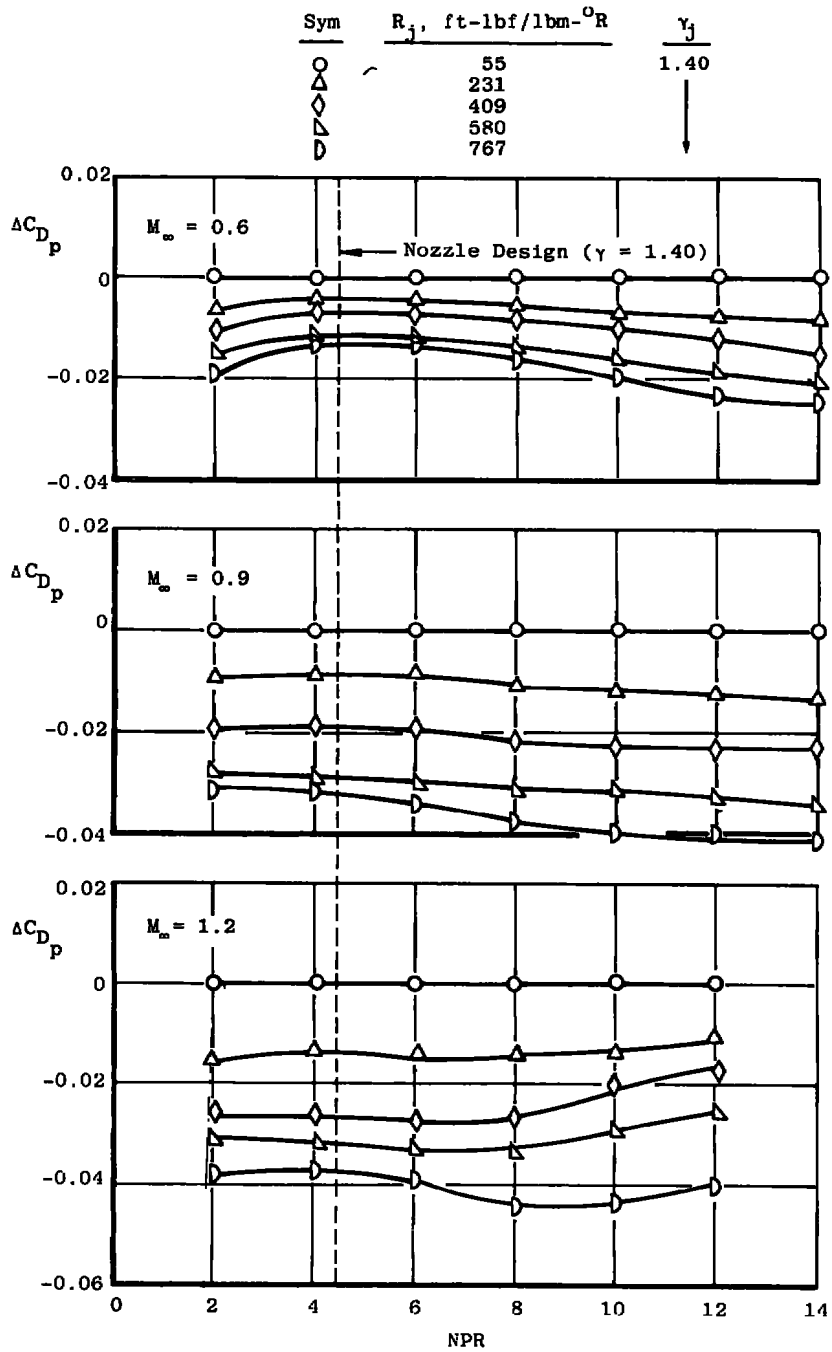
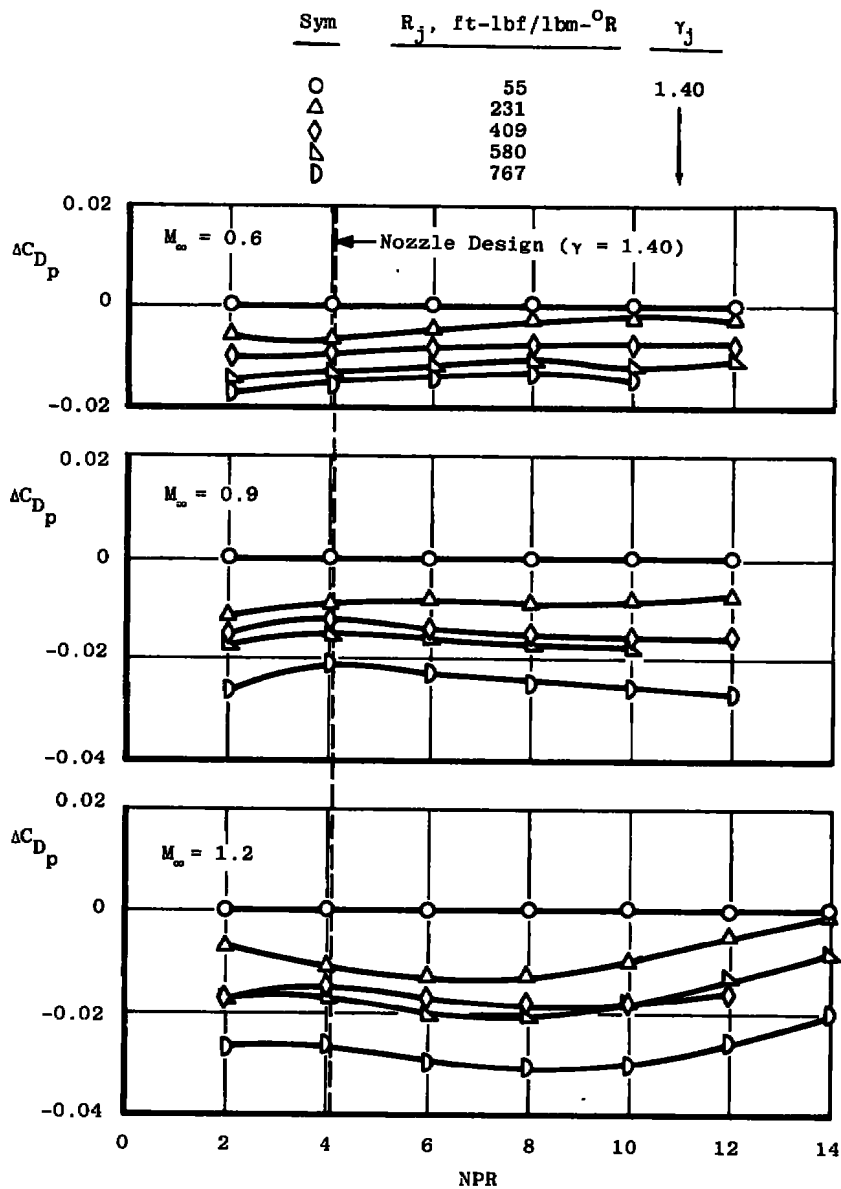


Figure 17. Inviscid jet plume shape parameters as a function of NPR, $A_e/A^* = 1.250$.

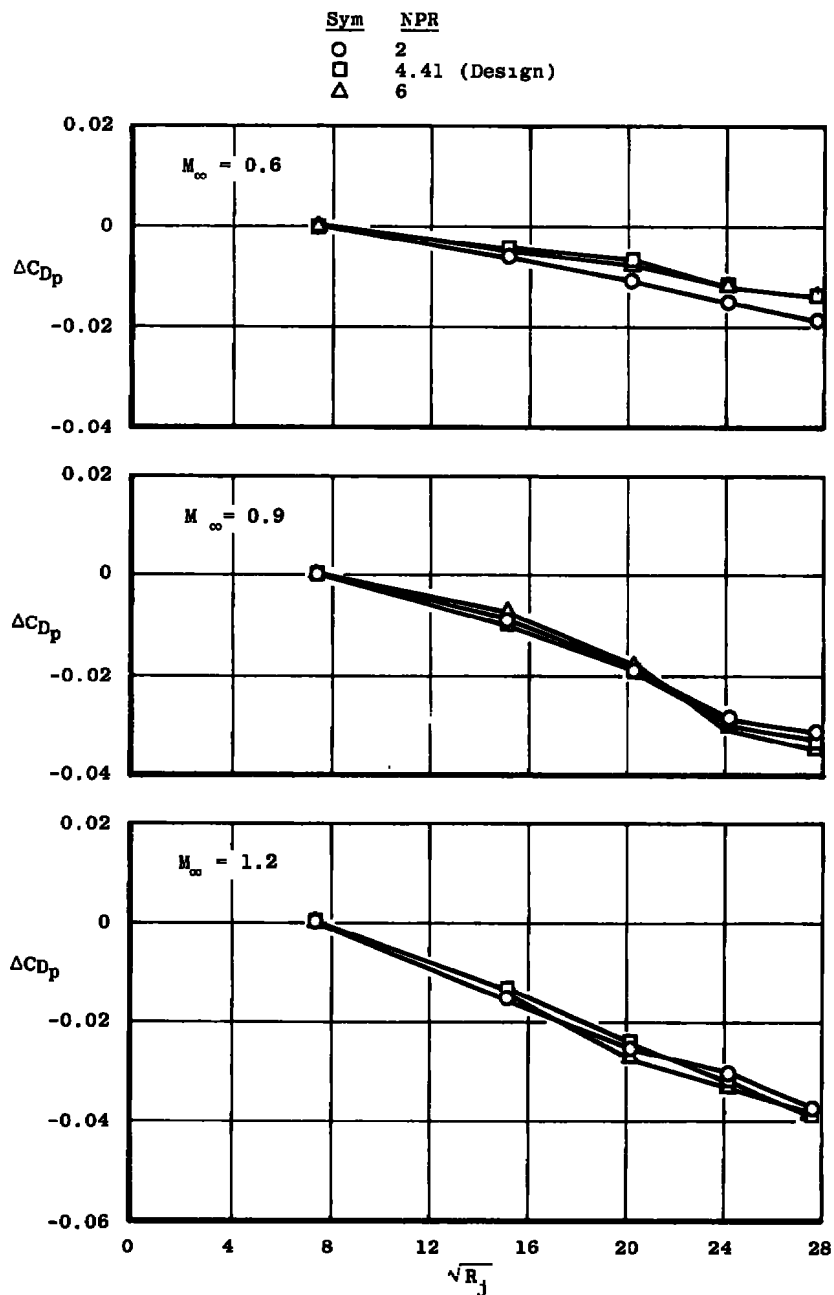


a. 25-deg boattail

Figure 18. Pressure drag coefficient differences between jet exhausts of varying gas constant at design, overexpanded, and underexpanded jet plume shape conditions, $T_{tj} = 630^{\circ}$ R.

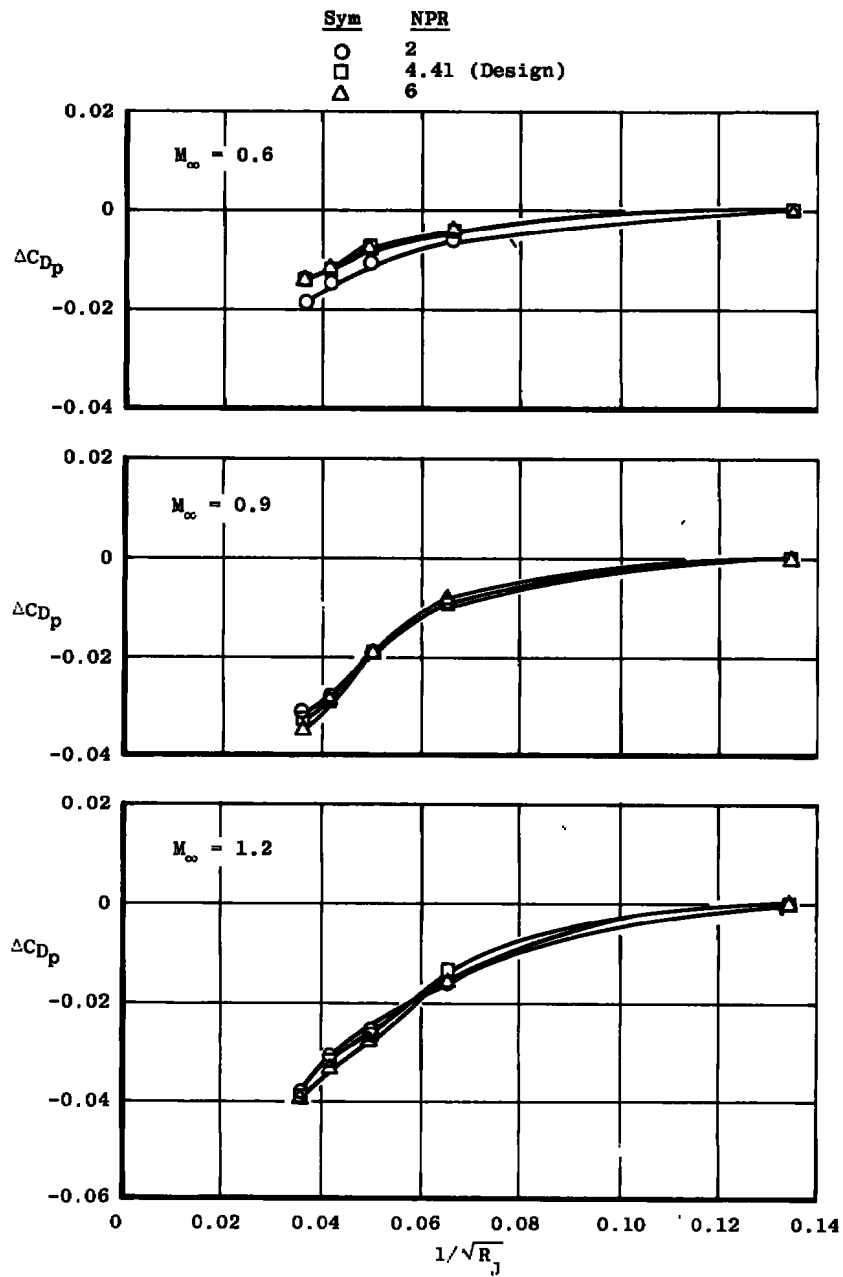


b. 15-deg boattail
Figure 18. Concluded.

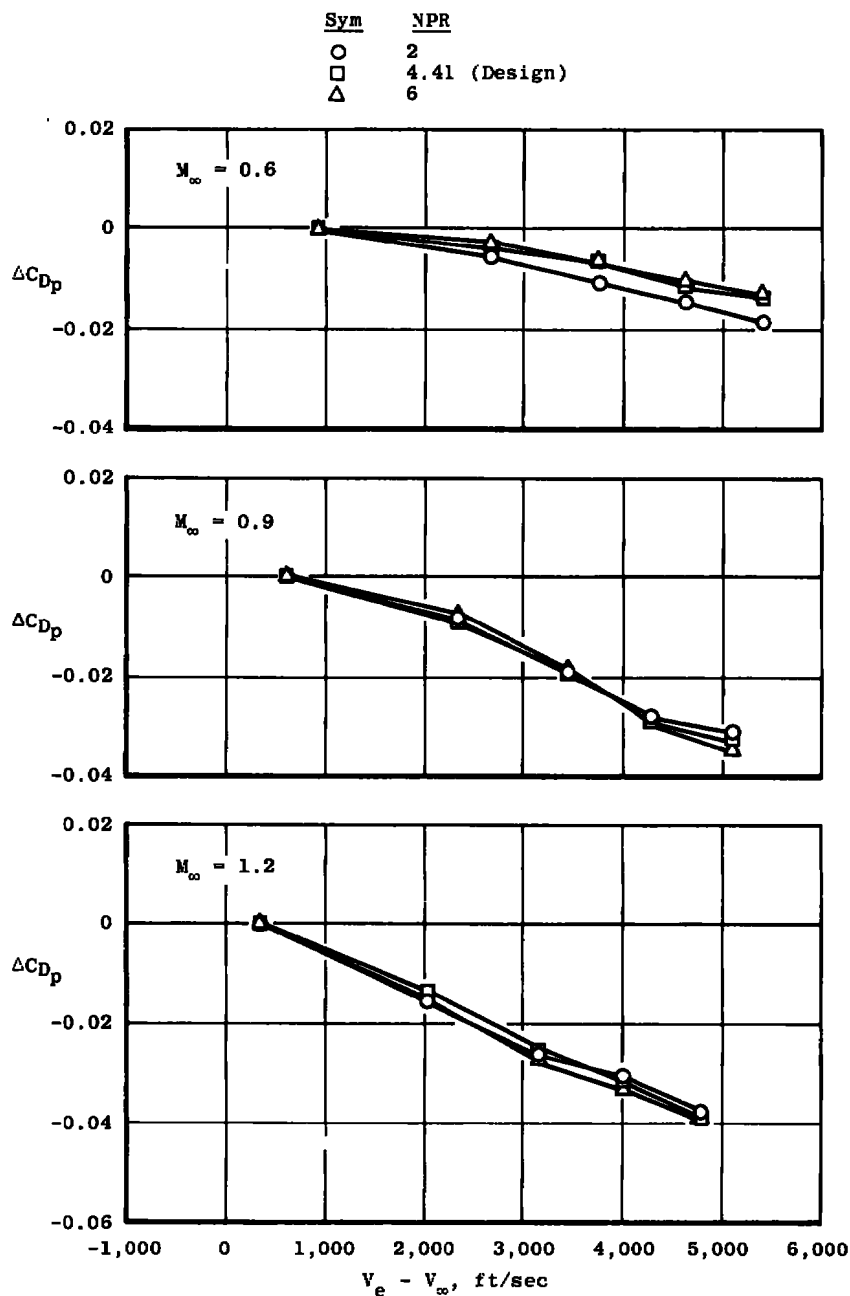


a. Square root of jet gas constant

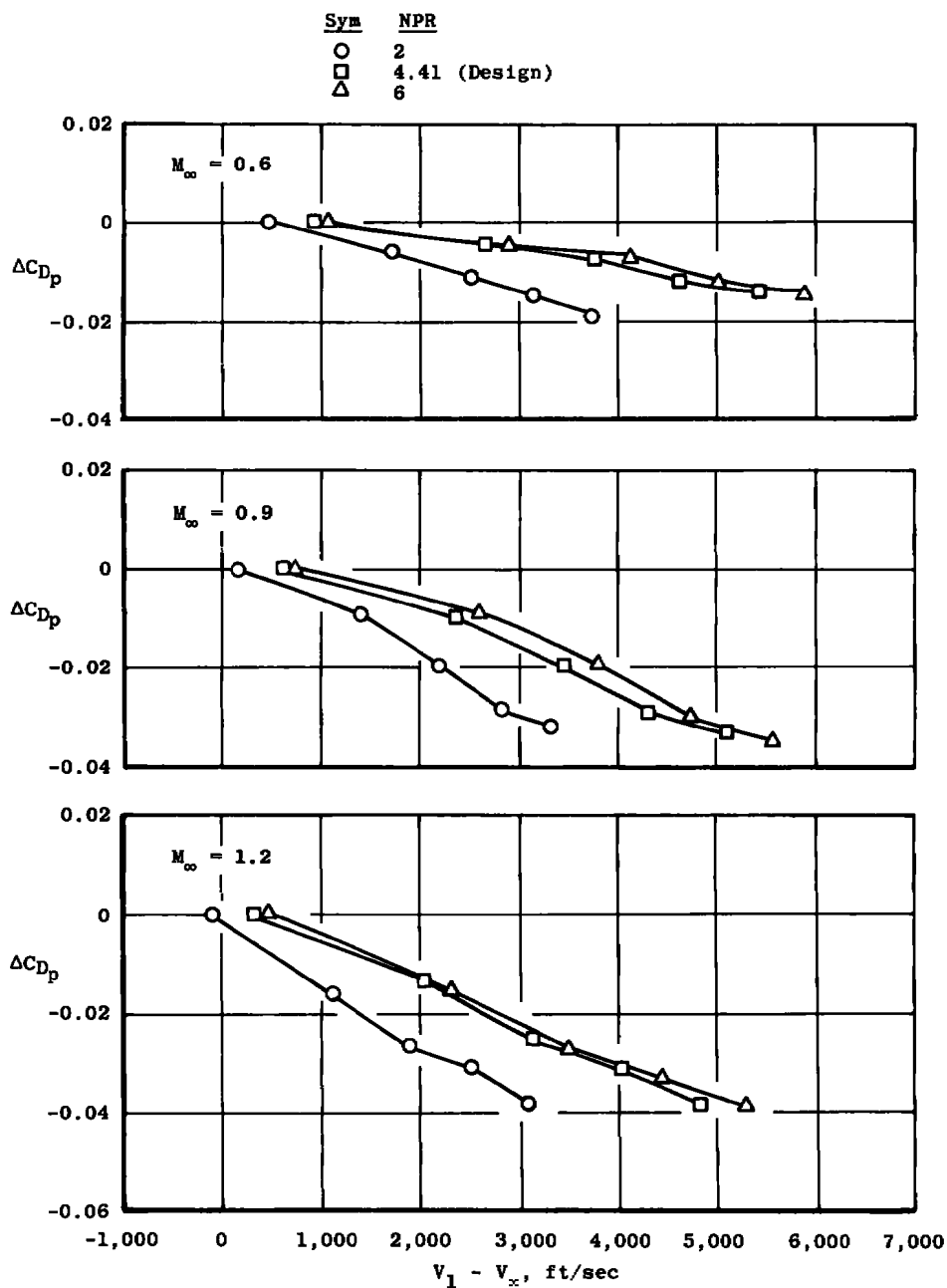
Figure 19. Correlation parameters for jet gas constant effects at design, overexpanded, and underexpanded jet plume shape conditions for the 25-deg boattail, $A_e/A^* = 1.271$, $T_{tj} = 630^\circ\text{R}$.



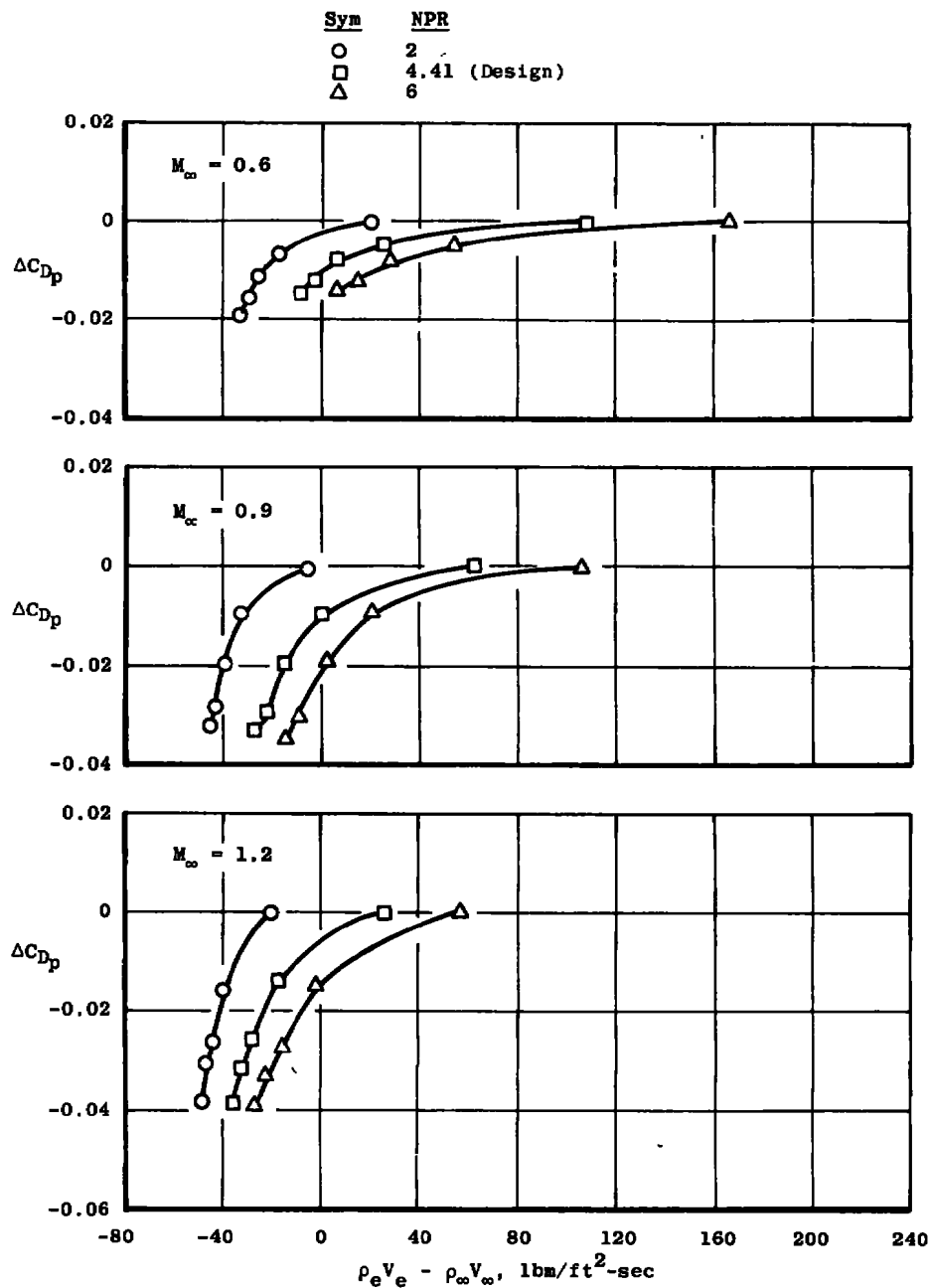
b. Reciprocal of square root of jet exhaust gas constant
Figure 19. Continued.



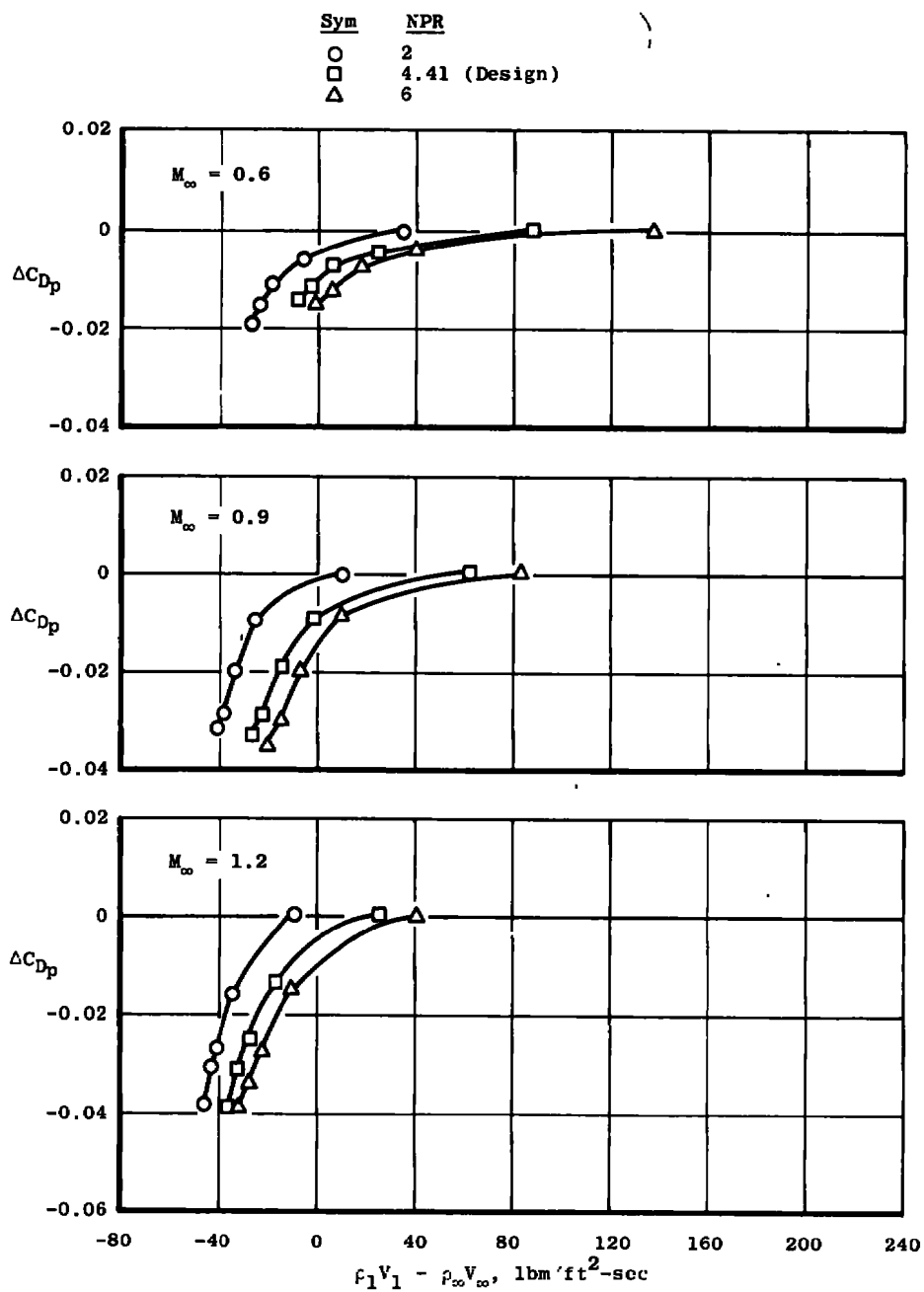
c. Difference in velocity between jet and free-stream at nozzle exit
Figure 19. Continued.



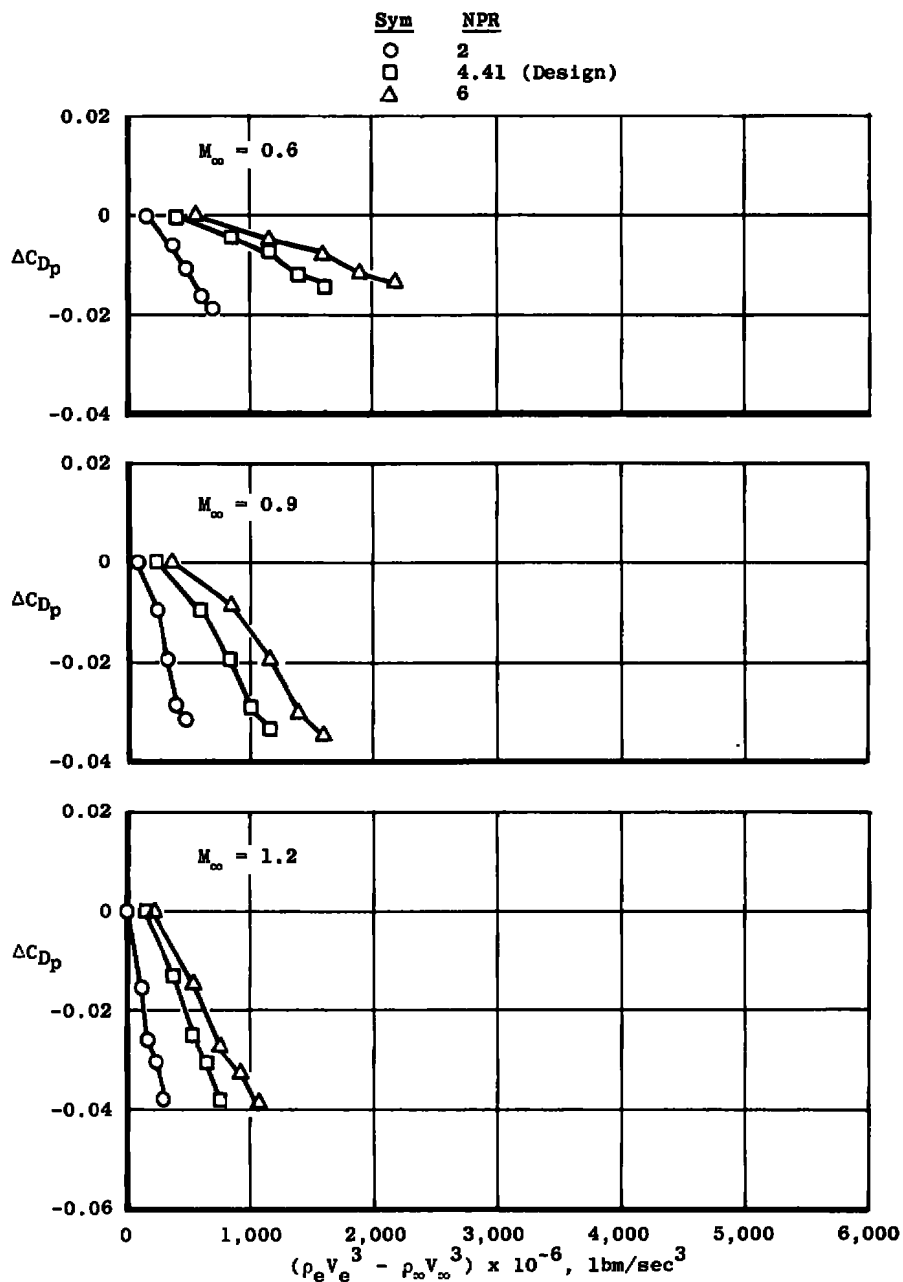
d. Difference in velocity between jet and free-stream at plume boundary
Figure 19. Continued.



e. Difference in mass flux between jet and free-stream at nozzle exit
Figure 19. Continued.



f. Difference in mass flux between jet and free-stream at plume boundary
Figure 19. Continued.



g. Difference in kinetic energy flux between jet and free-stream at nozzle exit

Figure 19. Continued.

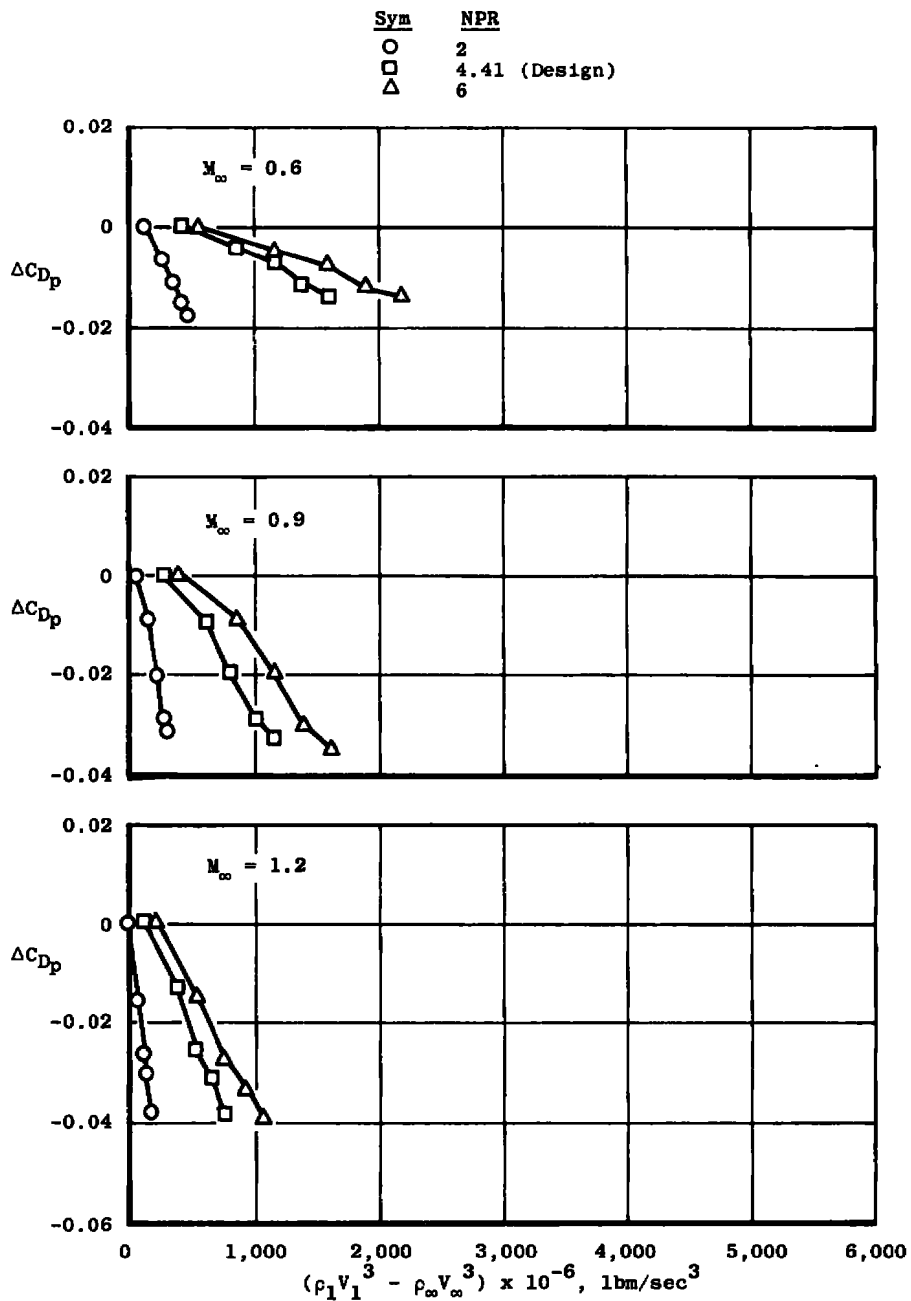
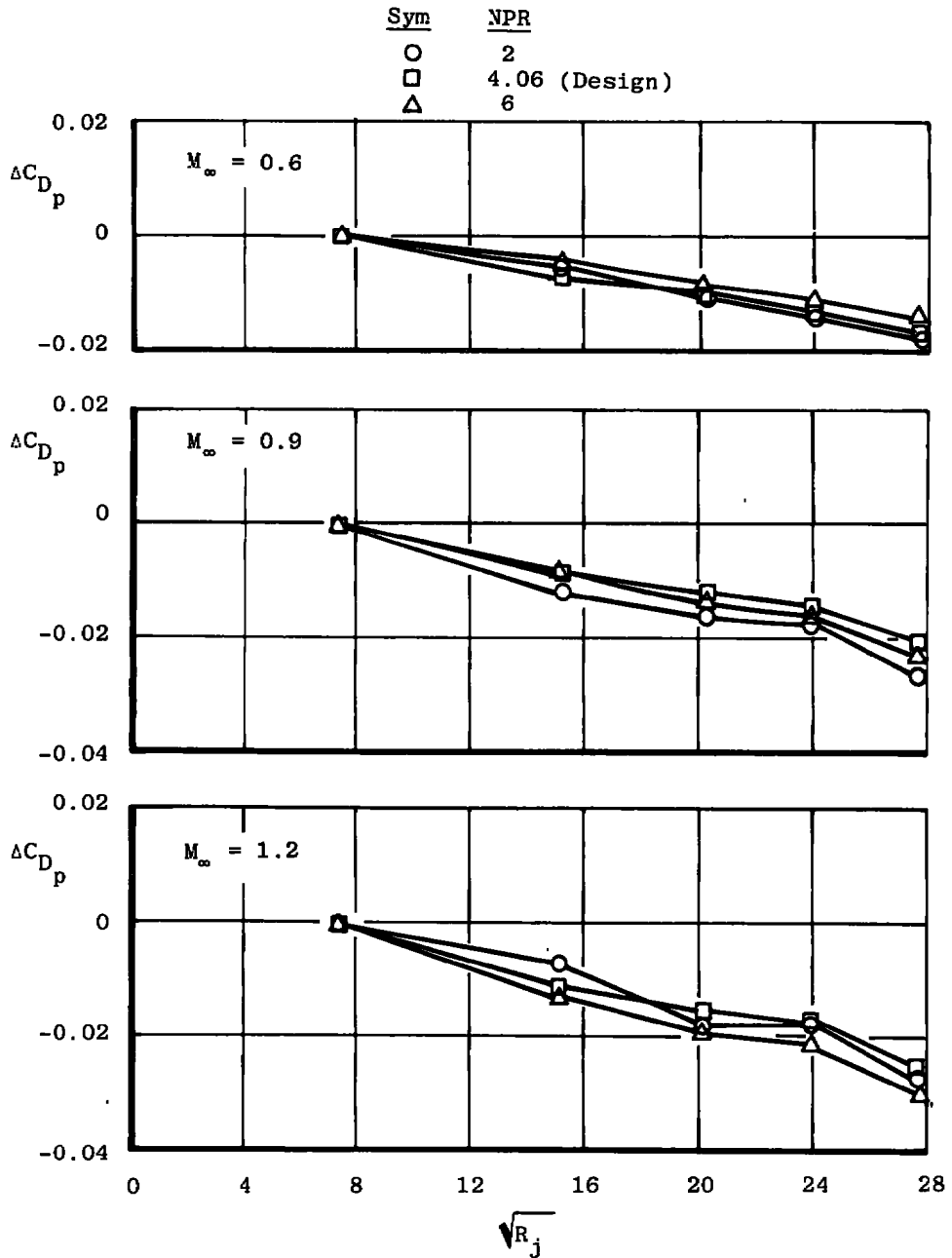
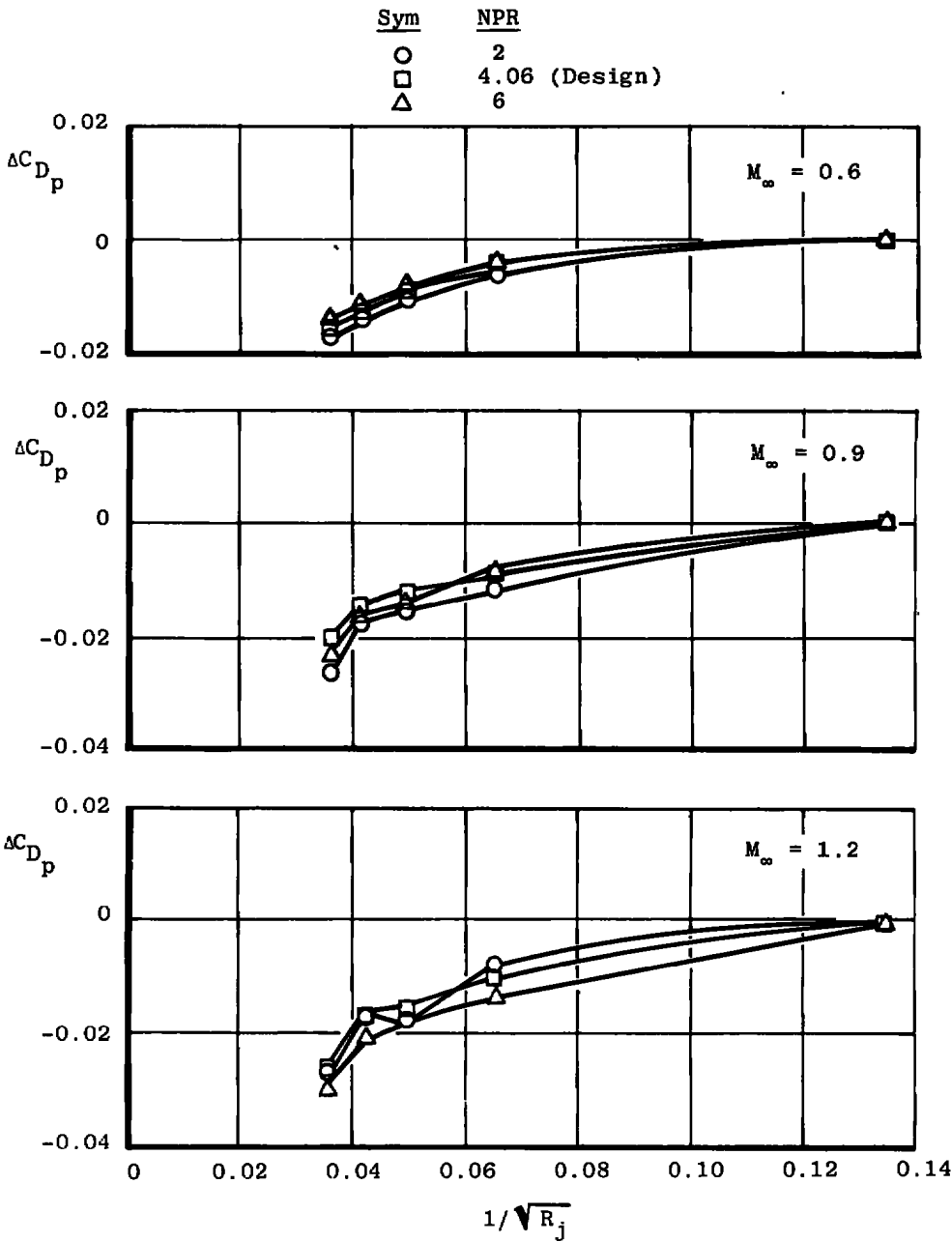


Figure 19. Concluded.

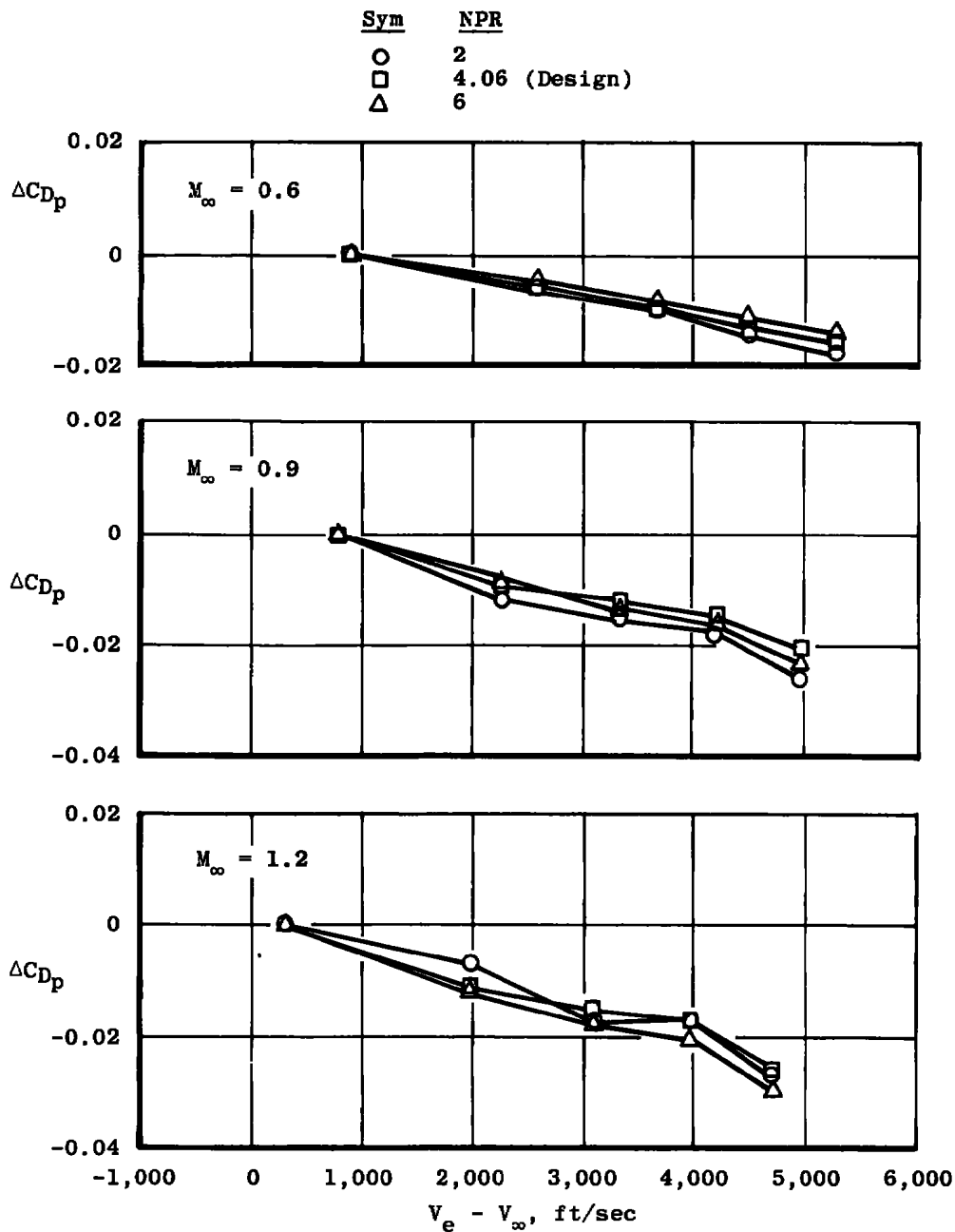


a. Square root of jet gas constant

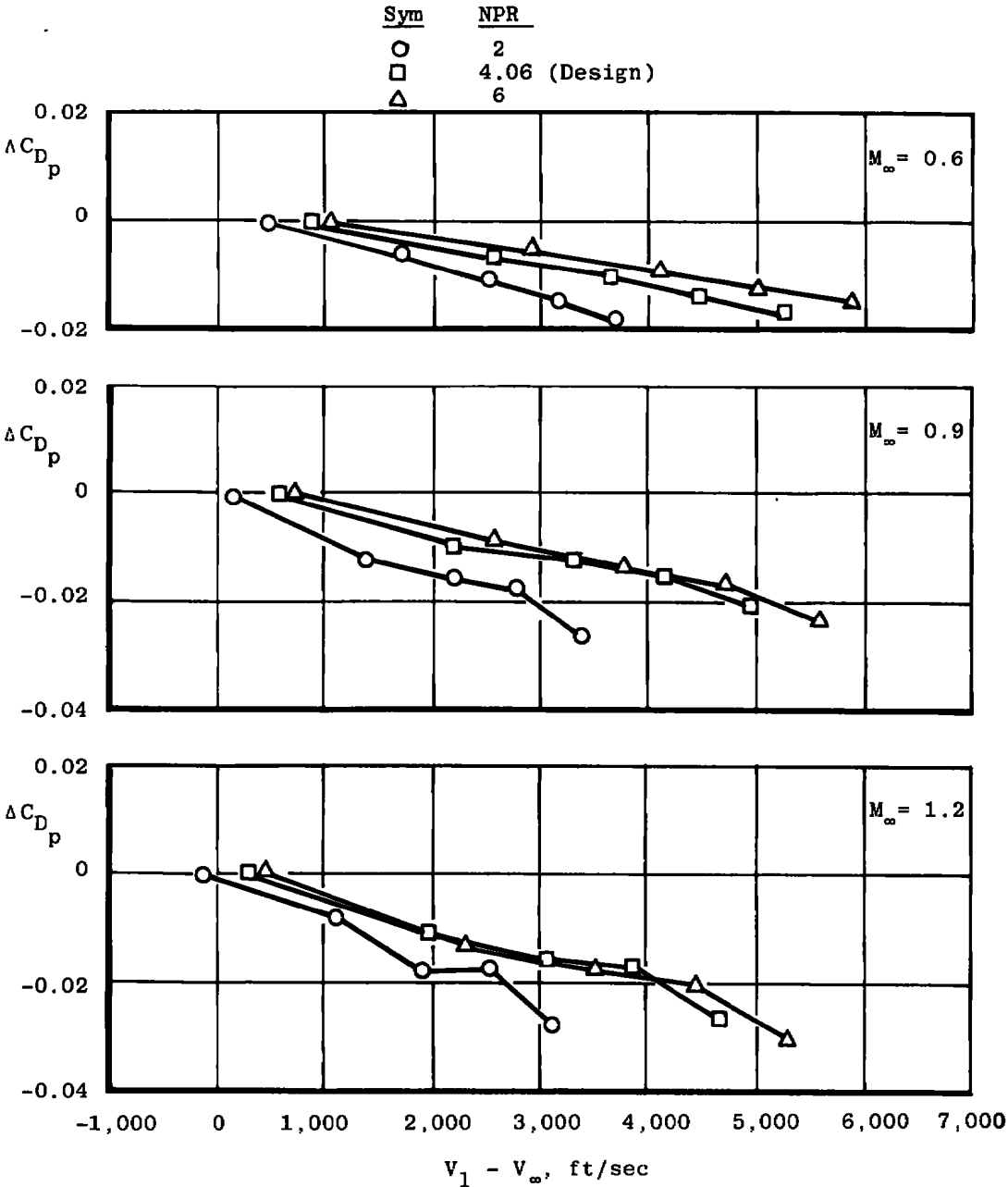
Figure 20. Correlation parameters for jet gas constant effects at design, overexpanded, and underexpanded jet plume conditions for the 15-deg boattail, $A_e/A^* = 1.226$, $T_{tj} = 630^\circ R$.



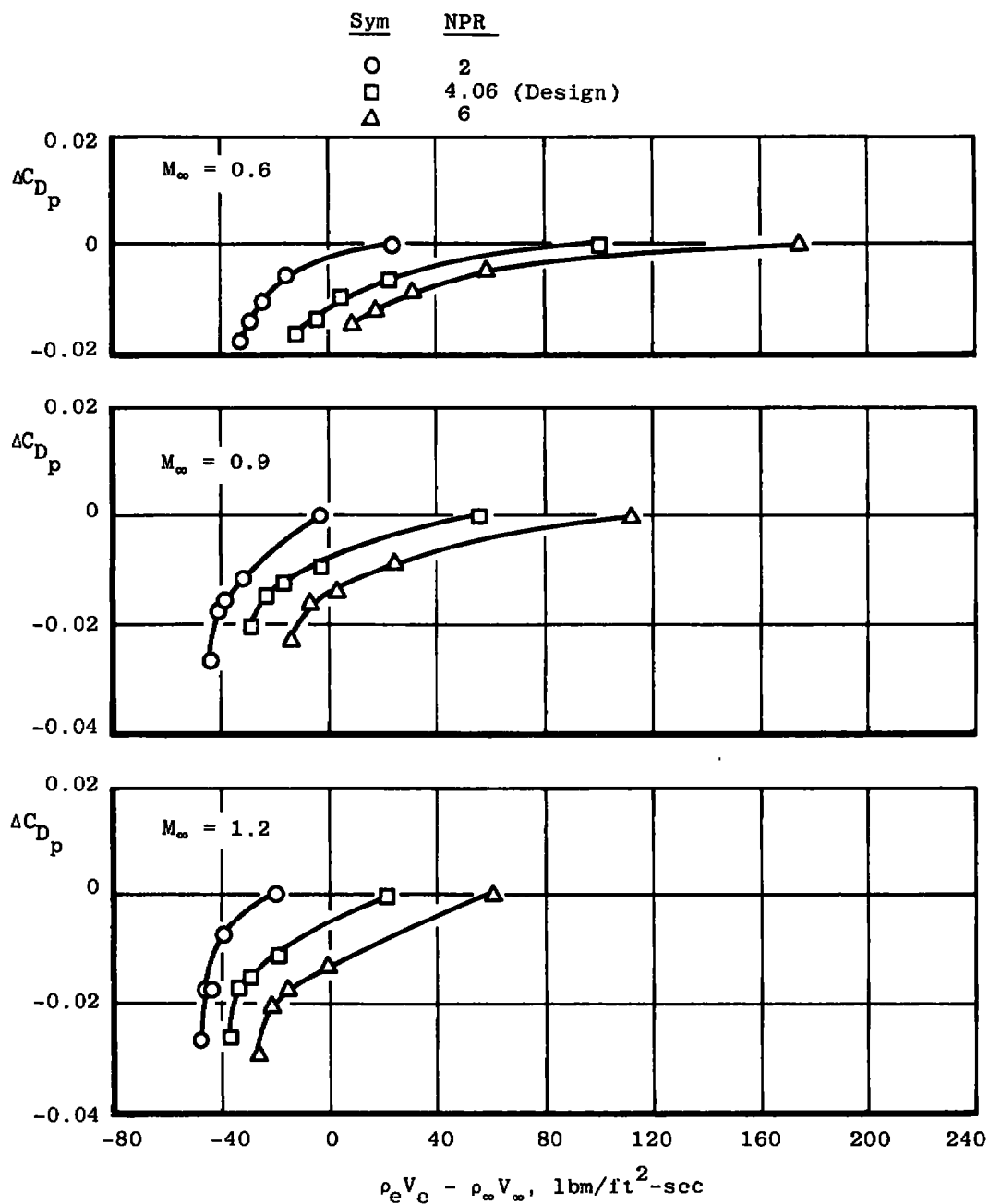
b. Reciprocal of square root of jet exhaust gas constant
Figure 20. Continued.



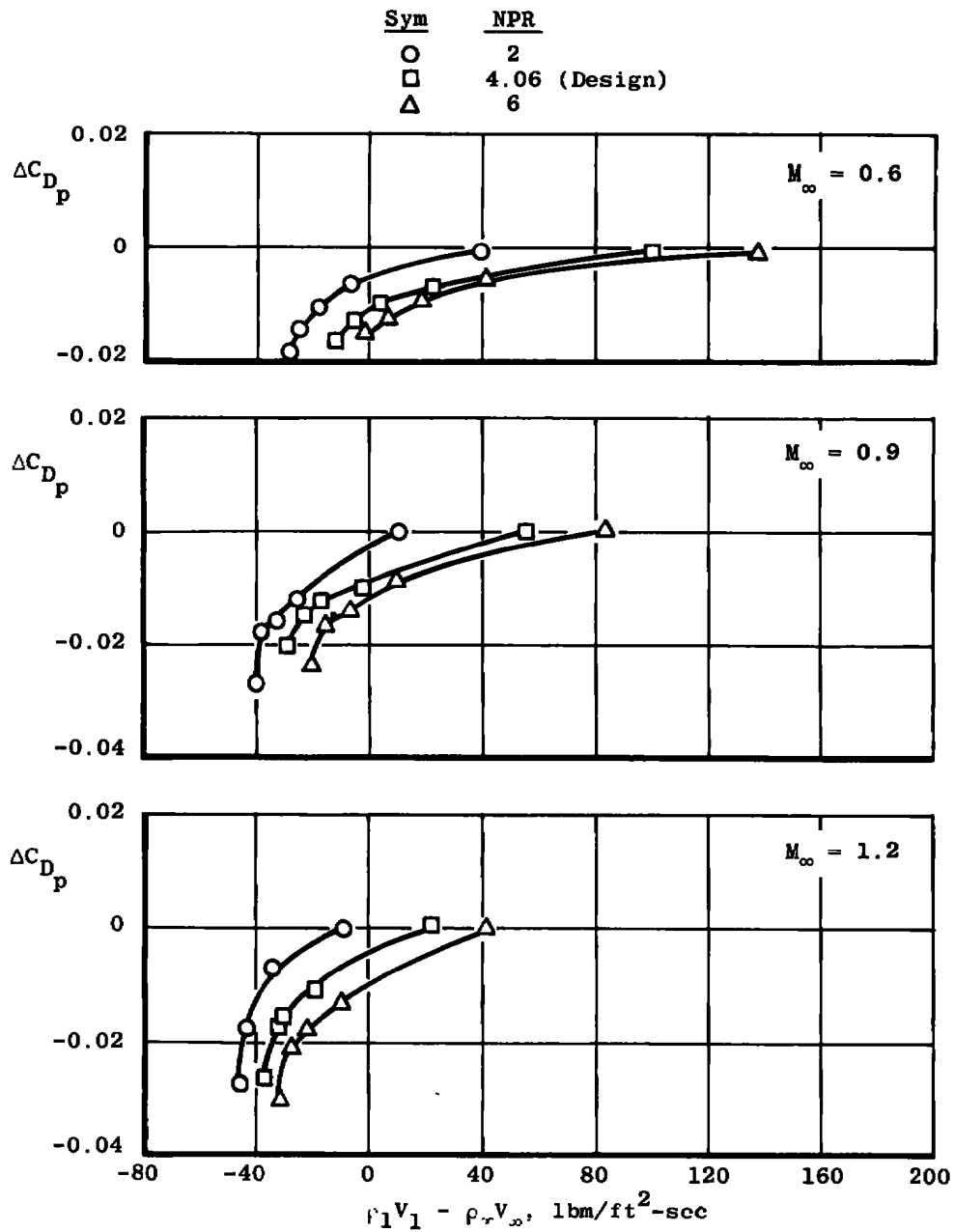
c. Difference in velocity between jet and free-stream at nozzle exit
Figure 20. Continued.



d. Difference in velocity between jet and free-stream at plume boundary
Figure 20. Continued.

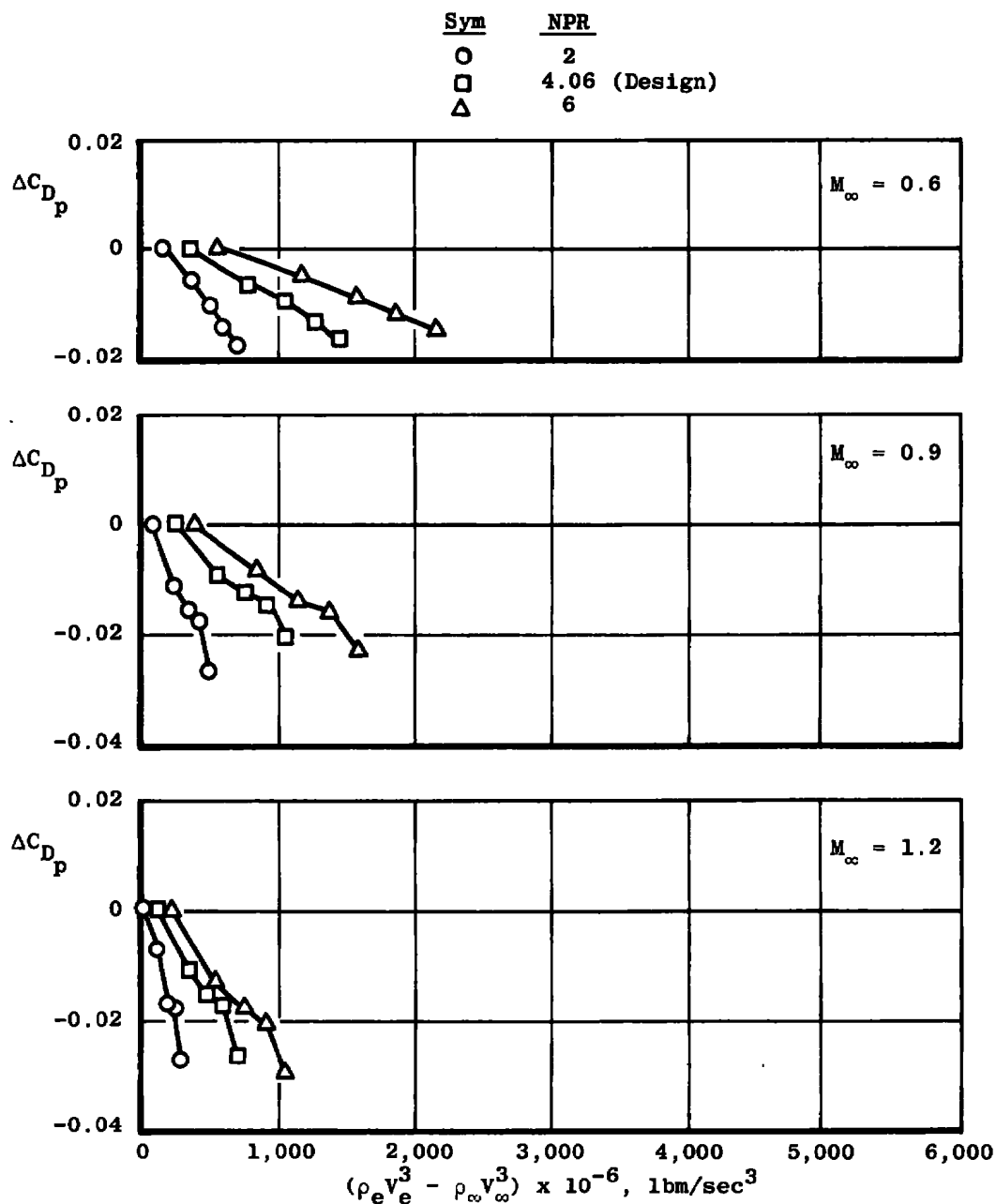


e. Difference in mass flux between jet and free-stream at nozzle exit
Figure 20. Continued.



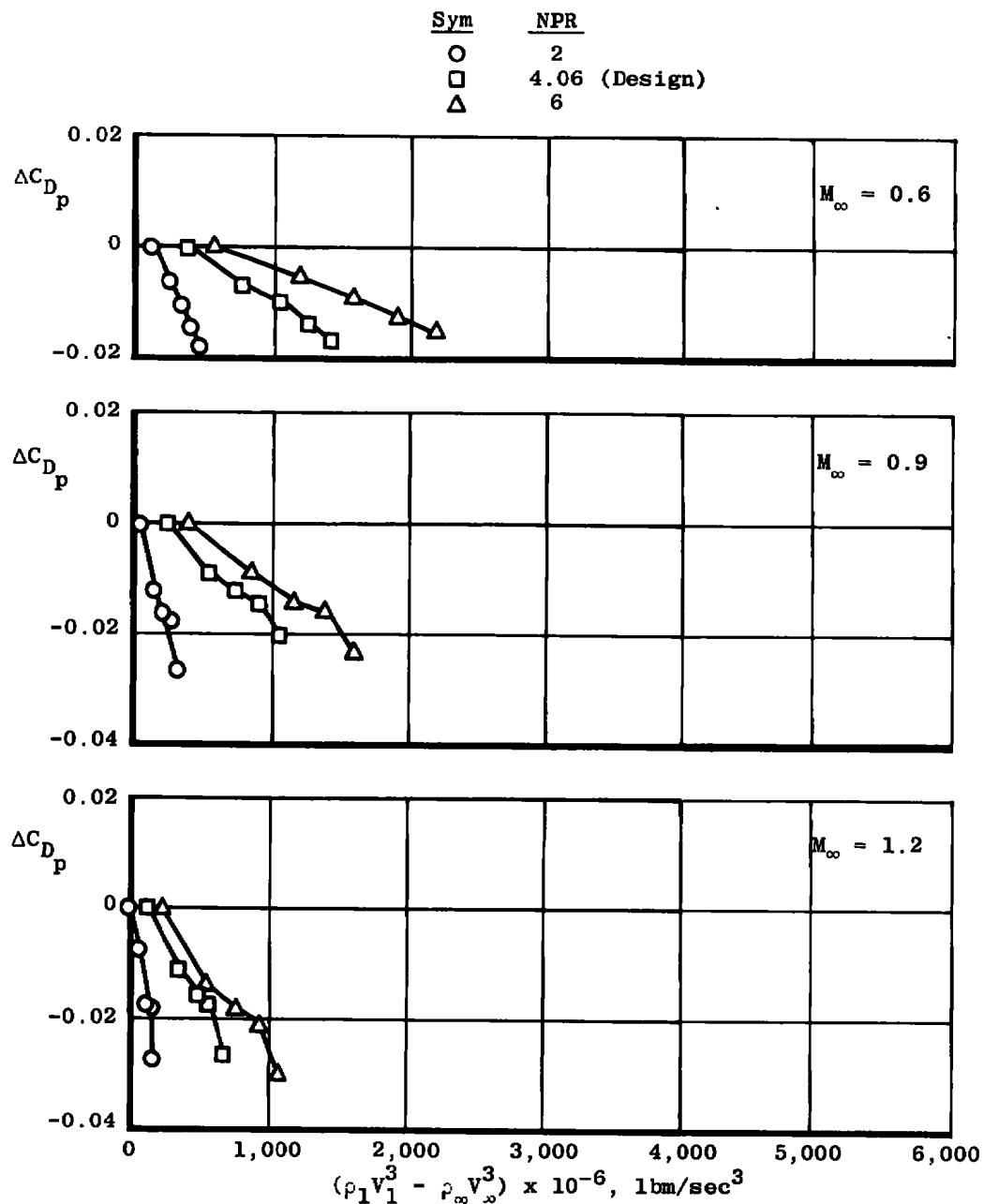
f. Difference in mass flux between jet and free-stream at plume boundary

Figure 20. Continued.



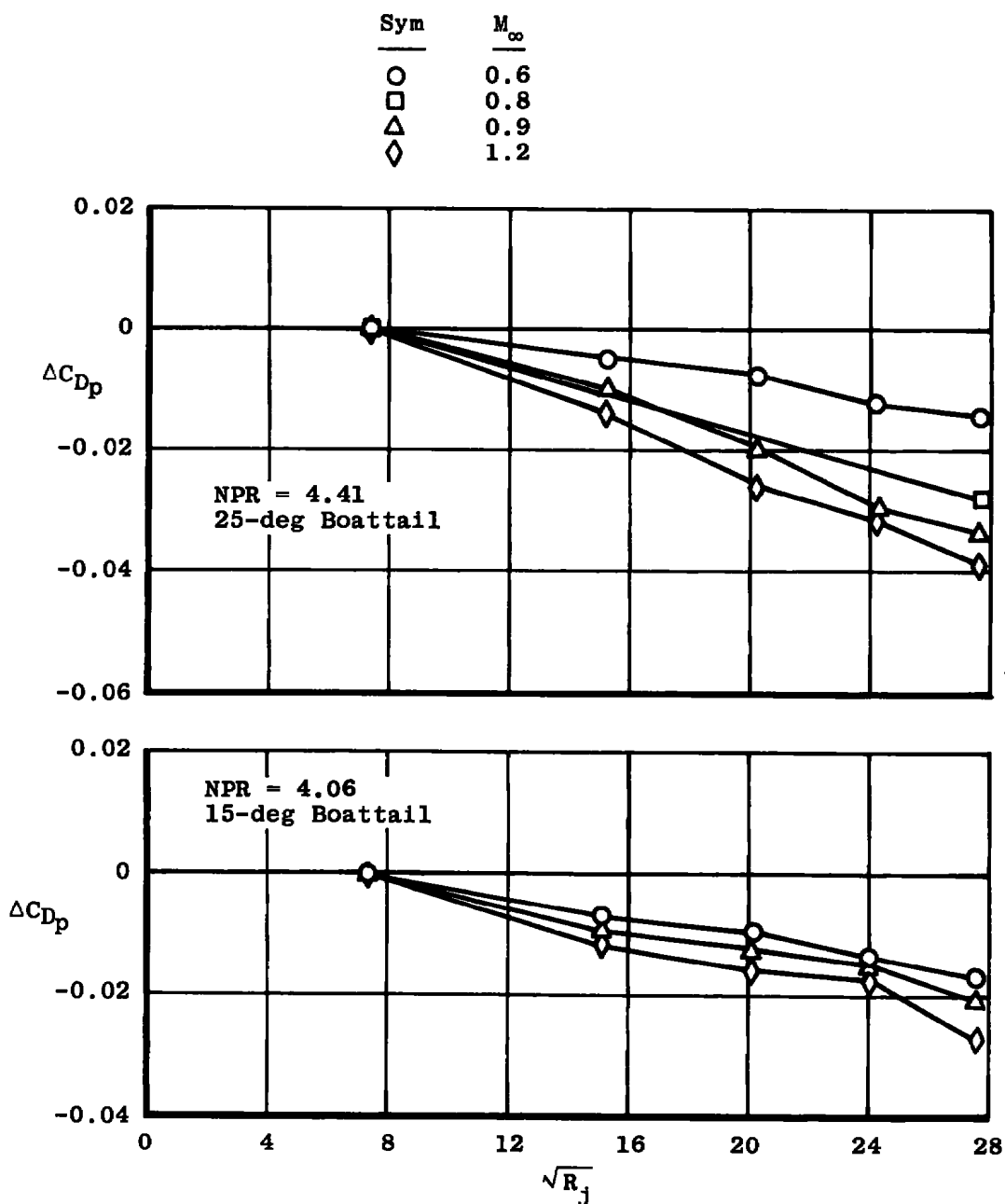
g. Difference in kinetic energy flux between jet and free-stream at nozzle exit

Figure 20. Continued.

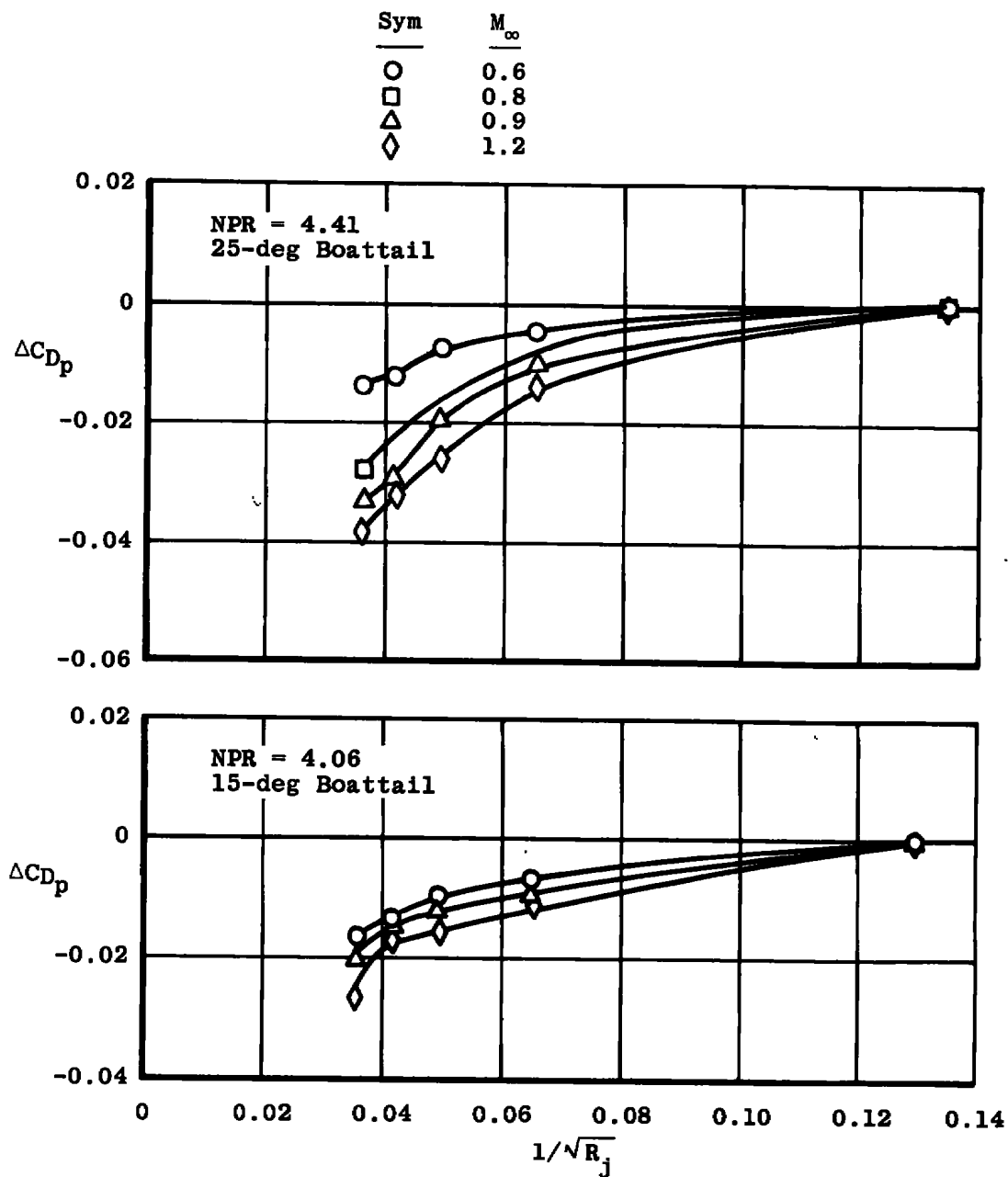


h. Difference in kinetic energy flux between jet and free-stream
at plume boundary

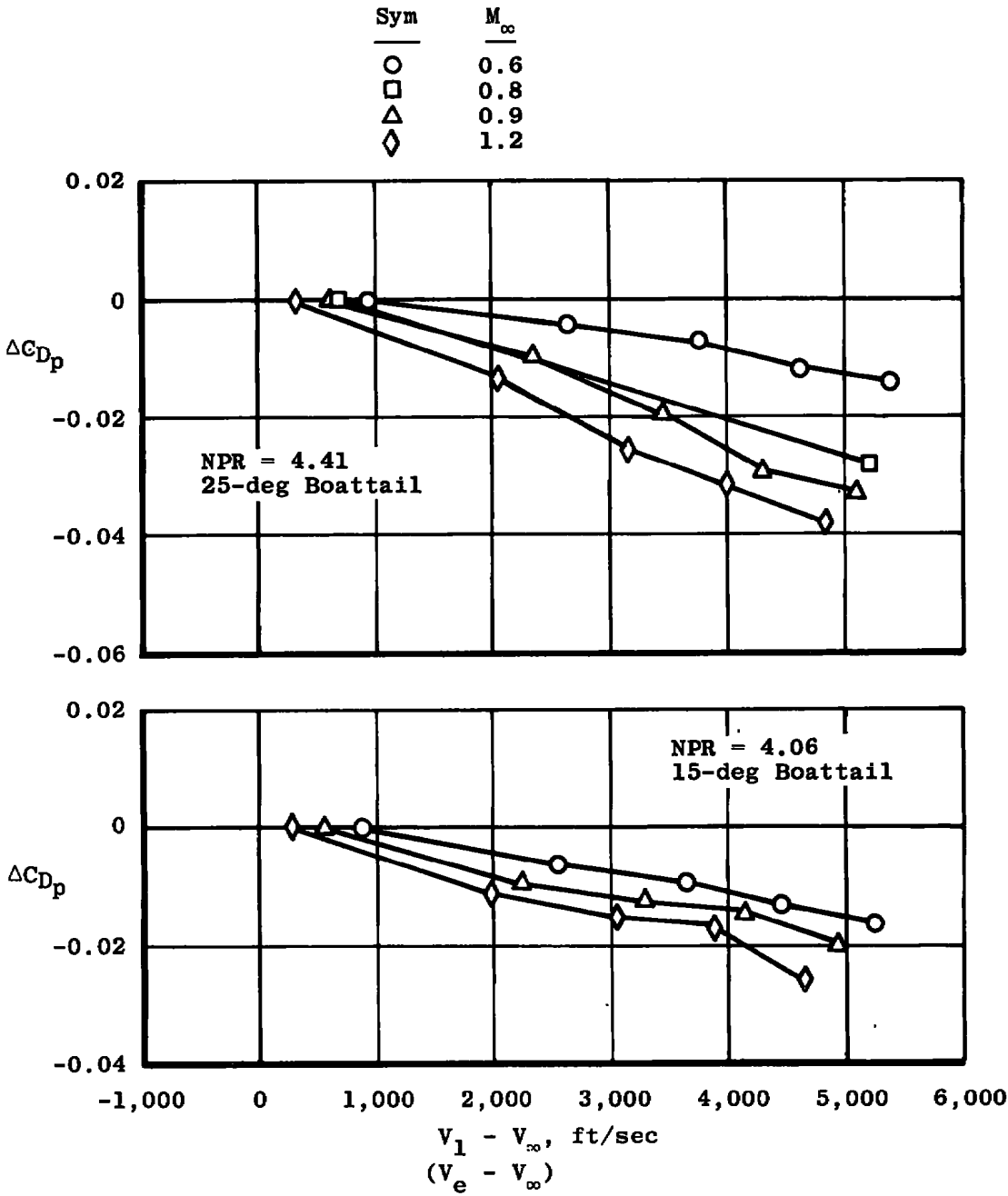
Figure 20. Concluded.



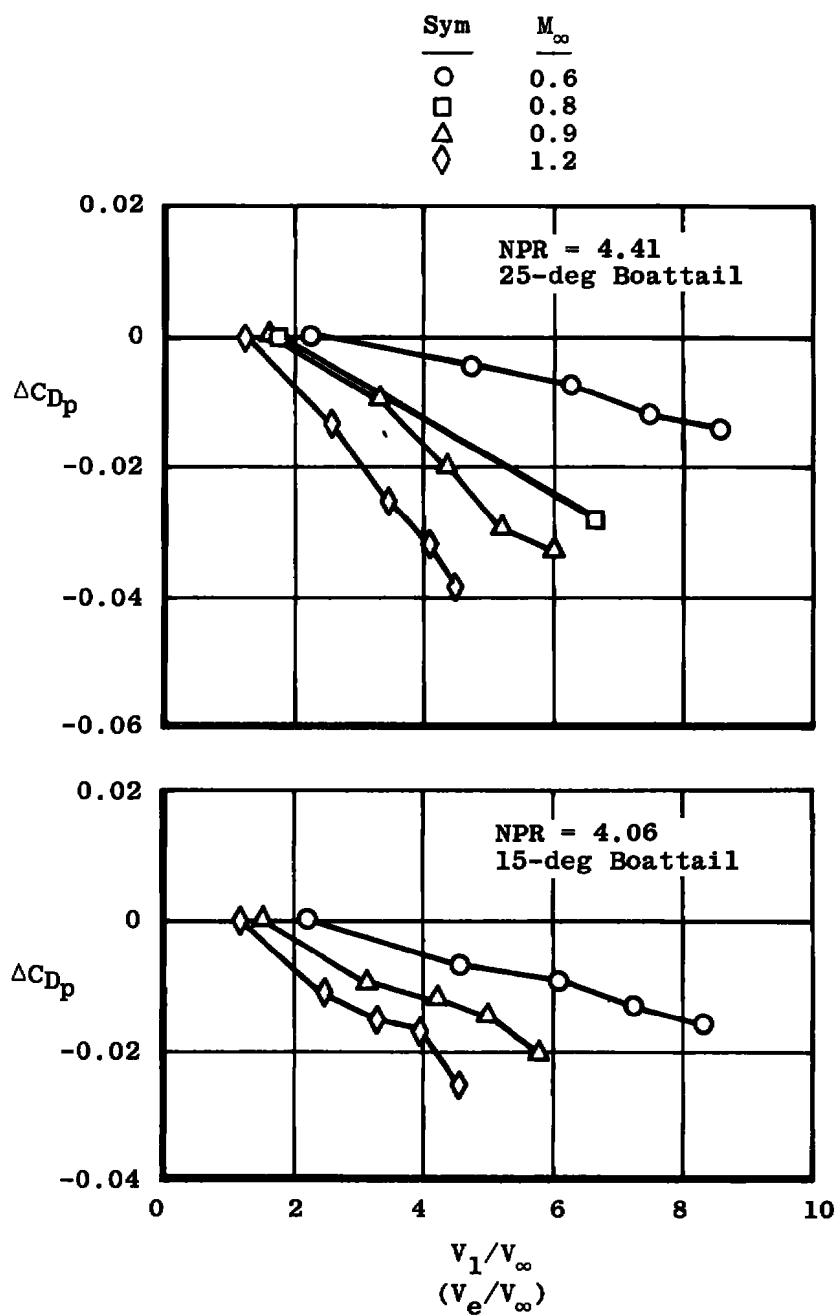
a. Square root of jet gas constant
 Figure 21. Correlation parameters for jet gas constant effects and Mach number effects at nozzle design conditions, $T_{tj} = 630^\circ\text{R}$.



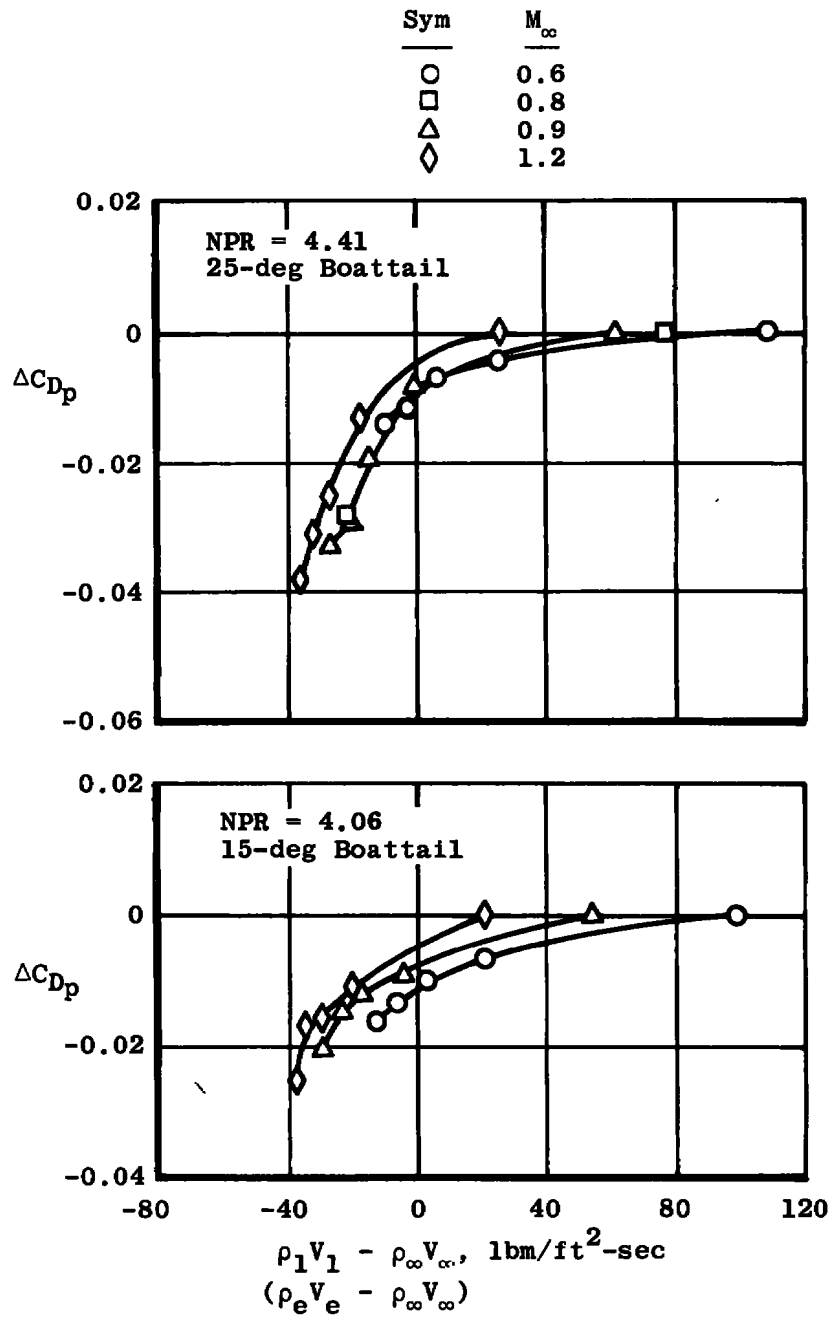
b. Reciprocal of square root of jet gas constant
Figure 21. Continued.



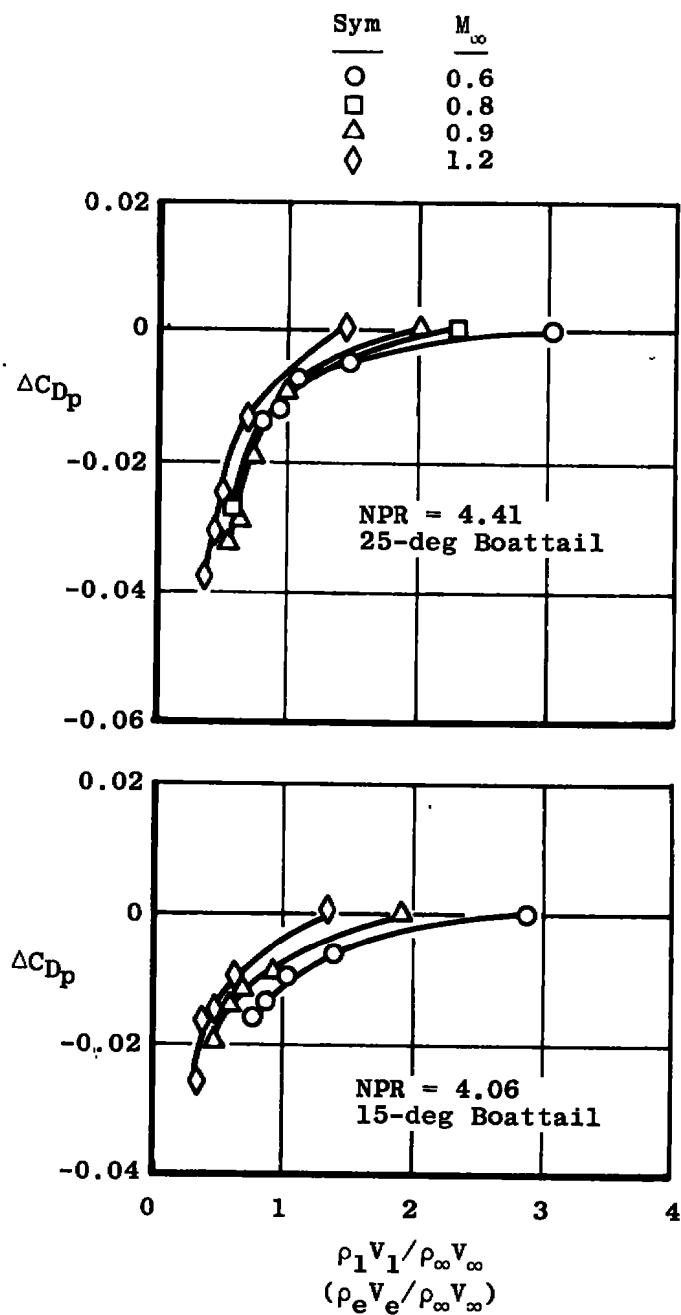
c. Difference in jet and free-stream velocities
Figure 21. Continued.



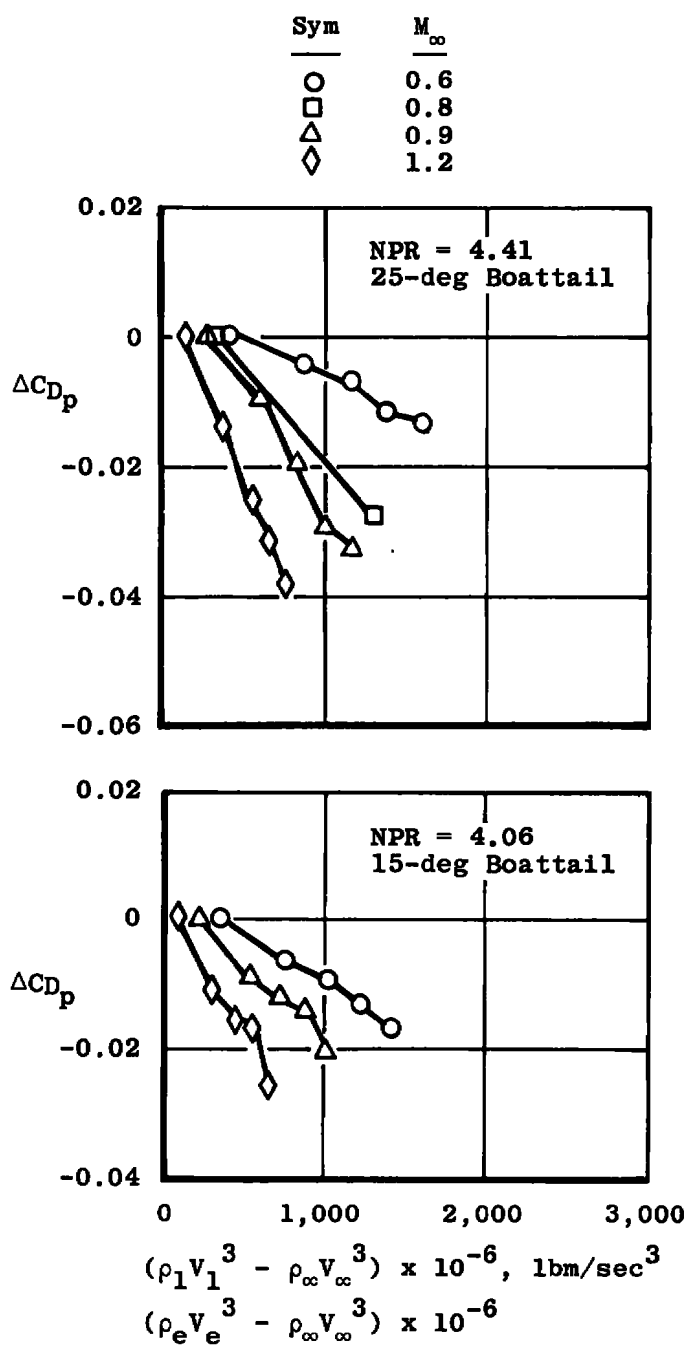
d. Ratio of jet and free-stream velocities
Figure 21. Continued.



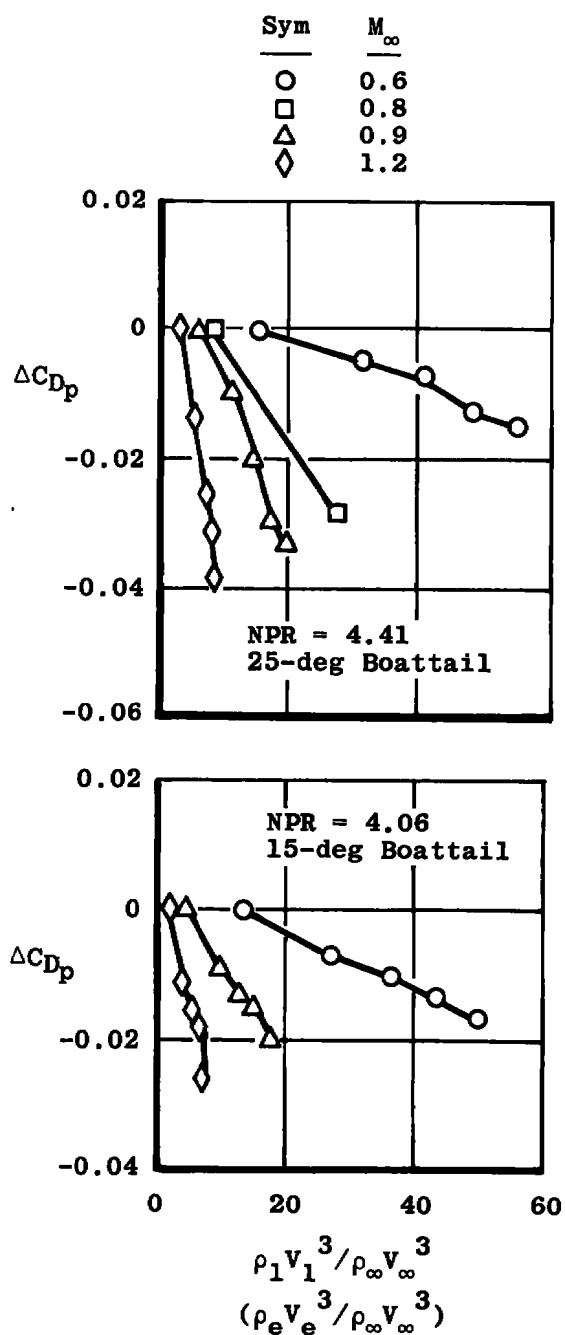
e. Difference in jet and free-stream mass fluxes
Figure 21. Continued.



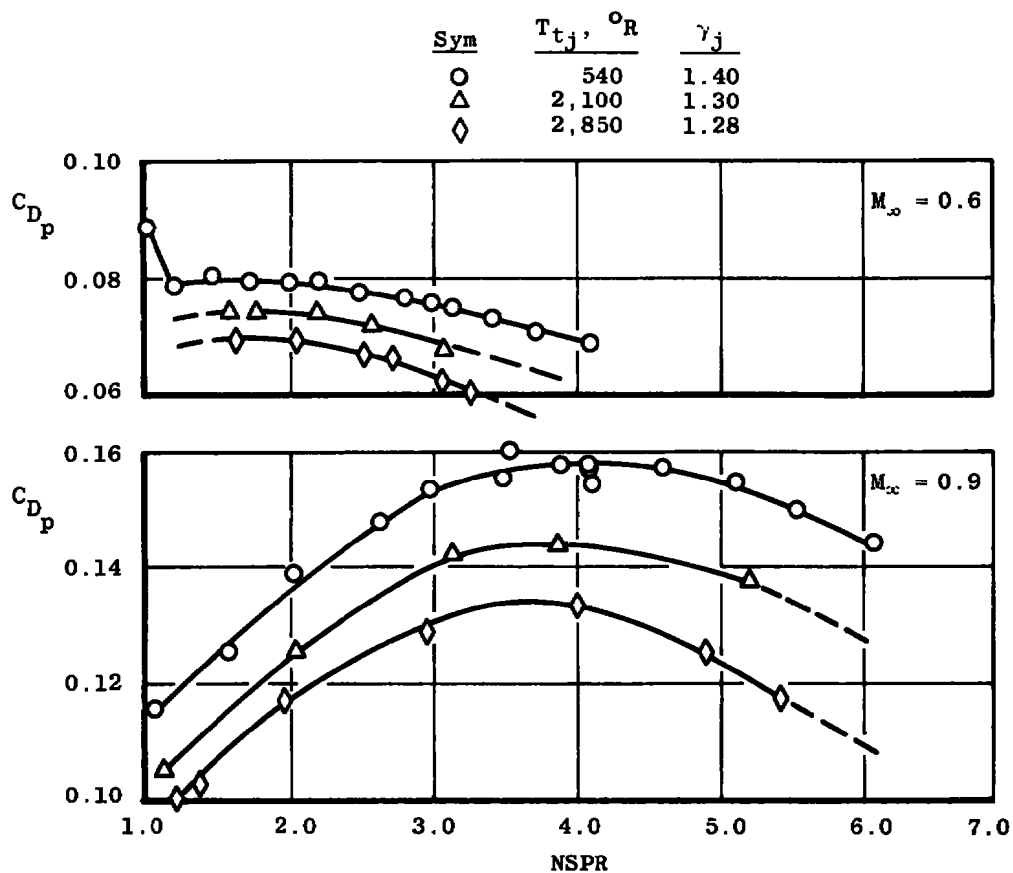
f. Ratio of jet and free-stream mass fluxes
 Figure 21. Continued.



g. Difference in jet and free-stream kinetic energy fluxes
 Figure 21. Continued.

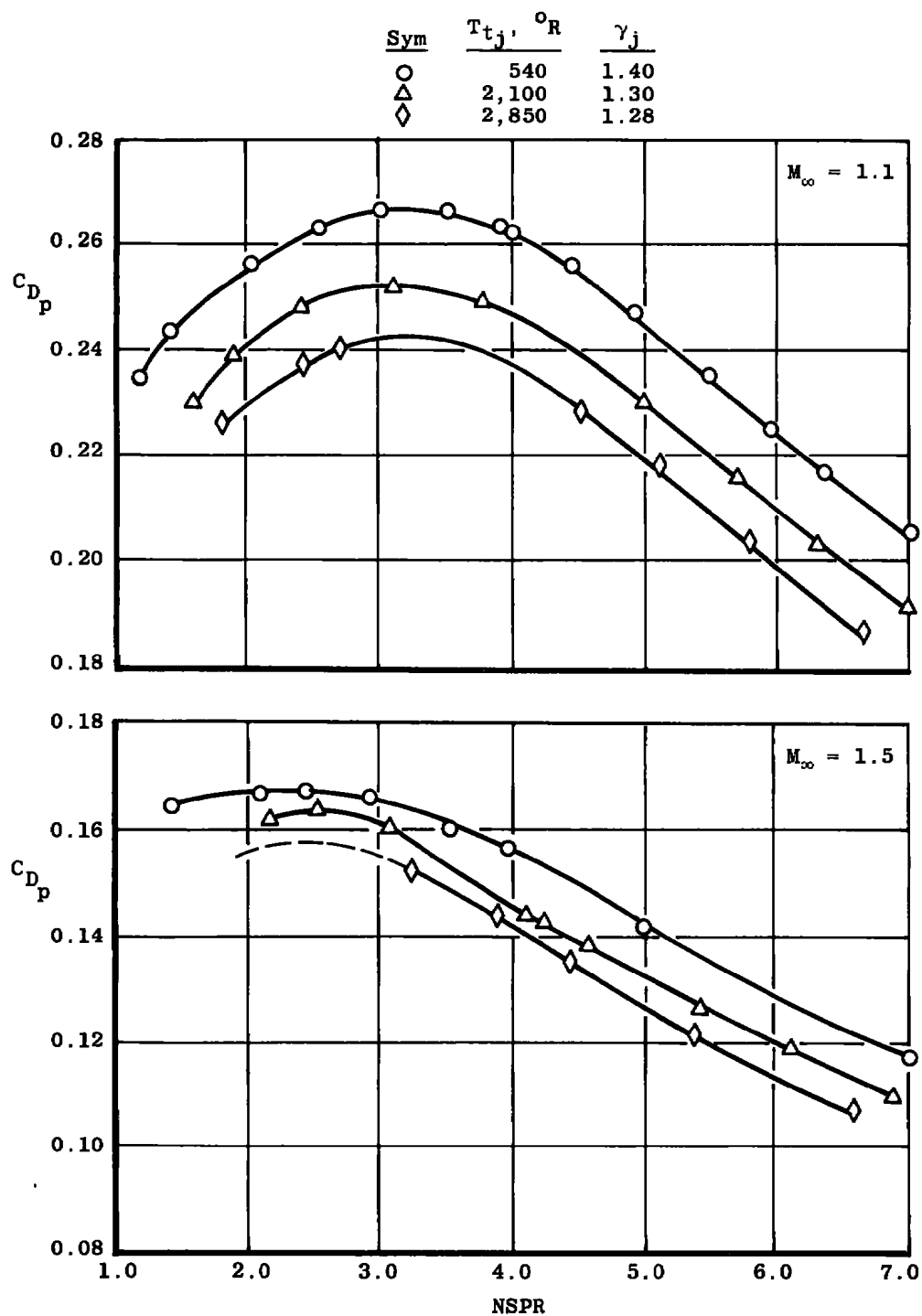


h. Ratio of jet and free-stream kinetic energy fluxes
Figure 21. Concluded.

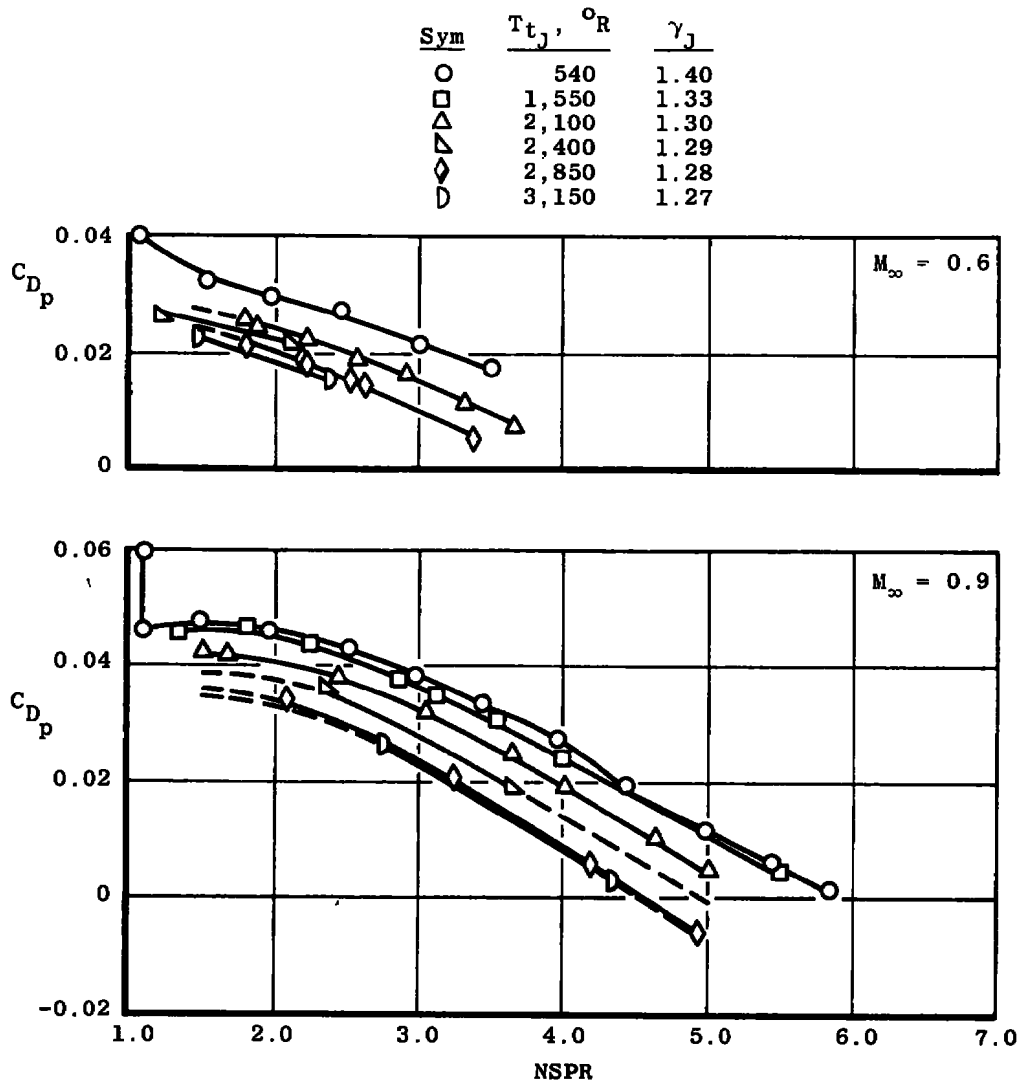


a. 25-deg boattail

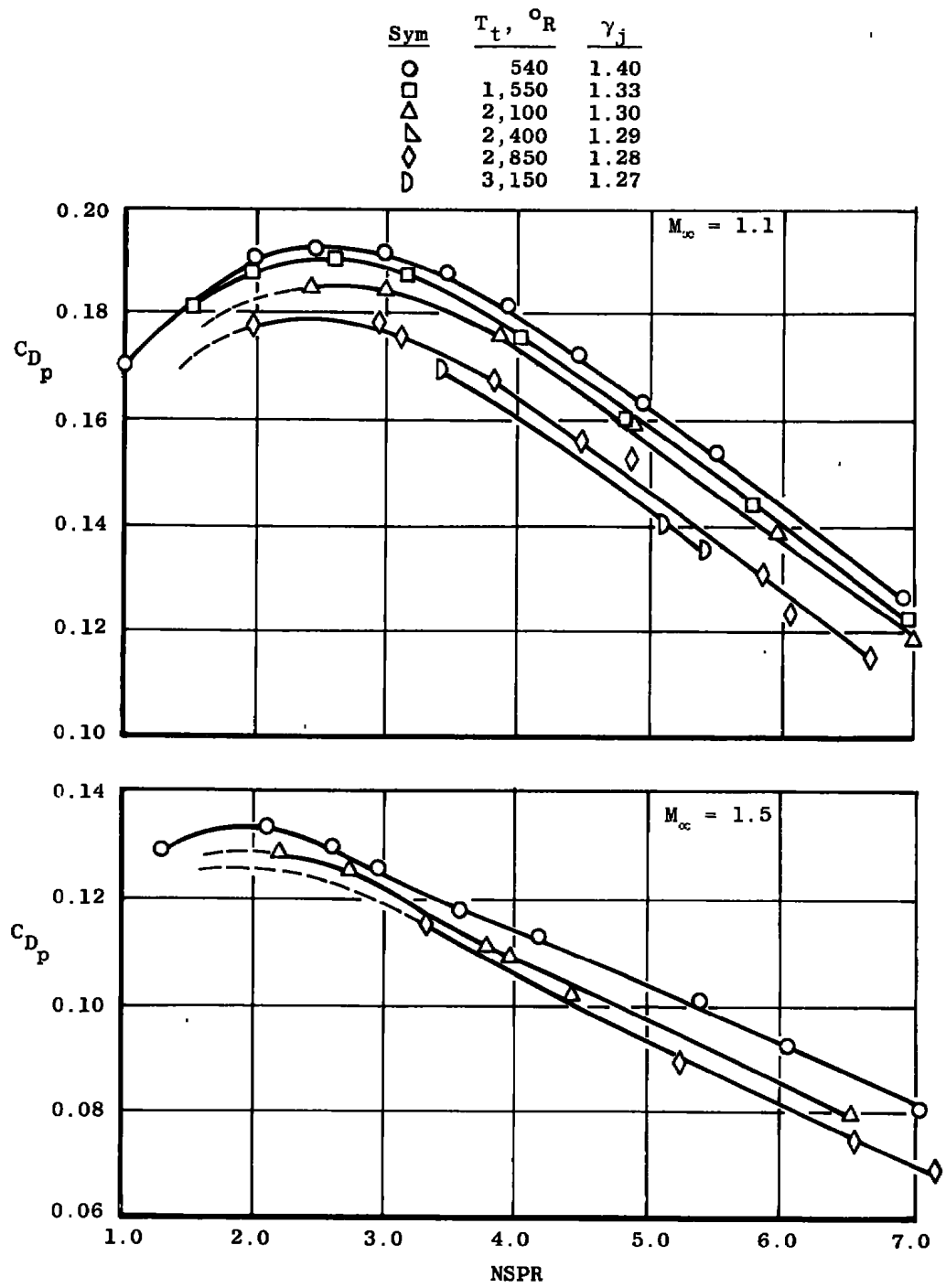
Figure 22. Jet total temperature and specific heat ratio effects on afterbody pressure drag coefficient as a function of an inviscid jet plume shape matching parameter, $A_e/A^* = 1.000$, $R_j = 53.35$ ft-lbf/lbm- $^\circ R$ (data from Refs. 1 and 3).



a. Concluded
Figure 22. Continued.

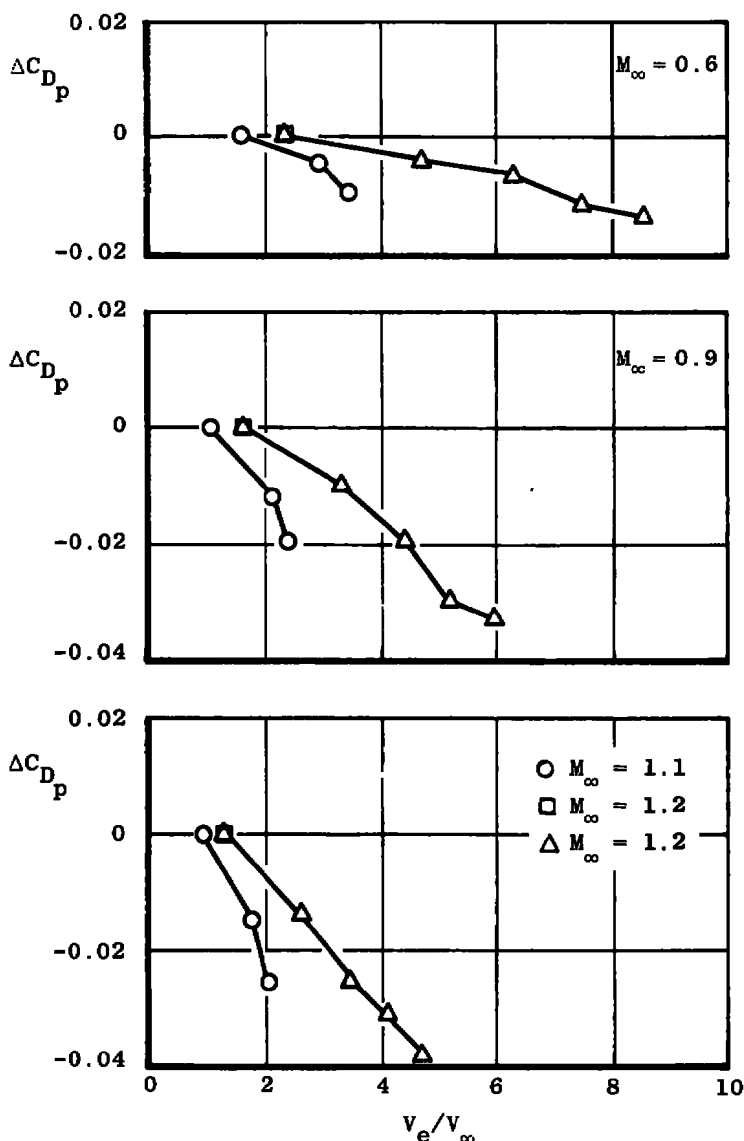


b. 15-deg boattail
Figure 22. Continued.



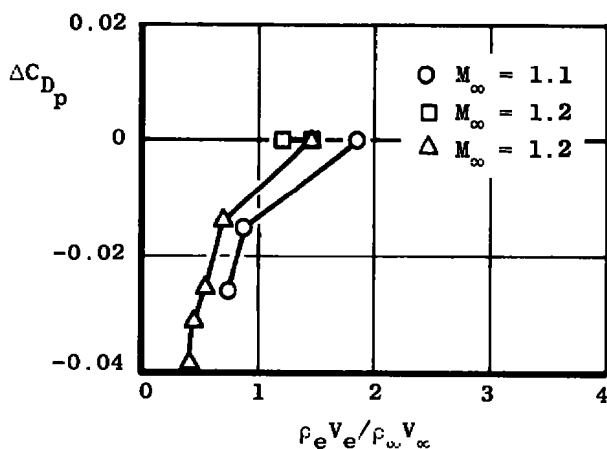
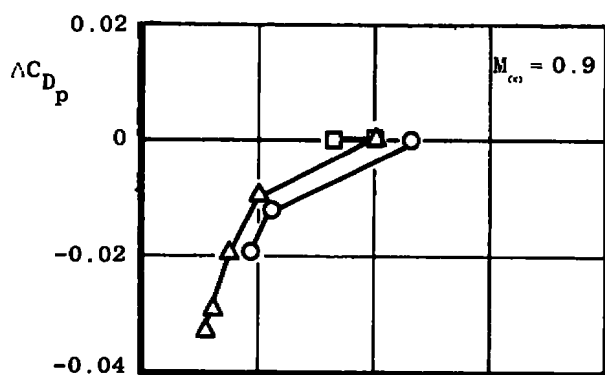
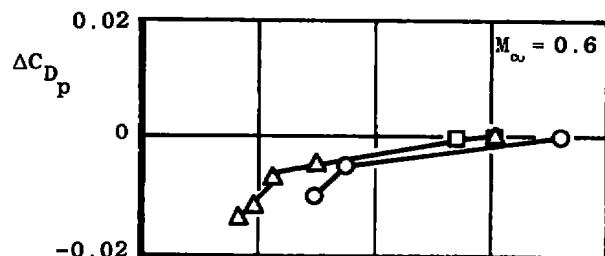
b. Concluded
Figure 22. Concluded.

Sym	Variable	γ_j	$T_{tj}, ^\circ R$	$R_j, \frac{ft-lbf}{lbm-OR}$	A_e/A^*	NSPR
○	γ_j and T_{tj}	1.40 to 1.28	540 to 2,850	53	1.000	2.0
□	γ_j	1.40 to 1.20	630	55	1.271	1.0
△	R_j	1.40	630	55 to 767	1.271	1.0



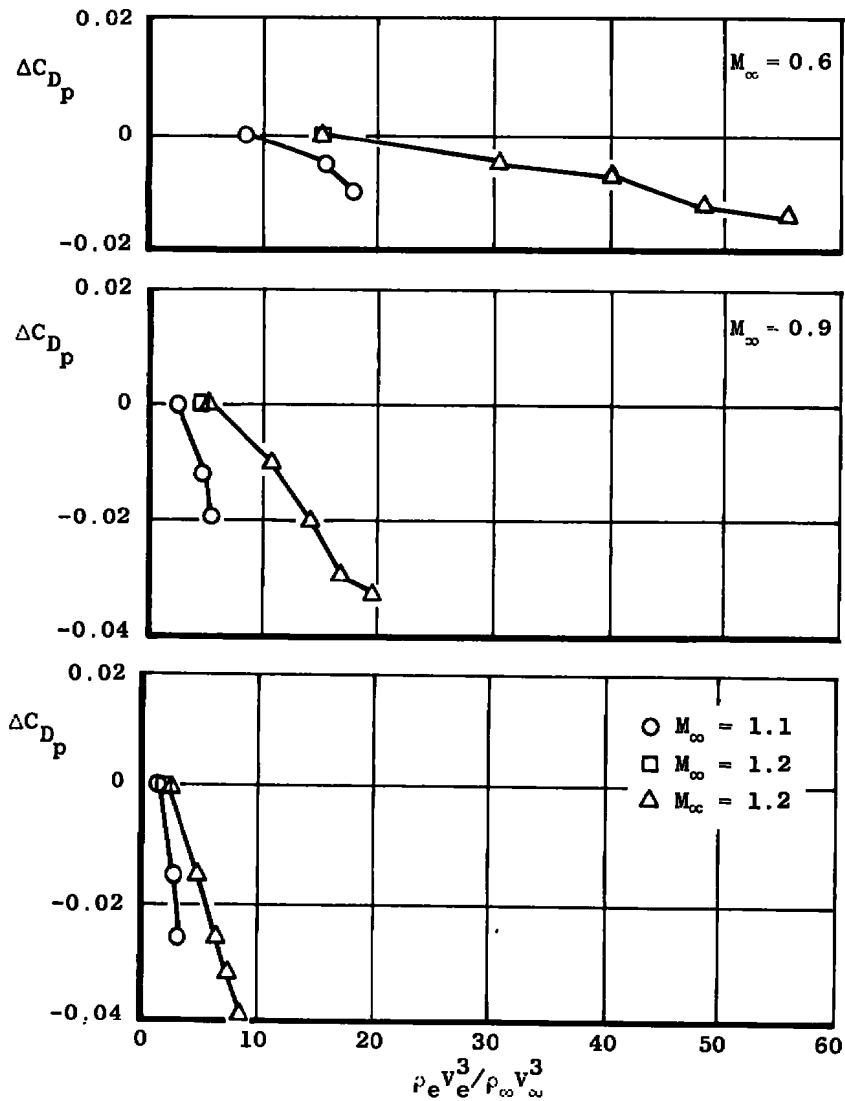
a. Ratio of jet and free-stream velocities at nozzle exit
 Figure 23. Comparison of pressure drag coefficient increments on the 25-deg boattail at fixed jet plume shape conditions for the effects of jet temperature, gas constant, and ratio of specific heats.

Sym	Variable	γ_j	$T_{tj}, ^\circ R$	$R_j, \frac{ft-lbf}{lbm-OR}$	A_e/A^*	NSPR
○	γ_j and T_{tj}	1.40 to 1.28	540 to 2,850	53	1.000	2.0
□	γ_j	1.40 to 1.20	630	55	1.271	1.0
△	R_j	1.40	630	55 to 767	1.271	1.0



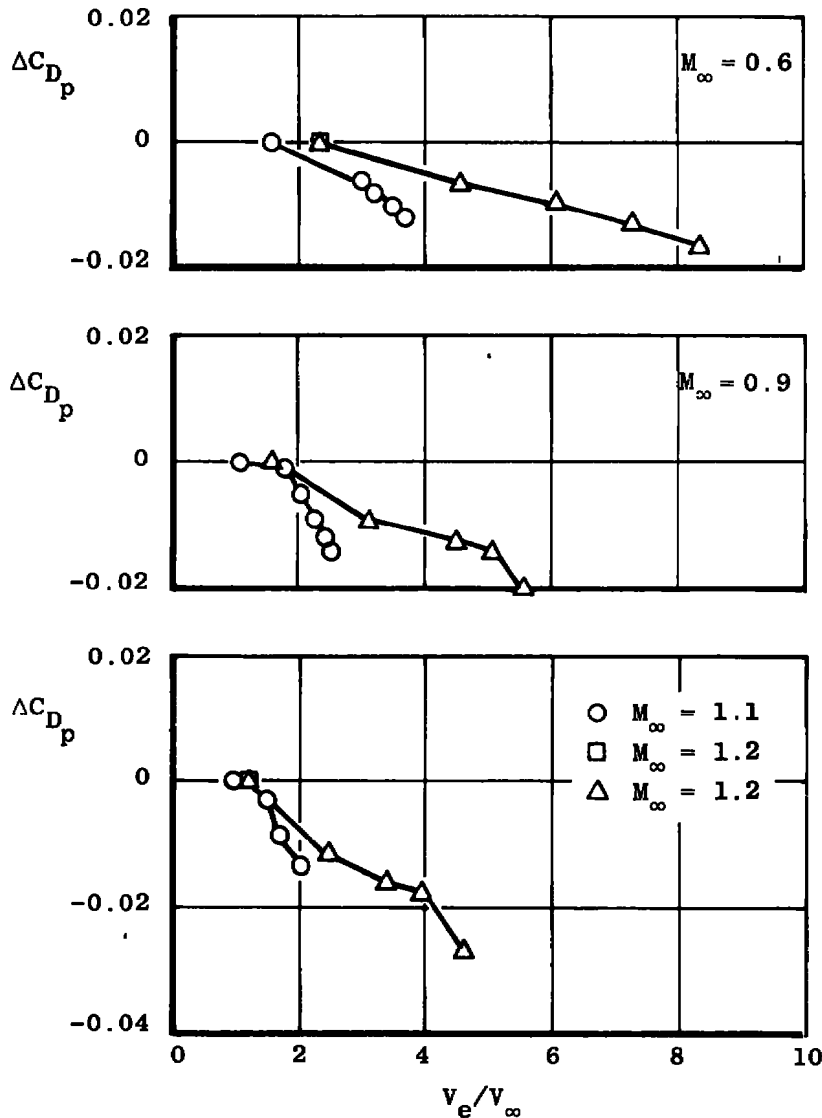
b. Ratio of jet and free-stream mass fluxes at nozzle exit
Figure 23. Continued.

Sym	Variable	γ_j	$T_{t,j}, ^\circ R$	$R_j, \frac{ft-lbf}{lbm-OR}$	A_e/A^*	NSPR
O	γ_j and $T_{t,j}$	1.40 to 1.28	540 to 2,850	53	1.000	2.0
□	γ_j	1.40 to 1.20	630	55	1.271	1.0
Δ	R_j	1.40	630	55 to 767	1.271	1.0



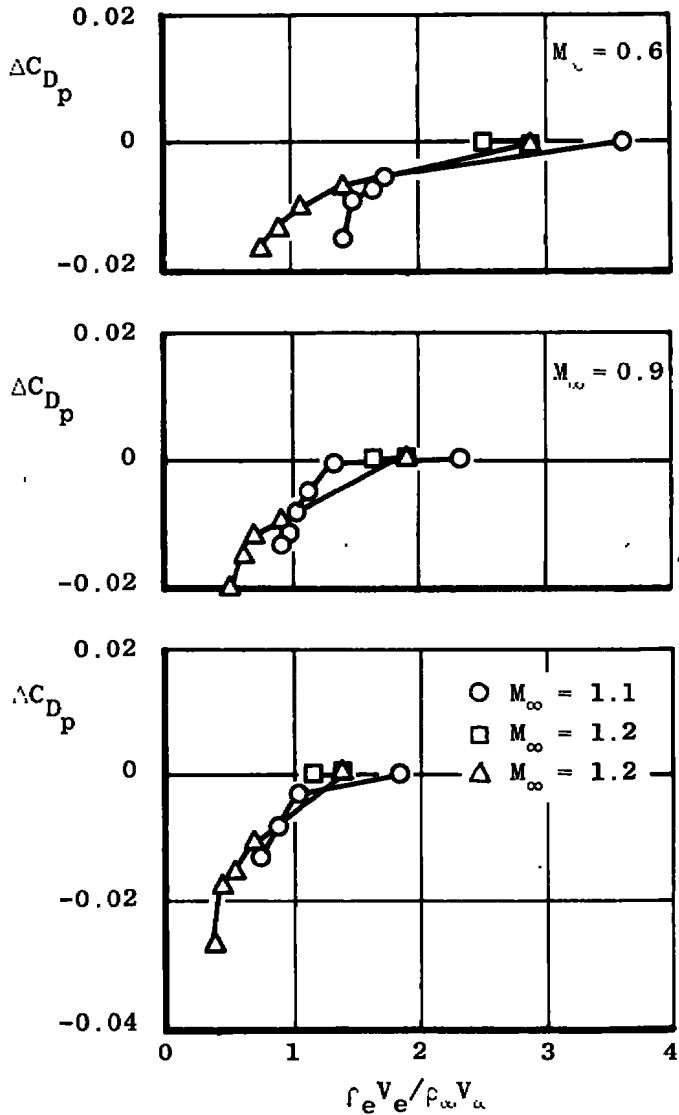
c. Ratio of jet and free-stream kinetic energy fluxes at nozzle exit
Figure 23. Concluded.

Sym	Variable	γ_j	$T_{tj}, ^\circ R$	$R_j, \frac{ft-lbf}{lbm-OR}$	A_e/A^*	NSPR
○	γ_j and T_{tj}	1.40 to 1.27	540 to 3,150	53	1.000	2.0
□	γ_j	1.40 to 1.20	630	55	1.226	1.0
△	R_j	1.40	630	55 to 767	1.226	1.0



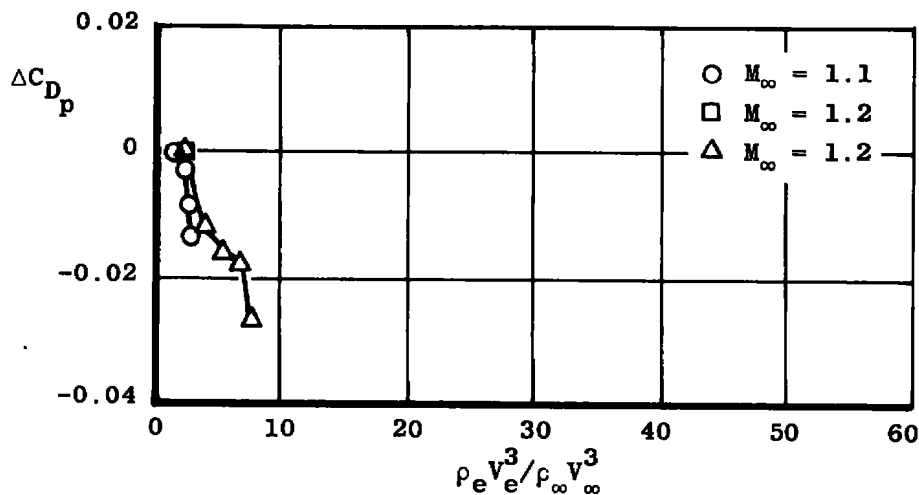
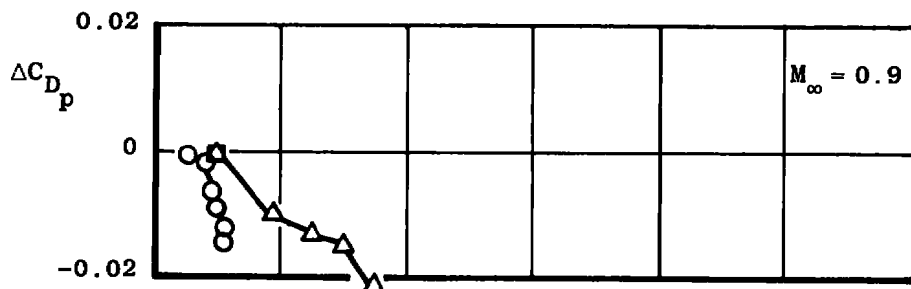
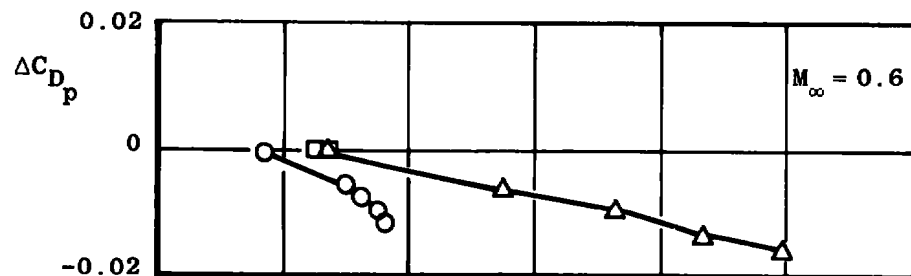
a. Ratio of jet and free-stream velocities at nozzle exit
Figure 24. Comparison of pressure drag coefficient increments on the 15-deg boattail at fixed jet plume shape conditions for the effects of jet temperature, gas constant, and ratio of specific heats.

Sym	Variable	γ_j	$T_{tj}, ^\circ R$	$R_j, \frac{ft-lbf}{lbm-OR}$	A_e/A^*	NSPR
○	γ_j and T_{tj}	1.40 to 1.27	540 to 3,150	53	1.000	2.0
□	γ_j	1.40 to 1.20	630	55	1.226	1.0
△	R_j	1.40	630	55 to 767	1.226	1.0



b. Ratio of jet and free-stream mass fluxes at nozzle exit
Figure 24. Continued.

Sym	Variable	γ_j	$T_{tj}, ^\circ R$	$R_j, \frac{ft-lbf}{lbm-OR}$	A_e/A^*	NSPR
○	γ_j and T_{tj}	1.40 to 1.27	540 to 3,150	53	1.000	2.0
□	γ_j	1.40 to 1.20	630	55	1.226	1.0
△	R_j	1.40	630	55 to 767	1.226	1.0



c. Ratio of jet and free-stream kinetic energy fluxes
at nozzle exit

Figure 24. Concluded.

Table 1. External Pressure Orifice Locations
a. Afterbody Pressures

25-deg Boattail			15-deg Boattail		
X, in.	Y, in.	ϕ , deg	X, in.	Y, in.	ϕ , deg
1.040	0.491	350	0.664	0.490	10
1.071	0.483	330	0.744	0.482	350
1.091	0.475	310	0.797	0.474	340
1.107	0.468	290	0.881	0.460	300
1.123	0.461	270	0.921	0.452	280
1.139	0.453	250	0.959	0.443	260
1.155	0.445	230	0.992	0.436	250
1.171	0.437	210	1.027	0.427	230
1.187	0.429	190	1.061	0.419	210
1.204	0.420	170	1.123	0.401	170
1.221	0.411	150	1.152	0.393	160
1.238	0.402	130	1.182	0.384	140
1.273	0.384	90	1.213	0.375	120
1.293	0.374	70	1.242	0.365	100
1.334	0.354	30	1.271	0.355	80
1.356	0.341	10	1.301	0.345	70
1.378	0.334	340	1.330	0.334	50
1.402	0.323	320	1.360	0.323	30
1.427	0.311	300	1.390	0.312	330
1.450	0.301	280	1.420	0.299	290
1.477	0.288	260	1.451	0.286	240
1.505	0.275	240	1.482	0.274	200
1.534	0.262	220	1.513	0.262	150
1.565	0.247	160	1.547	0.247	110
1.597	0.232	100	1.582	0.233	60
1.632	0.214	40	1.625	0.214	20

b. Base Pressures

25-deg Boattail		15-deg Boattail	
X, in.	ϕ , deg	X, in.	ϕ , deg
1.650	0	1.650	0
↓	120	↓	180
1.650	180	1.650	270

X = distance aft of M.S. 13.047

Y = distance from model centerline

L = afterbody length = 1.650 in.

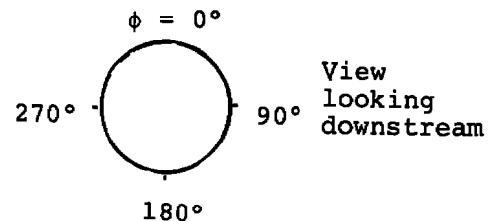


Table 2. Test Summary
a. 25-deg Boattail

Exhaust Gas	$M_\infty = 0.6$	$M_\infty = 0.8$	$M_\infty = 0.9$	$M_\infty = 1.2$
	Part No.	Part No.	Part No.	Part No.
Nitrogen (N_2) R = 55.159 $\gamma = 1.400$	17	20	24	27, 30
$N_2 + H_2$ (Mix 1) R = 231.47 $\gamma = 1.400$	71	--	67, 72	73
$N_2 + H_2$ (Mix 2) R = 408.96 $\gamma = 1.400$	86	--	87	88
$N_2 + H_2$ (Mix 3) R = 579.98 $\gamma = 1.400$	82	--	80	76
Hydrogen (H_2) R = 766.65 $\gamma = 1.400$	48, 53, 83	55, 57, 61	54, 62 81, 89	56, 77
Ethylene (C_2H_4) R = 55.084 $\gamma = 1.20-1.27$	42, 33	43	41, 34	40

b. 15-deg Boattail

Nitrogen (N_2) R = 55.159 $\gamma = 1.400$	93	--	94	95
$N_2 + H_2$ (Mix 1) R = 231.47 $\gamma = 1.400$	124*	--	125*	126*
$N_2 + H_2$ (Mix 2) R = 408.96 $\gamma = 1.400$	120*	--	119*	100
$N_2 + H_2$ (Mix 3) R = 579.98 $\gamma = 1.400$	130*	--	129*	128*
Hydrogen (H_2) R = 766.65 $\gamma = 1.400$	103	--	118*	99
Ethylene (C_2H_4) R = 55.084 $\gamma = 1.20-1.27$	107	--	111	112
Solid Cylinder Plume	133*	--	134*	135*

*Represents data with anomalies in pressure distributions.

Table 3. Free-Stream Test Conditions

M_∞	P_{t_∞} , psia	P_∞ , psia	q_∞ , psia	$Re_\infty \times 10^{-6}$, 1/ft
0.6	19.79 ↓	15.52	3.91	4.001
0.8		12.98	5.82	4.762
0.9		11.70	6.63	5.013
1.2		8.16	8.23	5.321

Table 4. Basic Properties of Jet Exhaust Gases Tested

Gas	Molecular Weight	R , $\frac{\text{ft-lbf}}{\text{lbm-OR}}$	γ at $T = 630^\circ\text{R}$ $P = 1 \text{ atm}$	Critical Temp., $^\circ\text{R}$	Critical Pressure, psia
Nitrogen (N_2)	28.016	55.159	1.40	227.1	492.4
Ethylene (C_2H_4)	28.054	55.084	1.21	509.8	742.4
Hydrogen (H_2)	2.016	766.65	1.40	60.2	188.2
$\text{N}_2\text{-H}_2$ Mixtures	6.68	231	1.40	---	---
↓	3.78	409	1.40	---	---
	2.664	580	1.40	---	---

NOMENCLATURE*

A	Nozzle area, in. ²
A_e/A^*	Nozzle exit-to-throat area ratio
C_{D_p}	Afterbody pressure drag coefficient, $D_p/q_\infty S = -\Sigma(C_{p_x})(S_{p_x})/S$
C_{p_x}	Afterbody pressure coefficient, $(P_x - P_\infty)/q_\infty$
D	Nozzle diameter, in.
D_1/D_e	Maximum inviscid jet plume boundary diameter based on isentropic flow divided by nozzle exit diameter
D_p	Integrated afterbody pressure drag, $-\Sigma(p_x - p_\infty)(S_{p_x})$, lbf
g	Gravitational constant, ft/sec ²
L	Afterbody length, 1.650 in.
M	Mach number
\dot{m}	Mass flow, lbm/sec
NPR	Nozzle total-to-free-stream static pressure ratio, P_{t_1}/P_∞
NSPR	Nozzle exit static-to-free-stream static pressure ratio, P_e/P_∞
P	Static pressure, psia
PN	Part number used to identify test runs
P_t	Total pressure, psia
q	Dynamic pressure, psi
R	Gas constant, ft-lbf/lbm-°R
$Re \times 10^{-6}$	Reynolds number per foot
S	Maximum model cross-sectional area, 0.76 in. ²

*See figure at end of Nomenclature for definition of terms.

S_{p_x}	Projected area on afterbody assigned to C_{p_x}
T	Static temperature, °R
T_t	Total temperature, °R _j
V	Velocity, ft/sec
X	Distance aft of model station 13.047, in.
X/L	Distance aft of model station 13.047 divided by afterbody length
ΔC_{D_p}	Afterbody pressure drag coefficient increment

For R_j variable, γ_j and T_{tj} fixed:

$$\Delta C_{D_p} = C_{D_p \ R_j = \text{variable}} - C_{D_p \ R_j = 55.159}$$

For γ_j and T_{tj} both variable, R_j fixed:

$$C_{D_p} = C_{D_p \ \gamma_j = \text{variable}} - C_{D_p \ \gamma_j = 1.40}$$

$$T_{tj} = \text{variable} \quad T_{tj} = 540^\circ\text{R}$$

For γ_j variable, R_j and T_{tj} fixed:

$$\Delta C_{D_p} = C_{D_p \ \gamma_j = \text{variable}} - C_{D_p \ \gamma_j = 1.40}$$

$\Delta\nu$	Incremental Prandtl-Meyer angle, $\nu_1 - \nu_e$, deg
γ	Ratio of specific heats
θ_N	Nozzle divergence half-angle, deg
ν	Prandtl-Meyer angle, deg
ρ	Mass density, lbm/ft ³
ρV	Mass flux, lbm/ft ² -sec
ρV^2	Momentum flux, lbm/ft-sec ²
ρV^3	Kinetic energy flux, lbm/sec ³

SUBSCRIPTS

l	Jet conditions at inviscid jet plume boundary
c	Jet conditions in nozzle plenum chamber
e	Jet conditions at nozzle exit plane
H ₂	Hydrogen
j	Jet conditions at any given axial station
N ₂	Nitrogen
v	Venturi conditions
x	Afterbody pressure tap axial location
∞	Tunnel free-stream conditions

SUPERSCRIPT

*	Jet conditions at nozzle throat
---	---------------------------------

